UNIVERSITY OF COPENHAGEN
FACULTY OF SCIENCE

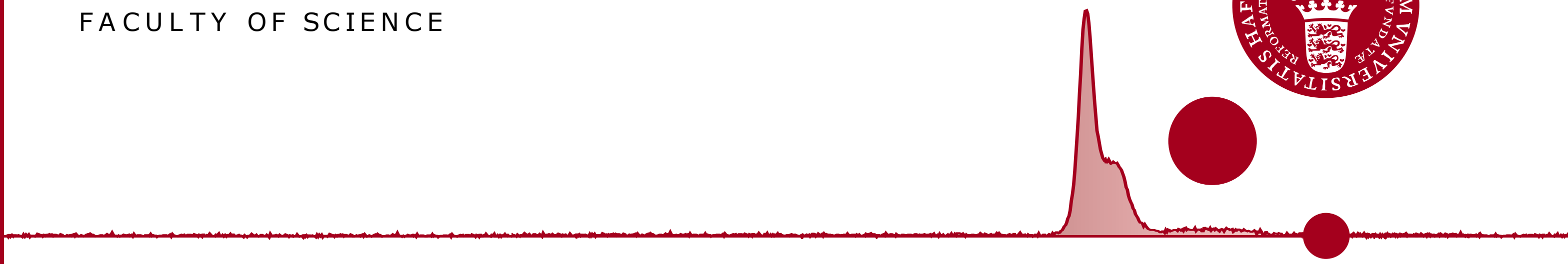

Narrow linewidth superradiant lasing with cold ^{88}Sr

PhD thesis

Sofus Laguna Kristensen

Niels Bohr Institute, August 2023

This thesis has been submitted to the PhD School of
The Faculty of Science, University of Copenhagen

Supervised by Jörg Helge Müller

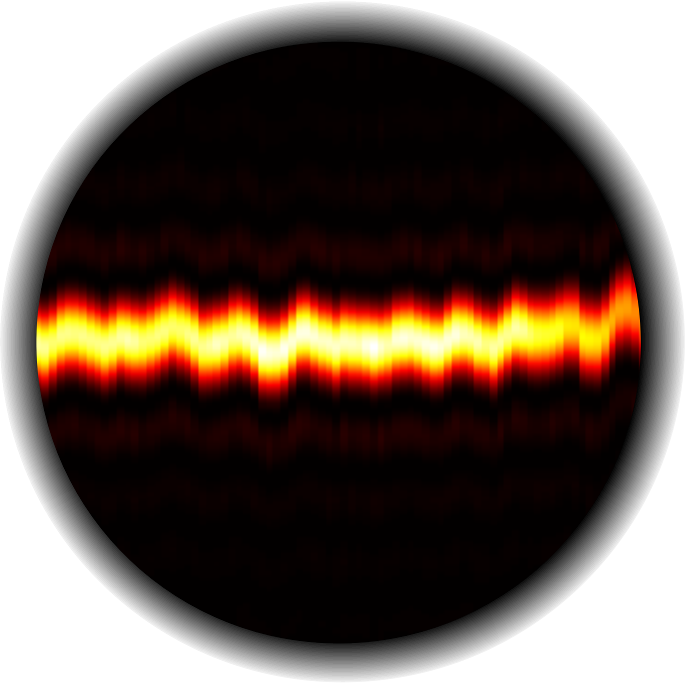

To my parents, Casper and Mette.

Abstract

Superradiant lasers operate in the bad cavity regime, where the lasing phase is stored in the spin state of an atomic medium rather than in the intra cavity electric field. Such a laser exhibits decreased sensitivity to cavity mirror vibrations and eliminates the need for separate reference cavity, overcoming limitations of modern atomic clocks. No fully continuous superradiant laser has been reported yet, and most studies describing the behavior of superradiant light investigates pulses shorter than the natural lifetime of the lasing transition.

This thesis details the development and the results of a system designed to produce extended narrow linewidth superradiant pulses for a proof of concept measurement. We use the 7.48 kHz wide $^1S_0 \rightarrow {}^3P_1$ intercombination line in ^{88}Sr to produce intense superradiant pulses. Inherently, the collectively enhanced decay of a superradiant pulse produced by a single population inversion will result in a Fourier limited lasing linewidth larger than the natural linewidth of the transition. However, the linewidth of the lasing can be significantly decreased if the lasing phase is carried over through continuous synchronisation of atomic phases. By extending the lasing from just a few µs to several ms using repumping, we observe a lasing linewidth $\Delta\nu_l/2\pi = 820$ Hz, almost an order of magnitude below the natural linewidth of the lasing transition. We regulate the gain of lasing by tuning the repumping frequencies, transforming the effective 3-level laser system into a 4-level laser. This allows us to sustain several ms of steady state lasing and emulate the behavior of a truly continuous superradiant laser. Furthermore, we study the time-dependent cavity pulling and verify that the system operates in the bad cavity regime where it is insensitive to cavity mirror vibrations.

We have implemented a 689 nm narrow linewidth MOT to bring the system into the bad cavity regime, and have managed to trap upwards of 120 million atoms at 2 µK in the single frequency red MOT, which allows for very strong atom-cavity interactions. This experimental setup was also used to realize a superradiance enhanced readout scheme for a Ramsey interferometer sequence. This scheme is fast and much less destructive to the atomic sample than traditional fluorescence readout techniques, and has promising applications for enhancing future quantum sensors.

Resumé

Superradiante laser opererer i ”dårlig resonator” regimet, hvor laser fasen opbevares i det atomare medium i stedet for det elektriske felt i en optisk resonator. En sådan laser har nedsat følsomhed over for vibrationer i resonatorspejlene, og eliminerer behovet for et separat reference resonator, hvilket for nuværende er en begrænsning i moderne atomure. Ingen har endnu formået at realisere en fuldt ud kontinuert superradiant laser, og de fleste studier der beskriver opførslen af superradiant lys undersøger pulser der er kortere end den naturlige levetid for laserovergangen.

Denne afhandling beskriver udviklingen og resultaterne af et system designet til at producere lange superradiante pulser med en smal linjebredde. Vi bruger den 7.48 kHz brede ${}^1S_0 \rightarrow {}^3P_1$ interkombinationslinje i ^{88}Sr til at producere intense superradiante pulser. Det kollektivt forstærkede henfald af en superradiant puls produceret af en enkelt populationsinversion resulterer i en Fourier-begrænset laserlinjebredde, der er større end den naturlige linjebredde for overgangen. Dog kan linjebredden for lasingen betydeligt reduceres hvis laserfasen overføres gennem kontinuerlig synkronisering af atomfaserne. Ved at forlænge lasingen fra kun få µs til flere ms ved hjælp af repumping observerer vi en laserlinjebredde $\Delta\nu_l/2\pi = 820$ Hz, næsten en størrelsesorden under den naturlige linjebredde for laserovergangen. Vi regulerer lasens forstærkning ved at justere repumping frekvenserne, hvilket transformerer det effektive 3-niveau laser system til en 4 niveau laser. Dette tillader os at opretholde stabile laser intensiteter for at emulere opførslen af en reel kontinuert superradiant laser. Desuden studerer vi den tidsafhængige resonator træk-koefficient og verificerer at systemet opererer i ”dårlig resonator” regimet hvor det er ufølsomt over for resonator fluktuationer. Vi har implementeret en MOT på den smalle 689 nm overgang for at bringe systemet ind i ”dårlig resonator” regimet, og vi har formået at fange og køle over 120 millioner atomer til 2 µK i den enkeltfrekvens-røde MOT, hvilket tillader meget stærke atom-resonator interaktioner. Eksperimentet blev ydermere brugt til at realisere en superradiens-forstærket aflæsningsmetode for en Ramsey interferometer sekvens. Denne metode er hurtig og meget mindre destruktiv for atom-ensemblet end traditionelle fluorescensaflæsningsteknikker, og den har lovende anvendelser til at forbedre fremtidige kvantesensorer.

Preface and acknowledgements

This thesis outlines my experimental work since I joined the group as a research assistant in the spring of 2019, and later as a PhD student from the beginning of 2020. I already had the pleasure of joining Jan's group as a bachelor student in 2016, working on cavity enhanced saturated absorption spectroscopy of molecular iodine - a project that served as my introduction to the wonders of experimental AMO physics. Jan ushered me forth and made arrangements for me to write my Master's thesis in Holger Müller's group at UC Berkeley. Here, I got the chance to partake in some simply mind-blowing research of intracavity atom interferometry. A spatial superposition cesium atoms with 20 s coherence times? Sure, why not. Upon my return to Copenhagen, Jan hired me as a research assistant. Having worked with infrared transitions at UC Berkeley, I immediately fell in love with the beautiful (and visible..) colors used in our strontium experiments. Lucky for me, Jan offered me to join the group as a PhD starting in the winter of 2020.

I wanna thank **Jan W. Thomsen** for bringing me into the world of AMO physics. Jan's passion for experimental physics and his endless enthusiasm are just some of the admirable qualities that makes him a great supervisor. Just before I started my PhD, Jan had to take up the reigns as head of institute, and in his stead he appointed **Jörg Helge Müller** to supervise the lab. I am extremely grateful to Jörg for taking charge of our education, even though he definitely had enough on his plate already. Jörg is an actual oracle when it comes to experimental and AMO physics and he will happily answer any questions you have, day or night. I like Jörg's pleasant way of engaging with his students, and it is not uncommon for an innocent coffee break to turn into a 4 hour long physics discussion. I am looking forward to many more of those in the future!

I want to give a huge shout out to my close colleague **Eliot Bohr**, with whom I have worked closely over the past few years. It has been a joy and a pleasure to share countless hours working in the lab. By now, we have also travelled the world together on various conferences, and together we have experienced what it is like to be a part of the grown up research community. We have made it an important tradition to remember to celebrate our accomplishments, and I am very much looking forward to grabbing a beer with you once both of us have handed in our theses. Cheers mate.

Thanks to **Julian Robinson-Tait**, without whom I would not have survived the dark winter in the lab during the height of the COVID-19 pandemic. In just a few months, we managed to develop an alternative way to communicate on a higher level (we might just have been screaming). Julian has worked extremely hard on a tricky experiment since the start of his PhD and has gained a lot of experience in leading projects as a result - I am excited to see what he will do after his PhD.

I wanna extend my thanks to past and present members of the group. **Stefan Alaric Schäffer** has taught me a great deal about basically every discipline within experimental AMO physics. We are thankful that we have gotten him back from his brief layover in Amsterdam. **Mikkel Tang** worked alongside me on the experiment when i first started my PhD, and he was in the trenches with us when we fought a losing battle against an unruly experiment. His experimental model produced some invaluable results that kept the group afloat in a time where the experiments did not produce many results. I have shared many great experiences with **Asbjørn Arvad Jørgensen** during our time at NBI. Among them are tutoring new students and participating in FysikRevyen™. Arvad's presence in the lab was always positively felt through an abundance of puns and discussions about the real origin of the linewidth. He has also made significant contributions to the lab infrastructure with his development of the QWeather system. **Martin Romme Henriksen** is highly skilled experimental physicist with extensive knowledge of RF electronics, and his anecdotes about life on the country side has kept the group entertained through many coffee breaks. **Valentin Cambier** joined us for a postdoc where he fought alongside Julian to try and get Sr2 to behave. His friendly personality was a pleasant presence in the lab.

I have also had the chance to supervise some brilliant students. **Maria Skak Vestergaard Larsen** worked on the red MOT setup as well as the initial normal mode splitting measurements of the blue MOT. **Mantas Ambroza** worked on the frequency stabilization of our repumper systems. **Andrea Sommer Eriksen** has chosen to rejoin us for her Master's thesis after she wrote her bachelor on the red MOT and imaging systems in our group. Furthermore, **Maddalena Genzini**, **Caroline Munck Nielsen**, and **Jonathan Elsborg** joined us for their masters working on the frequency combs and Sr2, respectively. Greater company in the lab is hard to come by.

I would like to acknowledge the help we have received from the mechanical workshop, more specifically **Dennis Westphal Wistisen** and **Michael Heide Bernt**. Dennis is always extremely engaging and helpful and will go to great lengths to make sure that you get exactly what you came for. Michael used his insane technical ability to manufacture a million miniature oven components. I have no idea how we would have progressed experimentally without the help of the workshop.

I, and the group as a whole, is extremely grateful that **Tanya Zelevinsky** chose to work in our lab for half a year in the start of 2022. It was like getting an additional supervisor for free. Her inputs proved invaluable in the path towards generating narrow linewidth superradiance, and we hope to get the chance to work with her in Copenhagen again.

Through various conferences and consortium meetings, I have had the pleasure of being introduced to the PhD students working under the MoSaiQC umbrella. It has been a fantastic experience getting to know so many early stage researchers at similar points in their career.

Finally, I would like to thank Mikkel, Julian and Stefan for providing very useful feedback on a few chapters in this thesis.

Papers

The work conducted before and during my PhD has led to the following publications;

- *Subnatural Linewidth Superradiant Lasing with Cold* ^{88}*Sr Atoms*
  S.L. Kristensen, E. Bohr, J. Robinson-Tait, T. Zelevinsky, J.W. Thomsen, Jorg Helge Muller, Phys. Rev. Lett. 130, 223402 (2023).

  > [1] This is the central paper detailing my PhD work. Through meticulous control of repumping rates, we were able to produce superradiant lasing pulses with a linewidth substantially below the natural linewidth of the lasing transition. This thesis describes all the experimental progress that was necessary to achieve this feat.

- *Collectively enhanced Ramsey readout by cavity sub- to superradiant transition*
  E. Bohr, **S. L. Kristensen** et. al, arXiv:2306.12544

[2] In this paper we experimentally verify the proposal in [3] and use superradiant pulses as a state readout in a Ramsey interferometer. We show that the superradiant laser pulses can be used as a fast and non-destructive readout of the atomic state, which can ultimately be used to stabilize the frequency of the interrogation laser. It is currently under review at Nature Communications.

- *Raman transitions driven by phase-modulated light in a cavity atom interferometer*
  S. L. Kristensen, M. Jaffe, V. Xu, C.D. Panda, H. Müller, Physical Review A 103 (2), 023715

  [4] This paper is an investigation of data taken during my 1 year stay at UC Berkeley when doing my master's thesis. It outlines the theory for driving intracavity Raman transitions using phase modulated light in a cavity atom interferometer, and confronts the theory to experiments. I use parts of this theory to discuss the effect of driving atoms with an inhomogenous beam profile, which also applies to our experiment.

- *Interferometri med ultrakolde atomer*
  S.L. Kristensen, Kvant 1, 16-19

  [5] This paper describes the applications of cold atoms and matter waves for precision measurements. It was published in the Danish popular science journal, Kvant, in 2020.

- *Probing gravity by holding atoms for 20 seconds*
  V. Xu, M. Jaffe, C.D. Panda, **S. L. Kristensen**, L.W. Clark, H. Müller, Science 366 (6466), 745-749

  [6] This paper describes the creation and results of a lattice atom interferometer. The lattice is formed inside an optical cavity, which allows for extreme coherence times in the spatially separated wavefuntion. This work was performed and published before my PhD and will not be discussed in this thesis.

Contents

List of Figures

Chapter 1

Introduction

The development of techniques to catch and coherently control ensembles of atoms, ions, and molecules at low temperatures has opened a diverse field of research using quantum systems for sensing and metrology applications. A cloud of cold atoms inside a vacuum chamber constitutes a localized and coherent quantum system that is an ideal test bed for investigating or exploiting the quantum nature of atoms. Such systems benefit from low collision rates, low velocities, extended interaction time, and the ability to store a large number of atoms at a high density, increasing the obtainable signal amplitude [7–10]. The relativity recent addition of techniques utilizing the quantum nature of cold atoms, ions and molecules has resulted in a new generation of tabletop experiments to probe and push the frontier of established physics - a field that was previously driven by more comprehensive and expensive experiments performed in high energy physics [11].

The potential applications of such systems includes measuring the fine structure [12] and gravitational constant [13, 14], probing electron dipole moment [15], tests of general relativity [16], searches for dark matter and energy [17, 18], performing quantum simulation [19], and quantum computing [20]. These advances were also made possible due to significant advancements of building and controlling coherent light sources; lasers stabilized to high finesse cavities allows for coherent manipulation of atoms using very narrow linewidth transitions, which enables cooling atoms to low temperatures and to probe long lived states where the laser must retain its coherence throughout the interrogation [21].

In quantum metrology, the information of the measured quantity imprinted on a quantum system is often extracted by reading out the final state of the system. In an atom interferometer, the phase shift of the atomic wavepacket can be read out as a shift of population usually between two metastable states, for example the two ground states in cesium ($F = 3$ and $F = 4$). The interference fringe is a result of a beating between the phase of a laser and the phase of atoms when applying a recombination laser pulse. Relying on a steady laser phase, the atomic phase shift can then be extracted and interpreted. In an atomic clock, the opposite is true. Here, the scheme relies on a well-defined atomic phase to determine the frequency of the laser.

1.1 Atomic clocks

Atomic clocks consist of two primary components: an oscillator and a reference. The role of the oscillator can be explained using an old-fashioned pendulum clock analogy. Each period completed by a swinging pendulum can constitute a unit of time, and for a pendulum with a 1 meter long swing arm, this period will be close to a second. The total number of oscillations completed by the pendulum clock provides a measure of the elapsed time since counting started. However, the frequency of the oscillation is be affected by external factors such as air resistance and friction, which causes the clock to become less accurate over time. This is where the reference is important - to keep track of the oscillations and to lock the oscillation period at exactly one second. In an atomic clock, the ”pendulum” is a coherent electromagnetic field - often the beam of a stable laser. The oscillation of the electric field is extremely fast compared to mechanical clocks, which makes it possible to quantize time with a much higher resolution. The laser, like the pendulum clock, is subject to drifts caused by vibrations and/or temperature changes. To stabilize the laser frequency, the laser is tuned to resonance with an atomic transition. Atomic energy levels are quantized, and electrons need a specific amount of energy to jump between the different states, $E = \hbar\omega$ (where $\hbar$ is the reduced Planck constant and ω is the angular transition frequency that the laser must match).

The spectral width of an atomic transition is referred to as the natural linewidth γ, and it is inversely proportional to the lifetime τ of the excited state,

$$\gamma = \frac{1}{2\pi\tau}, \tag{1.1.1}$$

which is a manifestation of Heisenbergs uncertainty relation in energy and time [22]. For longer lived states the spectrum becomes more narrow, enabling precise determination of the laser frequency using either Ramsey [23] or Rabi [24] type interrogation schemes.

Atomic clocks benefit from the universality of atoms; lasers referenced to atoms experiencing the same external conditions will always operate at the same frequency, be it on Earth or in outer space. The best performing atomic clocks are the optical lattice clocks, where a sample of atoms is cooled to a very low temperature and caught in an optical lattice. By meticulously controlling and quantizing the external factors influencing the resonance frequency of the atoms, such clocks can achieve fractional instabilities below 10^{-18} [25–28], which translates to the clock losing just one second in 30 billion years, twice the age of universe. Precise timekeeping have practical applications for satellite positioning (e.g. GPS), tracking of financial exchanges, internet and geological surveys. In fundamental science, atomic clocks can be used for probing the potential drift of fundamental constants, testing of general relativity, measuring gravitational waves, or searching for dark matter. Furthermore, atomic clocks are responsible for global timekeeping. In the 1967 the second was redefined as 9.192.631.770 oscillations of the radiation emitted from the transition between the two ground states of ^{133}Cs, and the definition remains this day. A weighted average of more than 300 atomic clocks forms the Intentional Atomic Time (TAI), and the contributions from different clock laboratories can be looked up at BIPM's website[1].

Significant advances have led to modern atomic clocks surpassing the performance of traditional cesium clocks by orders of magnitude [29, 30]. However, such clocks suffer from a few limitations. The relatively long sample preparation times results in a low duty cycle on the feedback to the laser frequency. This gap in interrogation is usually bridged by locking the clock laser to a high-finesse optical cavity, which is stable on the time scales needed to prepare and probe another sample of cold atoms - but such cavities are limited by vibrations and thermal noise on the mirrors [31]. This can be remedied with a cryogenically cooled crystalline cavity [32] and meticulous vibration isolation, which significantly adds to the experimental complexity.

---

[1] https://www.bipm.org/en/time-ftp/circular-t

The continuous improvement of the already impressive performance of optical atomic clocks is an increasingly difficult challenge, as external perturbations to the atomic reference plays at big role at sub 10^{-18} fractional stability levels. The best performing optical clocks are usually bulky and requires a many people to build and maintain them. This makes them unfit for deployment in the field and for satellite integration, which excludes a few of the aforementioned practical implementations. The sheer complexity, cost, and physical volume of such setups has motivated the development of alternative frequency stabilization schemes. These include using multiple atomic ensembles to bridge the aforementioned interrogation time gap [33–36], non-destructive measurements of the atomic ensemble [37, 38], or continuous loading and interrogation of atoms with a conveyor-belt scheme [39]. Previous work performed in our group aimed to use the coupling between a cavity and a cold atom sample to conduct passive cavity-assisted nonlinear spectroscopy [40–42] for laser stabilization, but such a scheme requires precise tuning of the feedback bandwidth and management of technical noise.

These schemes are all examples of passive atomic interrogation. The atoms are used as a passive reference to correct the frequency of a laser that is ultimately used as a clock. An exciting prospect is the realization of an active frequency reference using cold atoms in an optical cavity. In such a system the atoms are "active" in the sense that they generate the lasing themselves using collective effects. If the lasing transition is narrower than the cavity linewidth, the lasing can directly inherit the stability of the atomic transition. The working principle of an active optical clock is similar to a hydrogen maser [43], but it operates using an optical transition with a much higher frequency.

1.2 Superradiance and active-lasing schemes

When an atom is in an excited state, it will eventually emit a photon with a random phase through a process known as spontaneous emission, transitioning to a lower energy state. The lifetime τ of an excited state is defined as the time when the probability of finding the atom in the excited state has dropped to $P_e = 1/e$. However, this rate of emission can be modified by bringing multiple atoms close together. If the wavelength of the emitted light is much greater than the separation of the atoms, the atoms will constructively couple to the same free space mode which can greatly enhance the emission rate of the ensemble by several orders of magnitude (Fig. 1.1). This is what we refer to as a superradiant burst, and it was originally predicted by Robert Dicke in 1954 [44]. In the quantum mechanical picture,

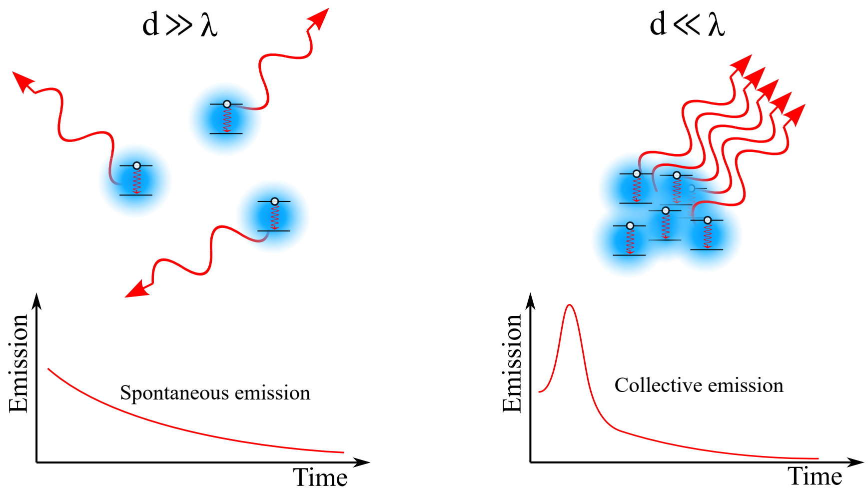

Figure 1.1: Emission of separated and closely spaced two-level emitters. If the emitters are separated, they will decay individually with the natural decay rate of γ. However, with closely spaced the emission rate is enhanced through a collective emission process.

superradiance is the result of the formation of so-called "Dicke states" [3], an entangled state where the atoms act as a single entity with effective dipole moment that is bigger than that of the individual atoms.

The spacing requirement of the emitters is easily satisfied for microwave transitions, where the wavelength of the emission is on the scale of cm. However, to observe superradiance for optical transitions, where the wavelength is on the hundreds of nm scale, it is convenient to use an optical cavity. The cavity creates a preferred emission mode to enable long range interactions between separate emitters that would not interact strongly in free space. Such atom-cavity systems has been shown to produce strong superradiant bursts on optical transitions [45–48], which has fueled the scientific interest in producing a steady-state continuous superradiant laser for frequency metrology applications.

1.2.1 Continuous superradiance

Conventional lasers work by using an optical cavity and a gain medium. The gain medium can usually amplify light over a broad range of frequencies by stimulated emission, and the cavity provides a preferred mode for emission. The intracavity field has well defined frequency and phase, and the leak through one of the cavity mirror forms the emitted laser beam. The cavity works as a frequency discriminator to carve out a much narrower

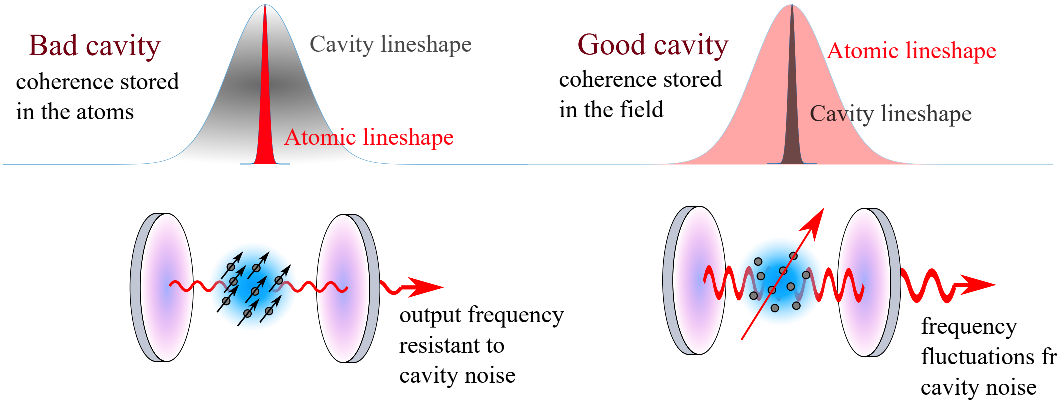

Figure 1.2: Bad cavity regime and good cavity regime. In the bad cavity regime, the frequency is dictated by the atoms. The phase of the lasing is upheld through continuous synchronisation in the atomic phases. In the good cavity regime, the frequency is dictated by the cavity, as the phase information is stored in the intracavity field.

frequency spectrum than the linewidth of the gain medium. This is what we refer to as the ”good cavity” regime (Figure 1.2). In this regime, photons circulating within the cavity will be stored longer than the time atoms take to emit into the cavity mode. Crucially, the coherence of the laser is stored in the intracavity field, which means that the frequency and phase of the laser is susceptible to vibrations in the cavity mirrors.

If the gain medium is much narrower than the cavity in frequency space, the frequency is dictated by the gain medium. This is the ”bad cavity” regime, where the cavity field decays quicker than the atoms emits photons into the cavity mode. This means that the coherence is primarily maintained in the phase of the atoms, and the lasing frequency is less sensitive to vibrations in the cavity mirrors. This sensitivity is characterized by the so-called cavity pulling coefficient, c_p. For $c_p = 1$, the emission frequency of the laser follows the cavity resonance. For $c_p < 0.5$, the frequency is mostly dictated by the atomic resonance frequency. If a narrow gain medium is used, such as cold atoms continuously repumped to a long lived excited state, the bad-cavity regime is accessible.

This lasing scheme eliminates the need for a separate stable reference cavity for laser stabilization, as the collectively enhanced emission of the intra-cavity atoms constitute the frequency reference. In combination with the suppressed environmental sensitivity of the bad-cavity regime, the realization of such a laser would constitute an entirely new generation of ultra stable lasers with broad applications within quantum metrology and sensing. Particularly, the simplified scheme for generating a stable frequency reference has intriguing applications in the realms of portable and space-borne quantum sensors.

In a steady state superradiant laser, the atomic phases continuously synchronize through the cavity field, which virtually increases the lifetime of the excited lasing state - thus allowing for much narrower linewidths than the atomic linewidth from the Heisenberg uncertainty relation. The fundamental limit of such a laser for optimal pumping parameters is theorized to be determined only by the single atom decay rate γ and the cavity cooperativity, C (which we shall discuss more in depth in the next chapter), through the Purcell limit [49],

$$\delta\nu_p = C\gamma. \tag{1.2.1}$$

This can be compared to the linewidth limitation due to phase noise induced by spontaneous emission into the cavity mode, commonly known as the Shawlow-Townes (ST) limited linewidth [50]. For a laser with a gain medium linewidth of γ and cavity linewidth κ it is defined as

$$\delta\nu_{\text{mST}} = \overbrace{\frac{\hbar\omega_l}{4\pi}\frac{\kappa^2}{P_{\text{out}}}}^{\text{org. ST}}\overbrace{\left(\frac{\gamma}{\gamma+\frac{1}{2}\kappa}\right)^2}^{\text{modified ST}}, \tag{1.2.2}$$

where P_{out} is the power output and ω_l is the lasing frequency. We have assumed that the cavity is on resonance with the gain medium. This is the modified Shawlow-Townes limit which also predicts the linewidth limit in the bad cavity regime [51]. In the bad cavity limit, where $\kappa \gg \gamma$, the ST limit reduces to

$$\delta\nu_{\text{mST,bad}} = \frac{\hbar\omega_l}{4\pi}\frac{\gamma^2}{P_{\text{out}}}. \tag{1.2.3}$$

At the time of writing, no group has reported a truly continuous superradiant signal, though several groups are pursuing an experimental realization [52–55]. In this thesis, I show and discuss the results of an experimental system designed to produce long superradiant pulses to provide an insight how the first few ms of lasing would behave in a truly continuous superradiant laser. We use the relatively broad 7.48 kHz ${}^0S_1 \rightarrow {}^3P_1$ transition in ^{88}Sr as the faster decay allows for more intense pulses and this linewidth should not limit the lasing linewidth on the timescales we expect to sustain lasing.

In parallel to investigating narrow linewidth superradiant lasing, we use the experimental system to realize a superradiant readout scheme for a Ramsey type interrogation [3], where the amplitude of the superradiant pulses can be used to determine the number of atoms in the excited state which in turn can be used to stabilize the pump laser frequency. The execution of such a readout is fast and less destructive to the atomic ensemble than traditional fluorescence measurements as it requires much fewer scattered photons. As such, it has intriguing applications to improve interrogation schemes of intracavity quantum emitters.

CHAPTER 2

Cold atoms in an optical cavity

In this chapter we will present the theoretical and historical background to provide the basic building blocks for understanding the physics that constitute this thesis. We will review some topics from atom cooling and trapping, cavity QED, and lasing dynamics.

2.1 The structure of strontium

Strontium is an alkaline earth metal that possesses useful transitions for laser cooling and narrow transitions for precision spectroscopy. The first experiments trapping and cooling strontium were realized in the end of the 1990's [56, 57], which led to the development of the first optical lattice clock [27, 28]. Strontium has four different naturally occuring isotopes; the bosonic ^{84}Sr (0.56% abundance), ^{86}Sr (9.86%), ^{88}Sr (82.58%), and the fermionic ^{87}Sr (7%) [58]. In our experiments, we work with the most abundant ^{88}Sr. This isotope has no nuclear spin, making it easy to cool and prepare large ensembles of atoms. In Fig. 2.1 we show the relevant transitions and levels of strontium.

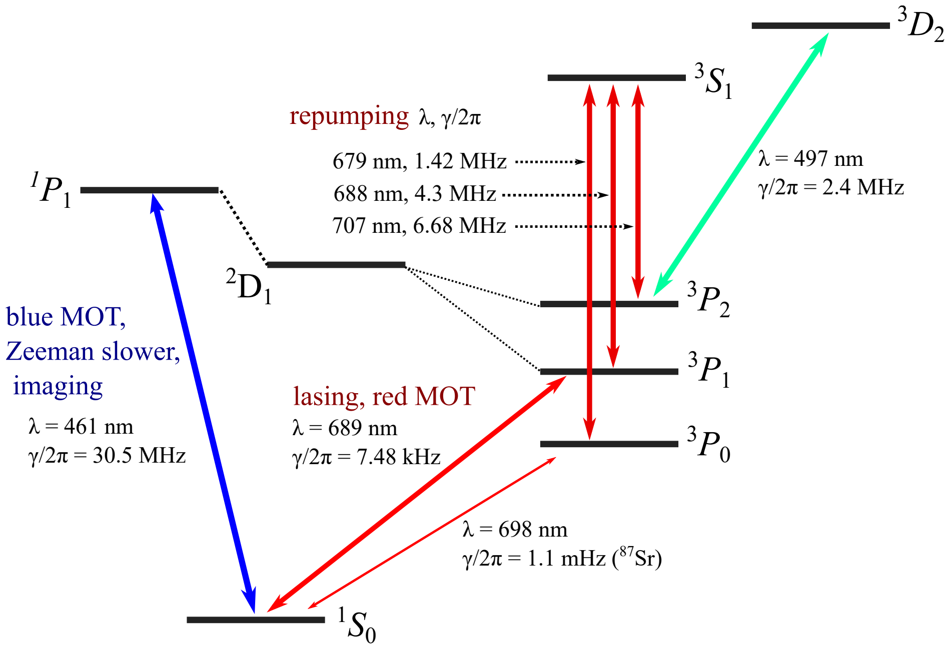

Figure 2.1: The relevant transitions in ^{88}Sr. The linewidths of the 679, 688 and 707 nm repumping transitions are partial.

The notation of each atomic state refers to the configuration of the two valence electrons in strontium using spectroscopic notation [59],

$$^{2S+1}L_J. \tag{2.1.1}$$

where S is the spin quantum number, which in strontium can be either be 0 or 1 for an antiparallel or parallel configuration of the spins, respectively. The term $2S+1$ is the spin multiplicity, which determines the number of spin projections along the quantization axis. L is the orbital quantum number in the spectroscopic notation, and $J = L + S$ is the total angular momentum quantum number. The coupling between the orbital angular momentum and the spin (the spin-orbit coupling) leads to a splitting of the levels for different J's, also commonly referred to as the fine structure. In strontium, the ^3P state is split into three levels with $J = 0, 1, 2$. When applying a magnetic field over an atom, the spin and angular momentum quantum number results in an additional splitting from its projections, m_j, along the magnetic field quantization axis. The splitting in energy for a weak magnetic field is given by [59]

$$\Delta E = g_j \mu_b B m_j, \tag{2.1.2}$$

where μ_b is the Bohr magneton, B is the magnetic field, and g_j is the Landé g-factor commonly defined as

$$g_j = \frac{3}{2} + \frac{S(S+1) - L(L+1)}{2J(J+1)}. \tag{2.1.3}$$

In strontium, this magnetic splitting is especially relevant for $^1P_1$ and $^3P_1$, as the splitting can create a confining force with a spatial dependence when atoms are moving in a magnetic field and illuminated with laser cooling beams.

In strontium, the $^1S_0 \rightarrow {}^1P_1$ 461 nm transition has a linewidth of 30.5 MHz [60, 61] which allows for efficient cooling and trapping. However, this transition is not completely closed, as $^1P_1$ has another, albeit much weaker, decay channel (Fig. 2.1). When an atom is excited to $^1P_1$, there is a 1:20000-50000 chance [1], that the atom will decay to $^1D_2$ [60], through which it will decay to $^3P_2$ or $^3P_1$. The $^3P_2$ state has a lifetime of 520 s [62], which means that the atom can no longer be optically cooled. However, the decay of atoms into the $m = +1, 2$ sublevels of $^3P_2$ can load a magnetic trap and reach relatively low temperatures due to thermalization and evaporative cooling [63].

---

[1] The actual fraction is still somewhat disputed. See the discussion in [60, p. 41]

To return the atoms into the 461 nm cooling cycle the atoms can be repumped from $^3P_2$ and $^3P_0$ using a 707 nm and 679 nm laser to the $^3S_1$ state (Fig. 2.1). From this state, the atoms can decay back to the $^3P_{2,1,0}$ states with a branching ratio of 5:3:1 [64]. If the atoms end up in $^3P_1$, they can decay back to the ground state and reenter the cooling cycle. The third repumper at 688 nm pictured in Fig. 2.1 is not used in the cooling cycle, but it is important for the repumping scheme of the superradiant laser we will consider later. As an alternative to the 679 nm and 707 nm repumpers it has been shown that a similar repumping efficiency can be achieved using just a single 497 nm coupling the $^3P_2$ and $^3D_2$ states [65, 66]. We shall discuss the 688 nm and the possible applications of a 497 nm repumper more in depth in chapter 6.

In ^{87}Sr, the commonly used clock transition is the 698 nm $^1S_0 \to {}^3P_0$ with a linewidth of just 1.1 mHz [26]. For ^{88}Sr, this transition is completely closed as the isotope has no nuclear spin, $F = 0$, but it can be opened and tuned with the introduction of a strong magnetic field. In our experiment, we opt to use the broader $^1S_0 \to {}^3P_1$ intercombination line at 689 nm with linewidth $\gamma_l/2\pi = 7.48(1)$ kHz (and associated lifetime of the excited state $\tau = 21.28(3)$) [67] for lasing experiments [2], as the demands on the lasers are relaxed which allows for simpler experimental setups and the stronger single atom decay rate makes it easier to observe superradiance. Using this transition over the mHz transition in ^{87}Sr should not put a linewidth limitation on the superradiant light on the time scales (3-4 ms) we expect to produce lasing [49].

The $^1S_0 \to {}^3P_1$ 689 nm transition is crucially used for cooling of the atomic ensemble. When cooling and trapping using the 461 nm $^1S_0 \to {}^1P_1$ transition, the ensemble typically has a final temperature of a few mK. Using the $^1S_0 \to {}^1P_0$ 689 nm transition, the temperature can be brought down to just a few µK. This can place the system firmly in the bad cavity regime, where the lasing is insensitive to cavity vibrations.

The $^3P_1$ state has three magnetic sublevels $m = 0, \pm 1$ with an energy splitting of 1.4 MHz/G between each level. We use the magnetically insensitive $m = 0$ for lasing, and the $m = \pm 1$ states are used for trapping and repumping. The magnetic sublevels can also be addressed from $^1S_0$ specifically using either circularly or linearly polarized light, which is useful for repumping the atoms without addressing the lasing state.

---

[2] Though we commonly just quote $\gamma_l/2\pi = 7.5$ kHz

2.2 The scattering force

The 90's saw a rapid development of schemes to catch and control ensembles of multiple species of cold neutral atoms [68–70]. Such techniques primarily rely on the on preferential absorption of photons to systematically remove the kinetic energy of atoms. Following the derivations of [59], the scattering force on a two level atom illuminated by a monochromatic field is given by

$$F_{\text{scatter}} = \hbar k \frac{\gamma}{2} \frac{I/I_{sat}}{1 + I/I_{sat} + 4\delta^2/\gamma^2}, \tag{2.2.1}$$

where γ is linewidth of the excited state, I_{sat} is the saturation intensity of the transition, and δ is the detuning from atomic resonance. Intuitively, the scattering force increases if the atomic transition has a faster decay - the spontaneous emission creates a non-conservative force that removes energy from the system, and if the atoms spontaneously decay faster, they can absorb more photons over time. For $\delta = 0$ and $I \gg I_{sat}$, the scattering forces converges towards

$$F_{\text{scatter}} = \hbar k \frac{\gamma}{2}, \tag{2.2.2}$$

which is the momentum of a photon $\hbar k$ applied at half the spontaneous emission rate. In the high intensity limit, half the atoms will be in the excited state. For a specific transition in an atom with a mass m, the maximum acceleration due to photon scattering can be written as

$$a_{\max} = \frac{\hbar k}{m} \frac{\gamma}{2} = \frac{v_{\text{recoil}}}{2\tau}, \tag{2.2.3}$$

where τ is the lifetime of the transition, and v_{recoil} is the change in velocity from the absorption of a photon on the transition. This maximum acceleration is important to consider when designing a system to slow a thermal beam of atoms, as it results in a minimum stopping distance L_0. In our system, we slow thermal beam of atoms travelling with $300 - 500$ m/s by scattering photons on the 461 nm $\gamma = 30.5$ MHz $^1S_0 \rightarrow {}^1P_1$ transition using a laser beam counter-propagating with respect to the atoms. A typically quoted value for L_0 with $I \approx I_{\text{sat}}$ is around $25 - 35$ cm [71]. However, this assumes that the atoms experience a constant acceleration - the reality is that as the atoms are slowed, the resonance condition changes due to Doppler shifts. The atoms only experience a strong scattering force when the effective field frequency is within the atomic transition line shape.

To counter the varying Doppler shift, the scattering force can be engineered to remain reasonably constant. By using a magnetically sensitive state such as ${}^1P_1, m = \pm 1$ and varying the magnetic field $B(z)$ along the slowing direction, the Doppler shift shift can be cancelled out by the magnetic shift,

$$\frac{\mu_B B(z)}{\hbar} = kv, \tag{2.2.4}$$

assuming that the field frequency is on resonance with atoms at rest. The required field profile becomes

$$B(z) = B_0\sqrt{1 - z/L_0} \tag{2.2.5}$$

where

$$B_0 = \frac{hv_0}{\lambda\mu_b}. \tag{2.2.6}$$

This setup is known as a Zeeman slower and is an important and common first cooling stage in strontium experiments. Without the Zeeman slower cooling beam, the number of atoms we can prepare for experiments is orders of magnitude lower. Turning on the magnetic field in the Zeeman slower coil, we typically gain an additional factor of two in atom number. If the power of the Zeeman slower beam is low, the loading rate of the optical trap after the Zeeman slower is best when the Zeeman slower coil is running at a low current. The interpretation is that a Zeeman slower operating with a low optical power provides an insufficient scattering force to follow the magnetic field gradient in the Zeeman slower.

2.3 The magneto-optical trap (MOT)

We use the scattering force in conjunction with carefully tuned magnetic fields for localized trapping and cooling of atoms. Instead of slowing in a single direction, we set up an arrangement of 6 lasers at the end of the Zeeman slower. The laser beams are intersecting in a single point and organized such that atoms gets slowed in all three dimensions, realized by retroreflecting 3 laser beams. The atoms get confined to a center defined by the zero point of a quadropole magnetic field. This technique is referred to as a magneto-optical trap (MOT), and it is the workhorse of many experimental quantum physics experiments. In ^{88}Sr, the first MOT stage is commonly realized using the ${}^1S_0 \rightarrow {}^1P_1$ transition at 461 nm with a linewidth of 30.5 MHz. Two magnetic coils arranged in an anti-Helmholtz

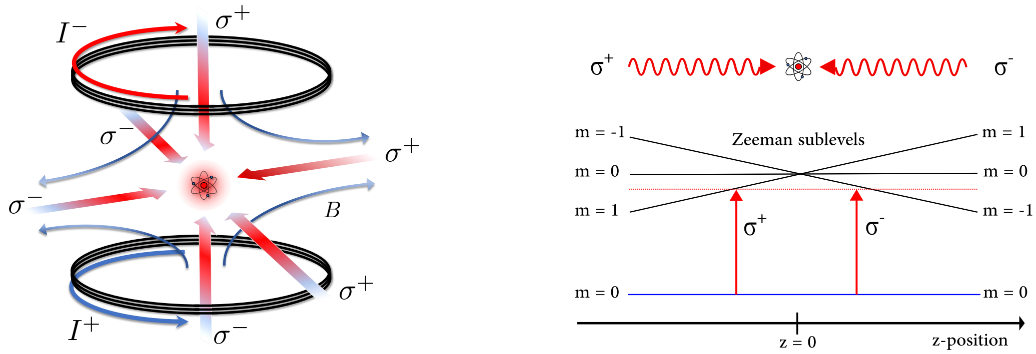

Figure 2.2: Simple schematic of a magneto-optical trap (MOT). Counter-propagating circularly polarized laser beams interact with Zeeman-shifted magnetic sublevels to create a spatially dependent restoring force that simultaneously cools the atoms. Figure from [72].

.

configuration form a anti-symmetric magnetic field with a zero point near the geometric center of the magnetic coils. Three orthogonal pairs of counter-propagating MOT laser beams (Fig. 2.2) operating at a frequency just below atomic resonance are overlapped near the geometric center of the magnetic coils. Each antiparallel pair of laser beams have opposite circular polarization [3] to address a specific magnetic sublevel of $^1P_1$. The Zeeman effect breaks the degeneracy of the three different angular momentum states of $^1P_1$, putting the MOT beams closer to resonance with the $m_j = \pm 1$ magnetic substates. Atoms within the intensity profile of the MOT beams will preferentially absorb photons from one of the 6 MOT beams, but will spontaneously emit in a random direction, resulting in an average effective force directed towards the magnetic field center. The theoretical lower limit on the temperature in a MOT is given by the Doppler limit [59]

$$k_B T_D = \frac{\hbar\gamma}{2}, \tag{2.3.1}$$

which for the 461 nm MOT $T_D \approx 770$ µK. This is using that $\delta = \gamma/2$, and $I \ll I_{\text{sat}}$, which means that the force from each MOT beam can work independently. In reality, it can be an advantage to increase the MOT detuning to increase the capture velocity of atoms. The working principles for a second state MOT using the 689 nm $^1S_0 \rightarrow {}^3P_1$ transition are exactly the same, except the linewidth of the transition is much narrower at 7.5 kHz. This provides a much lower trapping force and a smaller capture range, but the Doppler limit

---

[3] If the polarization is defined with respect to the k-vector, the beam and its retroreflection have the same polarization.

permits a much lower temperature of the ensemble, $T_D = 180$ nK.
It should be mentioned that the two level treatment of the cooling scheme often is often insufficient to describe the performance of a MOT. As it turns out, atoms with more complex ground state structures than ^{88}Sr can simoultaneously be cooled through other processes than photon scattering from the MOT beams. Atoms with magnetically sensitive ground state sublevels (such as Alkalis) can instigate Sisyphus cooling [73] when the atoms move around the sinusoidally varying potential landscape in the standing wave of the MOT beams [59]. The first realizations of Alkali MOT's saw temperatures much lower than the Doppler temperature [74].

2.4 Atomic state manipulation

In the previous section we used the direct drive between two atomic levels to produce a non-conservative force to cool an ensemble of atoms. When cooling atoms, we are incoherently driving them - the spontaneous emission is important as it removes the thermal energy from the atoms. However, in this section we concern ourselves with coherent population manipulation. If the atoms are driven with a uniform field intensity on time scales shorter than the natural lifetime of the excited state, the direct drive on the lasing transition can generate brief but strong population inversion. This can be leveraged to produce short (shorter than τ) but intense superradiant bursts.

2.4.1 Rabi oscillations

To achieve lasing in the ensemble of cold strontium atoms, we need population inversion. That is, more than half the atoms must be in the excited state. In the semiclassical model, illuminating a two-level atom with a monochromatic electric field, the time evolution of the probability to find the atom in the excited state can be written as the solution to the Schrödinger equation [75],

$$P_e = \frac{\Omega^2}{W^2} \sin\left(\frac{Wt}{2}\right)^2, \tag{2.4.1}$$

for an atom initially in the ground state ($P_g = 0$), and with $W^2 = \Omega^2 + \Delta^2$, where Δ is the detuning of the E-field from atomic resonance. The Rabi frequency Ω is defined by

$$\Omega = \frac{\langle 1|\, e\mathbf{r} \cdot \mathbf{E}_0 \,|2\rangle}{\hbar}, \tag{2.4.2}$$

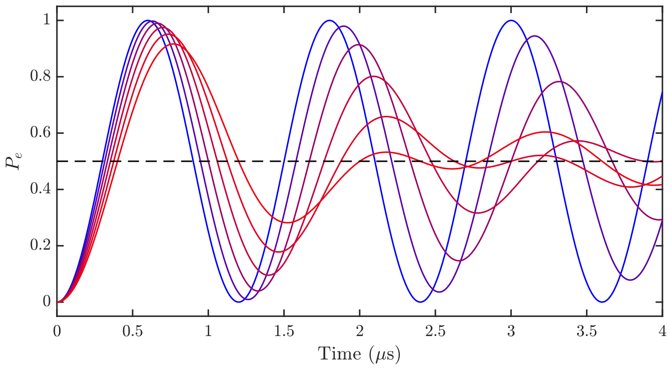

Figure 2.3: Rabi oscillations of an ensemble of atoms. The atoms experience different pulse intensities, which is translated into an effective Rabi frequency $\alpha\Omega$, where $\Omega = 2\pi \cdot 833$. From blue to red, α is uniformly distributed in the interval $[n, 1]$ where $n = [1, 0.9, 0.8, 0.7, 0.6, 0.5]$. For $n = 1$, the flopping is completely coherent as described by Eq. 2.4.1.

where $e\mathbf{r}$ is atomic dipole moment moment. For $\Delta = 0$, the atom can be driven perfectly between the ground and excited state. As the atom is driven between the excited and ground state, no net force is actually exerted on the atom - this is because the atom-light interaction alternates between absorption and stimulated emission. The atom will experience a scattering force along the direction of the driving field only when spontaneous emission is included (as we discussed in the previous section). When the atom is illuminated for a time $t = \pi/\Omega$, the atom will be in the excited state. This is what we refer to as a π pulse. We use such pulses to create large population inversion in the atomic ensemble, to observe short superradiant bursts in our atom cavity system. The π pulses can only be near perfect as any kind of difference in the effective detuning or Rabi frequency of each atom in the ensemble will create decoherence. The intensity profile of the laser used to drive the atoms is rarely perfectly uniform, and some atoms might be screened due to a high optical density of the cloud. The non uniform intensity profile is not the only thing causing decoherence when pumping the atoms directly on the lasing transition; the spontaneous emission and the varying Doppler shift of each atoms also contributes to the decoherence However, on the timescales of the π pulse, we suggest that the intensity profile is the dominating source of decoherence in the ensemble flopping.

Instead a fitting the population oscillation using just one Ω as in Eq. 2.4.1, the time evolution of the system can be described using a distribution of different Rabi frequencies as experienced by atoms subjected to a non uniform intensity profile [4],

$$P_e = \int_0^1 d\alpha f_A(\alpha) \frac{\alpha\Omega}{\sqrt{(\alpha\Omega)^2 + \Delta^2}} \sin\left(\frac{t\sqrt{(\alpha\Omega)^2 + \Delta^2}}{2}\right). \tag{2.4.3}$$

The variable α is unitless and $\in [0, 1]$, and Ω_R is here defined at the maximum Rabi frequency of the ensemble. The function $f_A(\alpha)$ is the probability distribution of different α's accross the cloud. If $f_A(\alpha) = \delta(\alpha - 1)$, that is, the atoms experience only one Rabi frequency, then Eq. 2.4.3 reduces to Eq. 2.4.1. In Fig. 2.3 we plot different transfer efficiencies for an ensemble of atoms. We have assumed a uniform distribution $f_A(\alpha)$ of $\alpha \in [n, 1]$ where $n = [1, 0.9, 0.8, 0.7, 0.6, 0.5]$, (blue to red graphs). We assume that $\Delta = 0$ and have used a typical Rabi frequency for our system, $\Omega = 2\pi \cdot 833$ kHz. We have marked the threshold for superradiant lasing, around $P_e = 0.5$, with a dashed black line. If the atoms experience Rabi frequencies that vary by a factor of two ($\alpha \in [0.5, 1]$), the flopping coherence will be almost completely gone after just a fewµs. More importantly, the maximum amplitude of the population oscillations is decreased. Other probability distributions $f_A(\alpha)$ of α can readily be used. If the pumping beam has a waist that is comparable to the size of an atomic cloud with a Gaussian distribution, the variations of the pumping intensity will be dominated by variation of the Gaussian intensity profile. For this, the probability function is [4]

$$f_A(\alpha) = \frac{w_0^2}{2\sigma^2} \alpha^{\frac{w_0^2}{2\sigma^2} - 1}. \tag{2.4.4}$$

In our experiment the pumping beam is much bigger than the cloud, such that most fluctuations in the intensity profile will originate from atomic screening effects or inhomogeneities in the beam profile inherited from optical elements in the beam path.

This theory is useful for gaining an intuition on how to achieve population inversion to produce short, superradiant bursts. However, this population inversion is only brief and cannot be sustained when lasing on the same transition that we pump to excite the atoms. To produce longer pulses than those originating from a population inversion (π pulse), we need to continuously reload atoms into the excited state using multiple atomic levels.

2.4.2 Multilevel laser

We touched briefly upon classical laser schemes in the introduction, and now we will discuss some of the theory of generalized 3-level and 4-level lasers to understand the behavior of our system when we start repumping atoms to prolong the lasing pulses. We will follow

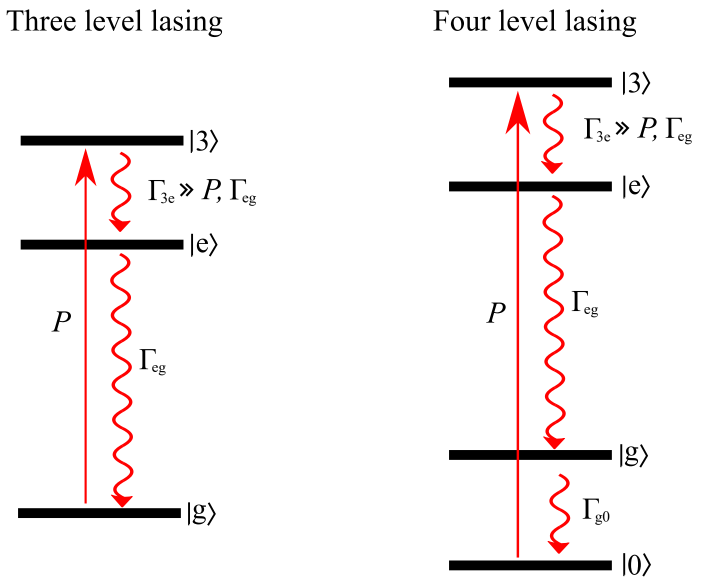

Figure 2.4: Generalized 3-level and 4-level lasing systems.

and discuss the definitions and conclusions outlined in [76].

The fundamental problem that various laser schemes address is that it is complicated to sustain population inversion of an atomic ensemble using just a single transition. When atoms are driven coherently between the ground and excited state, we can initially expect to periodically see more than 50% of the atoms in the excited state on timescales shorter than the decoherence time of the system. This decoherence can originate from either the excited state decay, pump pulse intensity variations, or varying level shifts across the atomic ensemble. When trying to sustain population inversion in an incoherent ensemble of atoms, the stimulated emission from the atoms in the excited state will cancel out the absorption of the atoms in the ground state, and when increasing the power the excited state population simply converge towards 50%. Using a third atomic state that has a fast decay to the excited state is a way to excite atoms without also removing atoms from the excited state (Fig. 2.4), and the first realization of a laser used a three level structure in ruby [77]. To describe such a system, we define the atom number in the ground and excited state as N_g and N_e, respectively. We write the population rate equations for the ground and excited lasing state as [76]

$$\frac{dN_g}{dt} = -PN_g + \Gamma_{eg}N_2 + \sigma\Phi(N_e - N_g), \tag{2.4.5}$$

$$\frac{dN_e}{dt} = PN_g - \Gamma_{eg}N_2 - \sigma\Phi(N_e - N_g). \tag{2.4.6}$$

where σ is the absorption cross section and Φ is the photon flux. The atoms are pumped from the ground state to the excited state through the third level at a rate P. We have assumed that the population N_3 decays to the excited state at a rate $\Gamma_{3e} \gg P, \Gamma_{eg}$, where Γ_{eg} is the rate of spontaneous emission from the excited state to the ground state. The last term in each equation is the stimulated emission and absorption, which depends on the population inversion $\Delta N = N_e - N_g$. Assuming steady state operation, we can take the time derivatives to be zero. Additionally, we assume that the photon flux is low $\Phi \approx 0$ to define the steady state values of N_g and N_g,

$$\overline{N_e} = \frac{P}{\Gamma_{eg}}\overline{N_g}. \tag{2.4.7}$$

From this, it is evident that in a three level lasing scheme the pumping rate must be bigger than the natural decay rate of the excited state,

$$P > \Gamma_{eg}, \tag{2.4.8}$$

to achieve steady state positive population inversion $\Delta N > 0$. At the threshold pumping power $P_{\mathrm{min}} = \Gamma_{eg}$, half of the atoms in the ensemble are in excited state and half are in the ground state. The pumping needs to counter the spontaneous emission of half the ensemble of atoms, which means that the ensemble on average scatters many photons to sustain the population inversion. This is an important thing to note for our applications of this theory, but for now we stick with a discussion of the generalized theory.

Today most laser schemes involve at least four levels. This is to decouple the depumping of the lower lasing level with the excited state population, which allows for much lower pump powers before lasing threshold is reached. We add a level below the lower lasing level, $|0\rangle$ (Fig. 2.4). The lower lasing level decays to $|0\rangle$ with a rate Γ_{g0}, and the pump now transfers atoms from $|0\rangle$ to $|3\rangle$. Using the same approach as with the three level system, the steady state population inversion can be approximated as [76]

$$\Delta_N = \frac{P(\Gamma_{g0} - \Gamma_{eg})(N_0 + N_g + N_e)}{\Gamma_{g0}\Gamma_{eg} + \Gamma_{g0}P + \Gamma_{eg}P}. \tag{2.4.9}$$

Now, for a non zero pumping rate the population inversion will always be positive if $\Gamma_{g0} > \Gamma_{eg}$. The addition of a fourth level has the consequence that only of the fraction of the atoms needs to actively contribute to sustain the population inversion, which allows for much lower pump powers. This is an important feature in systems where it is desirable to retain low pump powers, e.g. to limit photon recoils and residual light shifts of the lasing levels. Such considerations are important to consider when trying to produce a long steady state superradiant lasing signal.

2.5 Cavity QED

The heart of the experiment and this thesis as such is the interaction between an optical cavity and an ensemble of atoms, the study of which is commonly referred to as cavity quantum electrodynamics (cQED). Cavities are widely used in AMO physics for laser stabilization, to increase the interaction strength of atoms, and to form optical lattices with enhanced power and smooth, averaged wavefronts.

In recent times focus has increased on studying the interaction of an atomic ensemble coupled to a cavity. Atom-cavity interactions have a broad variety of applications, such as entanglement generation, quantum sensing, and, relevant for this thesis, the study of collective effects in an intracavity atomic ensemble. The cavity can enhance the interaction between individual atoms and create a preferred emission axis that is useful for producing and characterizing superradiant bursts. This lowers the requirements for creating interactions between atoms as compared to producing superradiant bursts in free space.

2.5.1 The bare cavity system

An optical cavity is an arrangement of mirrors that can (depending on the configuration) form a running or standing wave electromagnetic field. Here, we will consider the simple - and most commonly used in our laboratory - Fabry-Perot configuration, where two mirrors face each other. If the distance between mirrors is an integer times half the wavelength, coupling light through one of the mirrors will create a standing wave between the two coated surfaces, building up the optical power in the intracavity field. From this requirement, we can infer what is commonly refereed to as the free-spectral range (FSR) of the cavity, the frequency difference between allowed identical transverse modes in the optical cavity,

$$\mathrm{FSR} = \frac{c}{2L}. \tag{2.5.1}$$

For the bare cavity, the most important factor deciding the cavity's behavior is the transmission and loss coefficients for the mirrors. High mirror reflectivities with low loss results in long lifetimes for photons resonating between the mirrors. This makes the cavity more frequency selective, and it is desirable for schemes stabilizing the frequency of a laser to the length of the cavity. The cavity transmission spectrum is an Airy-function [78], but for mirror reflectivities $r \approx 1$ it is a good approximation to write the transmission of the cavity as a Lorentzian lineshape,

$$L(\omega) = A\frac{(\frac{1}{2}\kappa)^2}{(\omega - \omega_0)^2 + (\frac{1}{2}\kappa)^2}, \tag{2.5.2}$$

where ω is the frequency of the laser coupled to the cavity, and κ is defined as the linewidth of the cavity. Using the linewidth of the cavity and the FSR, we define the finesse $\mathcal{F}$,

$$\mathcal{F} = \frac{\mathrm{FSR}}{\kappa}. \tag{2.5.3}$$

which quantizes the loss of photons from the intracavity field per round trip, analogue to the Q-factor of a generalized harmonic oscillator. The finesse can be used to describe the power enhancement of the circulating field in the cavity

$$E_{\mathrm{circ}}^2 = \frac{\mathcal{F}}{\pi}E_0^2, \tag{2.5.4}$$

where E_0^2 is the magnitude of the input field coupled to the cavity. Figure 2.5 shows an example of the frequency dependent intracavity power as a function of cavity finesse.

These considerations are only immediately useful when considering light coupled to an empty cavity. Or, more generally, for light resonating at a wavelength where it does not experience significant absorption or a phase shift from an intracavity ensemble of atoms.

2.5.2 The atom-cavity system

We now move away from the purely classical treatment of our system, to coupling an intracavity ensemble of N atoms with an atomic transition close to the resonance of one of

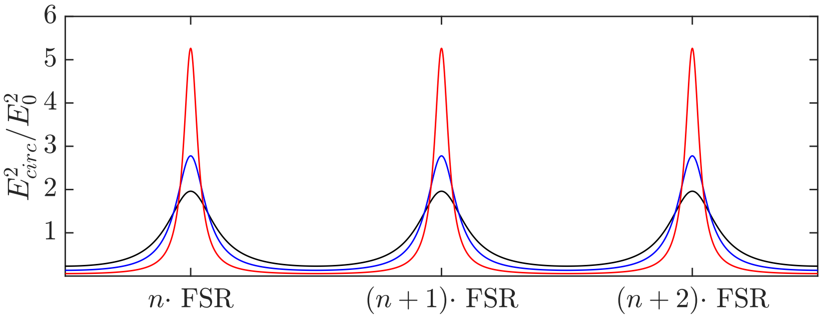

Figure 2.5: Intracavity circulating power of an optical Fabry-Perot cavity as a function of laser frequency, for a finesse of $\mathscr{F} = 10$ (black), $\mathscr{F} = 15$ (blue) and $\mathscr{F} = 30$ (red).

modes of the optical cavity. The atoms are randomly distributed along standing wave of the cavity field. When the atom-cavity cavity system is subjected to a weak probe, and number of atomic excitations is less than the number of atoms, we can describe such a system by writing the modified Jaynes-Cummings Hamiltonian in the rotating frame [79–81],

$$\hat{H} = \hbar\delta_{cav}\hat{c}^\dagger\hat{c} + \hbar g\sqrt{N}(\hat{a}\hat{c}^\dagger + \hat{c}^\dagger\hat{a}) \tag{2.5.5}$$

where δ_{cav} is the detuning of the cavity from atomic resonance, $\hat{c}$, $\hat{c}^\dagger$, $\hat{a}$, and $\hat{a}^\dagger$ are annihilation and creation operators for photons in the cavity field and atomic excitations (respectively). This is only a valid description when the system is subjected to a weak probe, such that a majority of the atoms are in the ground state. The last two terms are responsible for exchanging excitations between the cavity and the atoms at a rate $\Omega_N = 2g\sqrt{N}$ [82]. The single atom coupling g depends only geometric properties of the cavity as well as atomic properties, but the effective coupling varies as a function of longitudinal position within the cavity (z), going from no coupling to maximum interaction strength between the nodes and anti nodes of the cavity field. The transverse position perpendicular to the cavity axis (r) we model with a Gaussian distribution, assuming fundamental Gaussian cavity mode. Combining this, we write [83]

$$g(z,r) = \overbrace{\sqrt{\frac{6c^3\gamma\omega_c}{w_0^2 L\omega_0^3}}}^{g_0} \times \overbrace{\sin k_c z}^{\text{longitudinal}} \times \overbrace{\exp(-\frac{r^2}{w_0^2})}^{\text{transverse}}\,. \tag{2.5.6}$$

The maximal cavity coupling for a single atom we define as g_0, and it depends on the linewidth of the atomic transition γ, the cavity resonance frequency ω_c, the waist of the

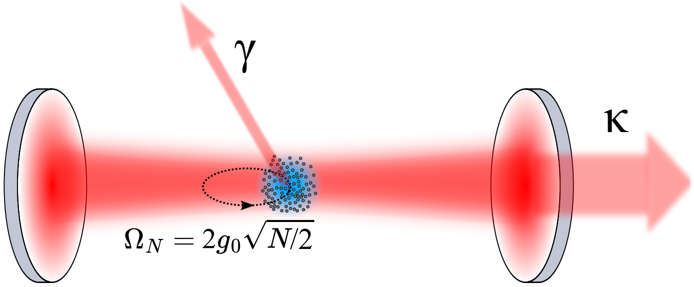

Figure 2.6: The atom cavity system with relevant dissipation rates. Excitations are exchanged between the atoms and the cavity field with a frequency Ω_N.

cavity w_0, the length of the cavity L, and the atomic transition frequency ω_0. For an atom cloud smaller than the waist of the cavity mode, the transverse distribution can be ignored, and we can define an average coupling strength in terms of g_0 by averaging over the sinusoidally varying cavity coupling of the standing wave cavity field, $\overline{g^2} = g_0^2/2$ [61, 84]. This definition of the average coupling strength lets us define the effective Rabi frequency of the atom-cavity system [85], the oscillation of energy between the cavity field and the atoms excitations, as

$$\Omega_N = \sqrt{2} g_0 \sqrt{N}. \tag{2.5.7}$$

$$= 2g_0 \sqrt{N/2} \tag{2.5.8}$$

The enhancement of the Rabi frequency due to $\sqrt{N}$ is possible through atom-atom interactions mediated by the cavity mode, and Ω_N is an important figure of merit to determine which regime the system operates in. In the strong coupling regime, the Rabi frequency is bigger than other relevant decoherence rates in the system, $\Omega \gg \kappa, \gamma$ (loss from cavity mirrors or single atom decay into free space). This collective Rabi frequency can be observed in the time-domain as an oscillation in the cavity field, or in the frequency domain as a splitting in the resonance condition of the cavity (which we shall discuss in the next section).

The strength of coupling between a single atom in the ensemble and the cavity mode relative to free-space modes is described using a metric known as the cavity cooperativity,

$$C_0 = \frac{(2g_0)^2}{\kappa\gamma}, \tag{2.5.9}$$

where the coupling strength of the atom-cavity system g_0 is compared to the dissepation rates κ and γ. For a low cooperativity $C_0 \ll 1$ a single excited atom is likely to emit a photon into free space rather emitting into the cavity mode (Fig. 2.6). The single atom cooperativity is an important figure of merit when considering cavity design for a superradiant laser. It can be easier to go above lasing threshold using a cavity with a high cooperativity, but it increases the Purcell linewidth limit $\Delta\nu_p = C_0\gamma$ [86].

The strength of the atom-cavity interaction can be improved by introducing N intracavity emitters, which results in collective effects of the atoms mediated by the cavity mode,

$$C_N = NC_0 = N\frac{(2g_0)^2}{\kappa\gamma}, \tag{2.5.10}$$

which can greatly enhance the effective cooperativity depending on the atom number. The collective behavior plays a central role in most of the physics presented in this thesis. In our cavity, we operate with a low single atom cooperativity, but due to a high atom number, we find ourselves in the collective strong coupling regime. This means that can exceed the lasing threshold yet theoretically reach very narrow lasing linewidths.

2.5.3 Normal mode splitting

To determine which regime the system operates in we can probe the atoms through the cavity. In the strong coupling regime the cavity transmission is split into two transmission peaks, commonly referred to as the normal mode splitting (NMS) [87, 88][4]. In simple terms, the NMS is the result of the interplay between the dispersion curves of the atomic ensemble and the cavity. The atomic ensemble causes a phase shift of the intracavity field, which for a specific laser detuning counteracts the detuning of the cavity resonance. This results in two frequency solutions for coupling light to the cavity.

The resonance frequencies of the combined atom-cavity system and their splitting can be found as the eigenstates of the Jaynes-Cummings Hamiltonian [82], and they are governed by the detuning of the cavity from atomic resonance $\delta_{\text{cav}} = \omega_c - \omega_{eg}$ and the collective Rabi frequency Ω_N [89],

---

[4] Also

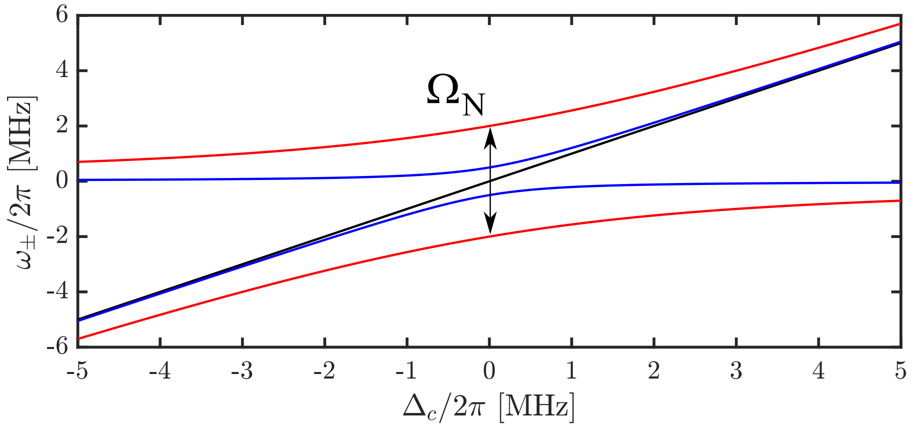

Figure 2.7: Normal mode splitting for $\Omega_N = 0, 2, 4$. At $\delta_{\mathrm{cav}} = 0$, the splitting is Ω_N, and the atom number can be inferred if g_0 is known.

$$\omega_\pm = -\frac{1}{2}\delta_{\mathrm{cav}} \pm \frac{1}{2}\sqrt{\delta_{\mathrm{cav}}^2 + \Omega_N^2}. \tag{2.5.11}$$

The shape of this is an avoided crossing of the atomic resonance (Fig. 2.7). In this figure, we have plotted the NMS for $\Omega_N = 0, 2, 4$ MHz (black, blue and red respectively). For $\Omega_N = 0$, the only solution follows the cavity detuning as there is no atom-cavity interaction. As Ω_N increases, the frequency splitting of the two solutions gets bigger, especially around atomic resonance. If the cavity is on atomic resonance $\delta_{\mathrm{cav}} = 0$, these allowed modes are placed at $\pm\Omega_N/2$. Since Ω_N depends on $\sqrt{N}$, the NMS provides an extremely useful measure of the total number of atoms interacting with the cavity mode. This can be used to probe the atom number non-destructively before we generate a superradiant pulse.

Chapter 3

Experimental apparatus

In this chapter, the experimental setup and its development is discussed. Before the start of my PhD, the Strontium 1 machine had been used to investigate the coupling between mK cooled ^{88}Sr atoms and a low finesse cavity. Namely, the system was used to demonstrate how nonlinear dispersion can be utilized for a passive laser stabilization scheme using the NICE-OHMS technique [41, 90, 91]. Later the cavity was swapped to increase the finesse, which enabled intense superradiant bursts in the crossover regime [45] that demonstrated immunity to cavity fluctuations [92].

In 2019 when I started my PhD the experiment was due for a significant upgrade. The biggest planned change to the experiment was the implementation of a second MOT cooling stage on the narrow $^1S_0 \rightarrow {}^3P_1$ transition to make the atoms reach much lower temperatures. Previously, the experiment operated in the crossover regime, where the cavity linewidth is similar to the homogeneous broadening of the atomic ensemble. However, a red MOT would make the system operate in the bad cavity regime, where the lasing frequency is dictated by the atoms frequency rather than the intra-cavity field. This chapter is sectioned into the various components and techniques that goes into the experiment, whereas most have been implemented or upgraded during my PhD. The layout of the experiment is depicted in Fig. 3.1.

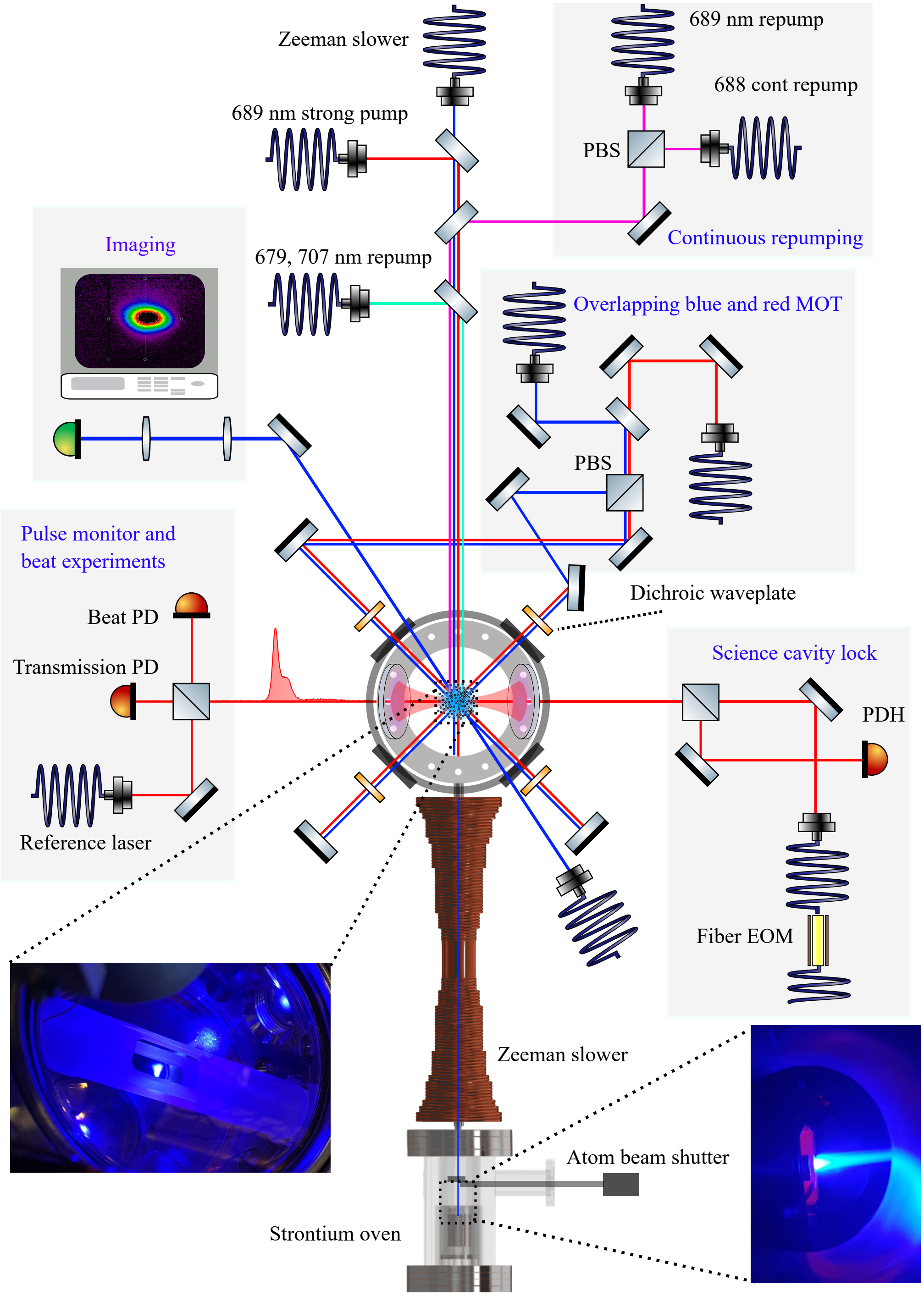

Figure 3.1: Schematic of the experimental setup as seen from above.

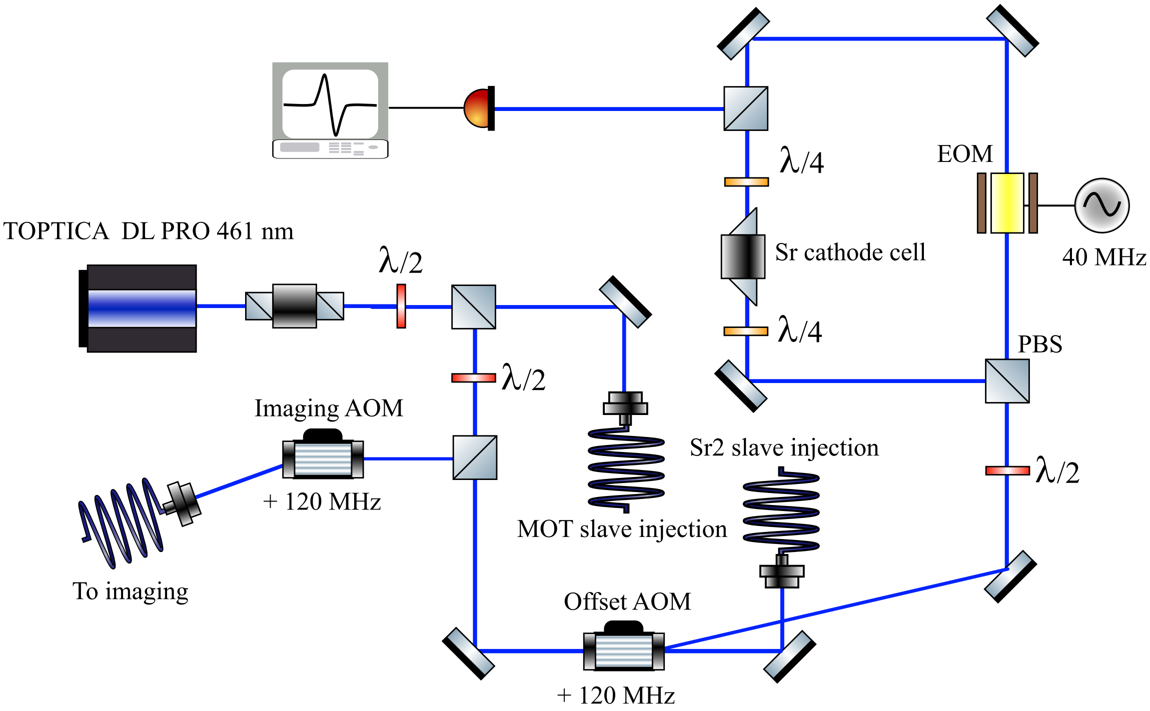

Figure 3.2: Layout for the blue reference laser optics. We use the light for imaging and to inject 461 nm laser diodes in our own and our neighbouring experiment. The light is locked using modulation transfer spectroscopy in a strontium cathode cell.

3.1 461 nm laser systems

The first atom light interaction in the experimental sequence happens on the $^1S_0 \rightarrow {}^1P_1$ 461 nm transition. We use the 461 nm light in the Zeeman slower, the blue MOT, and for imaging the atomic cloud. The low lifetime of the $^1P_1$ state permits a large scattering rate suitable for slowing thermal atoms and producing absorption images. The 461 nm reference light is generated using a Toptica DL PRO 461 nm, capable at outputting 120 mW. This light is used for the imaging systems and to inject other 461 nm diodes, and it is locked to an atomic reference (a Hamamatsu strontium cathode cell generously donated by the Ye group). The layout of the blue reference laser breadboard is depicted in Fig. 3.2. After the first optical isolator, we pick off $\approx$ 20 mW to inject the dedicated 461 nm MOT and Zeeman slower diode. From this, we usually fiber couple $\approx$ 8 mW, which is more than enough for a good and stable diode injection. A similar amount of power is sent to our neighboring experiment ”strontium 2” to inject their ”grandfather” laser diode.

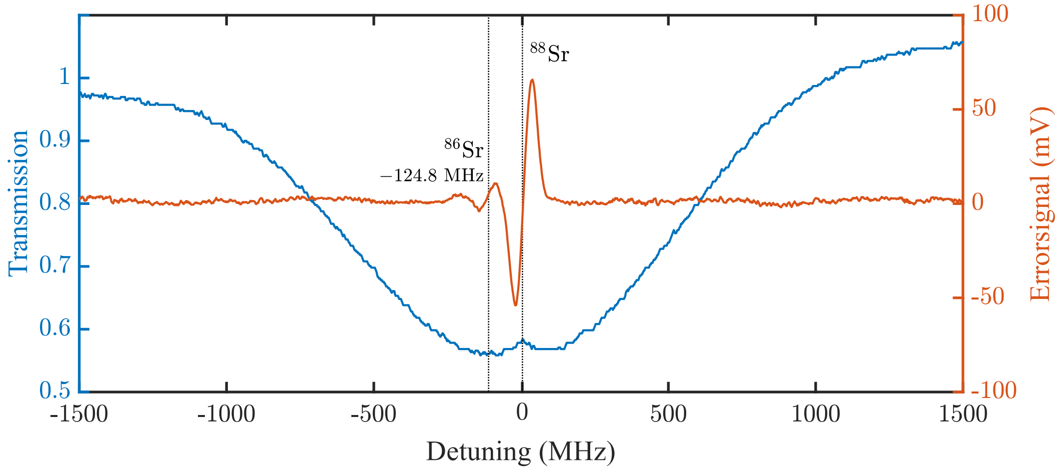

Figure 3.3: The errorsignal generated using saturated modulation transfer spectroscopy. In blue, the absorption of the probe with a visible saturation peak in the bottom of the absorption bowl. In red, the errorsignal generated by demodulating the probe light. The ^{86}Sr isotope is visible in the errorsignal with a detuning of −124.8 MHz compared to the ^{88}Sr resonance.

The imaging light is generated by shifting the 461 nm light with +120 MHz and fiber coupling the diffracted beam. We use ≈ 500 µW through the fiber in 20 − 50 µs imaging pulses. We derive the imaging light directly from the TOPTICA (rather than a high power injected diode) as the spectral purity is important when imaging dense atomic clouds. The imaging setup will discussed in greater detail in chapter 4.4.

3.1.1 Blue reference locking

The reference light intended for frequency locking the laser is shifted by +120 MHz by an AOM ("offset AOM"), such that the blue reference light has a detuning of −120 MHz to atomic resonance when locked. Locking the laser off resonantly simplifies using AOMs for simultaneous frequency shifting and shuttering further downstream. The diffracted beam from the offset AOM is guided through a polarizing beam splitter (PBS), where the transmission and reflection becomes the pump and probe beam in a modulation transfer spectroscopy scheme [93, 94]. The pump beam is phase modulated using an EOM. When the pump and probe beam overlaps within the strontium cathode cell, the pump beam transfers its phase modulation to the probe beam through an interaction with the atomic medium. Demodulating the probe beam at the EOM modulation frequency then generates an errorsignal to stabilize the blue reference laser. This scheme combines the benefits of saturated absorption spectroscopy (SAS) and frequency modulation (FM) spectroscopy to produce a high signal to noise Doppler-free spectroscopy signal from interrogating hot strontium atoms in a cathode cell. This scheme is a significant improvement over our previous setup where the SAS signal was produced by interrogating a hot atom beam from a reference oven in a different vacuum chamber.

We run the cathode cell at 400V. This is sufficient to produce an errorsignal with a high signal-to-noise. If the voltage is increased further, the cathode cell starts exhibiting unstable behavior, turning on and off every other second. Figure 3.3 shows an example of the locking signal generated with the cathode cell. In red, the demodulated signal forming the anti symmetric feature for frequency stabilization. In blue, the transmission of the probe beam. The transmission has a Doppler width of more than a GHz, but the errorsignal is generated in the region where the pump and probe interact with the same atomic velocity classes in the cathode cell. The interplay between the pump and probe beams creates the saturation peak visible at the bottom of the absorption bowl. The isotope ^{86}Sr (9.86% abundance) is also visible in the errorsignal. In ^{86}Sr the 461 nm transition is shifted with -124.8 MHz compared to ^{88}Sr [60].

3.1.2 Blue MOT and Zeeman slower

The blue MOT beams and the Zeeman slower beam are derived from an injected diode (NICHIA NDB4916) outputting 400 mW. The diode is injected using the rejection port on a Newport ISO-04-461-MP isolator which is capable of handling high optical powers. The NICHIA diode can output up to 600 mW, but we run it at a lower power to prolong its lifetime and protect the optical elements. When working with blue light at such powers, dirt or dust can get burned to the surface of optical elements. Fiber interfaces are especially at risk of getting burned as the beam intensity is increased by orders of magnitude when light is focused down to the size of a fiber core. If a fiber has an unusually low transmission, it might need to get polished.

The layout of the optics after the blue high power diode is shown in Fig. 3.4. The MOT AOM shifts the frequency with $+80$ MHz, such that the detuning of the MOT beams is -40 MHz relative to atomic resonance. The power in the diffracted beam is split on a PBS and coupled separately into two fibers for the XY and Z blue MOT beams. The XY fiber outputs 25 mW, and the Z fiber outputs 3 mW. The power is distributed between the X

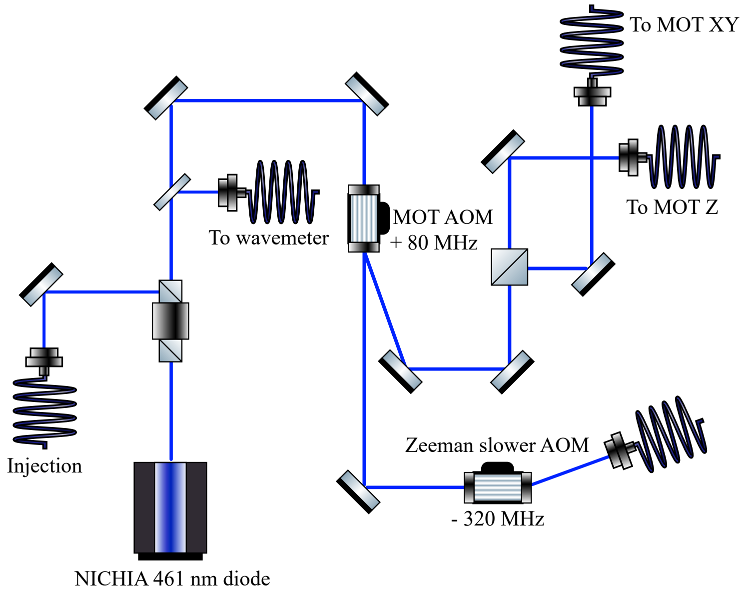

Figure 3.4: Layout of the blue MOT and Zeeman slower breadboard. A high power NICHIA diode is injected with the blue reference laser, and generates 400 mW of power for MOT beams and the Zeeman slower.

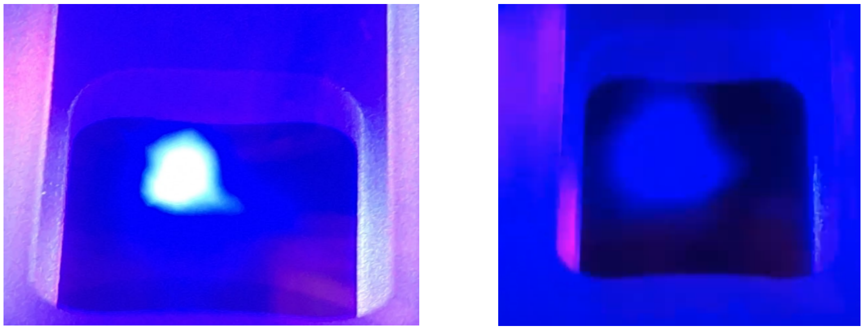
High power blue MOT

Low power blue MOT

Figure 3.5: Pictures of the high and lower power blue MOT.

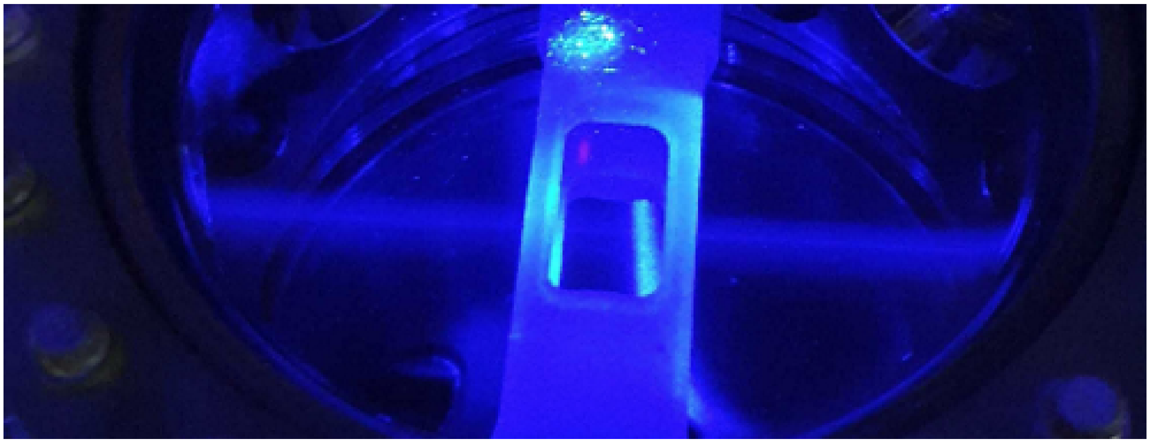

Figure 3.6: Fluorescence from the Zeeman slower beam travelling through the science chamber.

and Y MOT beams using a $\lambda/2$ waveplate and a PBS. The circular polarization of the MOT beams is generated using six achromatic $\lambda/4$ waveplates (AHWP10M-600), which works for both the 461 nm blue MOT and the 689 nm red MOT (Fig. 3.1). The blue MOT benefits substantially from a higher power in the XY beams as they remove the majority of the kinetic energy in the atomic beam - even after the Zeeman slower, the atoms move at speeds of $10 - 20$ m/s.

The light for the Zeeman slower is recycled from the 0th order of the MOT AOM. It is passed through the Zeeman slower AOM to achieve a detuning of -440 MHz from atomic resonance. Typically, we manage to couple ≈ 25 mW through the Zeeman slower fiber. For this optical power, the optimal current for the Zeeman slower coils is 9A. However, if the optical power is increased, the coil current can be increased. Figure 3.6 shows an image of the fluorescence from the Zeeman slower beam travelling through the science chamber.

The blue MOT has a secondary cooling stage where the power in the MOT beams is lowered to half of the initial power. This is done by passing the RF signal driving the MOT AOM through a mixer. The voltage on the I port on the mixer controls the strength of the signal transmission, and the control voltage for high (low) power blue MOT operation is 600 mV (300 mV). The control voltage is derived off a RIGOL frequency generator triggered by the experimental sequence. Figure 3.5 shows the two blue MOT regimes; the low power blue MOT is significantly more diffuse, but the lower temperature increases the transfer efficiency into the next narrowband red MOT stage.

3.2 689 nm systems

The wavelength of the ${}^1S_0 \rightarrow {}^3P_1$ transition is 689 nm. In our experiment, we use 689 nm light for cavity locking, the red MOT, pumping, and repumping. We have two 689 nm diodes and one tapered amplifier (TA) to generate enough power for strong population inversion pulses and a broadband red MOT. The red diodes are injected by light from a stable reference laser.

The 689 nm light on our optical table is derived from the ”slave 1” laser, which in turn is injected by our stable reference ”master” laser. Slave 1 injects the ”slave 2” diode that is used to generate light for the red MOT. Figure 3.7 shows the layout of the optics table around slave 1, where most optical elements play a role in the generation of frequencies to lock the science cavity either at atomic resonance or one FSR away. The light from slave 1 initially has a $\delta_l = +2\pi \cdot 43.3$ MHz frequency detuning to the ${}^1S_0 \rightarrow {}^3P_1$ atomic resonance, inherited from the reference laser, and it outputs ≈ 20 mW. The frequency is shifted with $-2 \cdot 345.6$ MHz in a double pass AOM (FSR AOM 1), after which it is incident on another PBS that guides the light one of two ways, depending on the input polarization. If we wish to lock the cavity one FSR away from resonance (the common configuration for all experiments described in this thesis), the polarization is unchanged, and we move a flip mirror to reflect the light after it has been frequency shifted an additional -133 MHz by AOM 2. The polarization of the light gets cleaned in a Glan-Taylor (GT) polarizer before coupling into a fiber EOM. The fiber EOM is utilized to generate frequency sidebands for locking the science cavity, but it can simultaneously be used to generate sidebands at one FSR - the application of which we will discuss later.

If we instead wish to lock the cavity with resonant light (the previous configuration for running NICE-OHMS experiments not described in this thesis [41, 90, 91]), we flip the linear polarization after the light exits the FSR AOM 1 double pass configuration. The flip mirror is removed from the beam path, such that the light now enters a second AOM double pass configuration, AOM 3. Here, the frequency is shifted by $+2 \cdot 324$ MHz, bringing it back to resonance.

3.2.1 Reference laser and beat generation

Our 689 nm reference laser is stabilized to a high-finesse (≈ 150000) cavity in an acoustic isolation chamber. The stable laser and cavity setup is situated in a quiet room next to our laboratory. The reference light propagates through a long fiber between the labs to inject

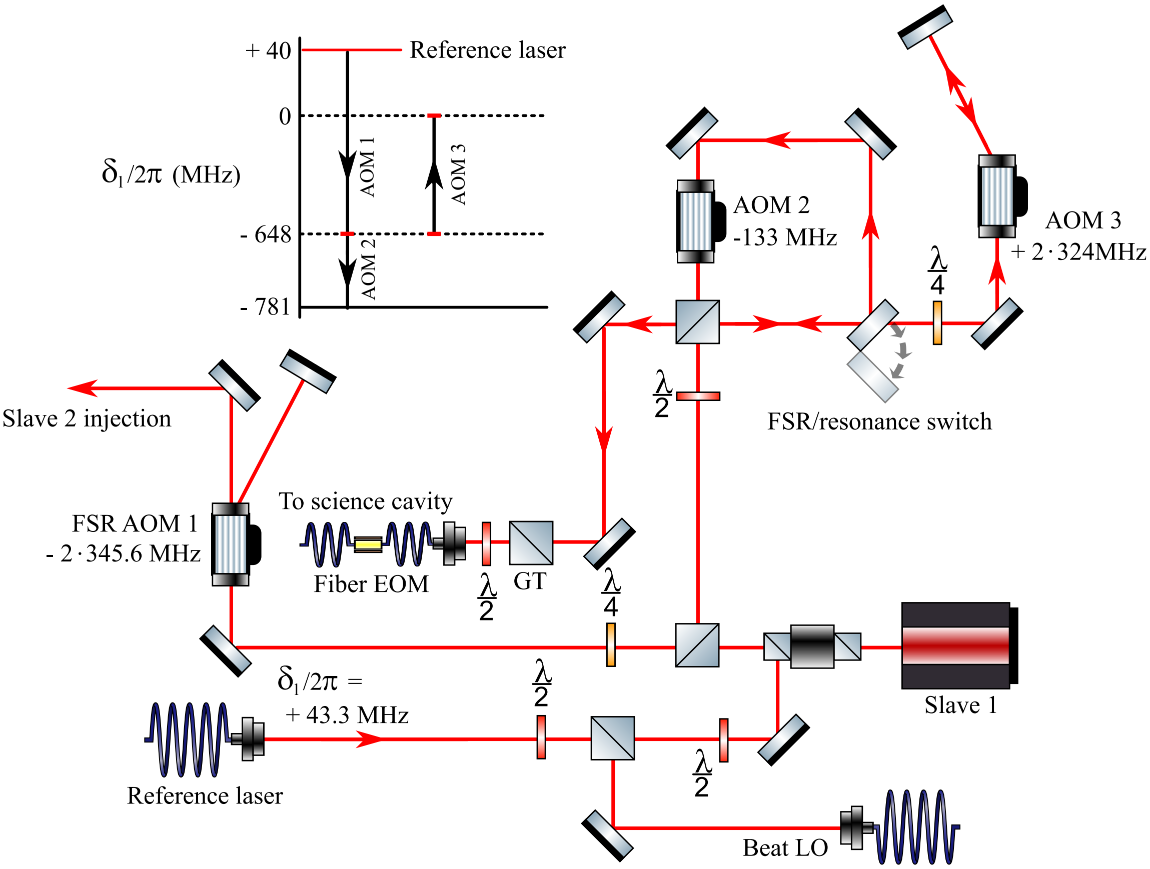

Figure 3.7: Optics and components for shifting the science cavity lock point between locking on atomic resonance and locking one FSR away.

our 689 nm diodes and perform beat experiments on the superradiant light generated by our atom cavity system. For injecting the first 689 nm diode, we typically use 1.1 mW right before the laser diode. For beat experiments, we overlap the science cavity output light with ≈ 100 µW of reference laser light.

To quantify the frequency stability of our superradiant pulses it is important to have a stable frequency reference. We have investigated the frequency stability of the reference laser by computing an Allan deviation against another cavity stabilized 689 nm laser. The overlapping Allan deviation at 1 ms shows a stability of 300 Hz, ultimately reaching 20 Hz at 400 ms before drifting. We believe this stability is limited by the secondary laser, and not the reference laser, because the ultimate stability is sensitive to tweaking the locking parameters of the secondary laser.

The beat between the superradiant light and the reference is also useful for removing low frequency noise in the cavity output. Particularly, the beat signal filters out the cavity locking light background. Besides frequency stability measurements of our long superradiant pulses, we use the beat between the cavity output and our reference to measure superradiant pulse amplitudes and to gauge the normal mode splitting.

3.2.2 Science cavity

The science cavity is the heart of the experiment. The cavity is housed in an in-vacuum ZERODUR spacer resting in two DN40CF openings on an axis perpendicular to the atomic beam (Fig. 3.8). The science cavity has a length of 192 mm [61], inferred from the measured free spectral range (FSR) of 781.14 MHz. The cavity has a finesse of ≈ 1000 from the measured linewidth of $\kappa/2\pi \approx 800$ kHz. The linewidth used to be $\kappa/2\pi \approx 620$ kHz [83], but it is likely that the finesse has dropped over the years due to degradation of the mirrors. The cavity mirrors are 1 inch in diameter and have a radius of curvature (ROC) of 9 m. The waist radius of the cavity is $w_0 = 450$ µm, which results in a relatively low single atom cooperativity of $C_0 = 5.72\text{e-}4$ and atom-cavity coupling $g_0/2\pi = 813.5$ Hz [61]. The large waist, however, allows us to fit most of the red MOT atoms to achieve a large collective cooperativity, $C_N = NC_0$. Moreover, having a low single atom cooperativity is desirable when designing a narrow linewidth superradiant laser [49].

The science cavity is locked using Pound-Drever Hall (PDH) [95], using sidebands generated with the fiber EOM depicted in 3.7. The PDH method is a phase-modulation spectroscopy method used to stabilize the frequency of a laser to the resonance of an optical cavity

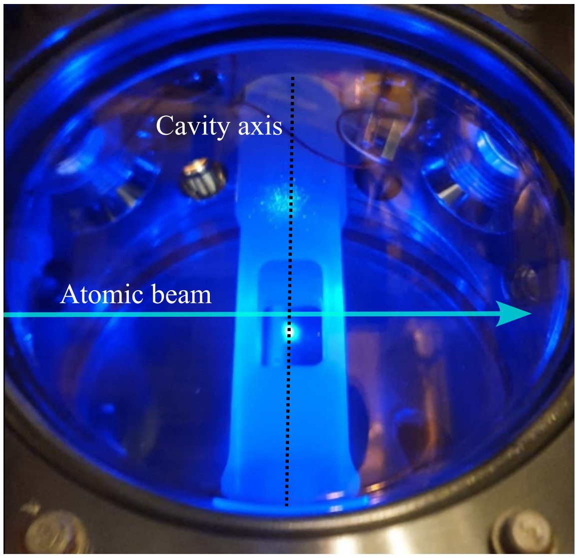

Figure 3.8: The science cavity ZERODUR spacer. The spacer has openings to allow optical access to the center of the cavity. The blue MOT is visible.

or vice versa [78]. The PDH signal is generated by demodulating frequency modulated light reflected off an optical cavity. An electro-optic modulator (EOM) is employed to perform phase modulation on the optical carrier frequency incident on the cavity, resulting in the generation of sidebands at frequencies $\omega_l \pm \omega_m$. These sidebands are produced with an initial phase difference of π, leading to destructive interference between the two beat nodes oscillating at ω_m. When one of the spectral triplet components is close to cavity resonance, the phase shift of the reflected light changes, and the destructive interference between the two beat notes at ω_m will be disrupted. Measuring the strength of the ω_m beat node by demodulating the reflected light yields an anti symmetric errorsignal around cavity resonance, which constitutes a useful metric for determining the laser detuning to the cavity.

3.2.3 Red MOT

To move into the bad cavity regime, the homogenous broadening of the ensemble must be less than the cavity linewidth. For the blue MOT, we have temperatures of around $\approx 3-5$ mK, which corresponds to a Doppler width $\gamma_{\text{Dopp}}/2\pi \approx 1$ MHz, larger than the cavity linewidth of $\kappa/2\pi = 800$ kHz. We implement another cooling stage to the experiment bring the temperature of the atoms to µK levels. In this regime the typical Doppler broadening is on the order of 10s of kHz, which is much smaller than the cavity linewidth. The red MOT cloud typically is much smaller and with a much higher density than the blue MOT [96], which allows more atoms to interact strongly with the cavity mode.

Out of the blue MOT, the atoms have RMS velocities ≈ 1 m/s. The much narrower linewidth of the 689 nm transition (7.5 kHz) versus 30.5 MHz for the 461 nm blue MOT allows for cooling to much lower temperatures, but results in a much weaker trapping force of the MOT [97]. The magnetic field gradient of 35 G/cm used for the blue MOT is too high for red MOT operation, and it is common to ramp the magnetic field gradient to $3 - 5$ G/cm to reach a higher transfer efficiency between the blue and red MOT. However, this must be done on a timescale comparable to the time it takes the atoms to leave the red MOT beams, which is a few ms. The specifics of how this fast ramping is achieved is discussed in chapter 3.5.2.

In the red MOT, we use three pairs of retro reflected 1 cm diameter MOT beams, each with an initial 3 mW of 689 nm power. In the first step of the red MOT, we broaden the frequency of the 689 nm MOT beams to increase the capture range. This is what we refer to as the broadband (BB) red MOT. We sweep the modulation frequency of the AOM with 3 MHz at a 50 kHz repetition frequency. The BB MOT dramatically increases the capture efficiency, and we have seen a transfer efficiency between the blue and red MOT of close to 100% [1]. However, this also largely depends on the final temperature of the blue MOT, and as such the overall atom number in the red MOT is the important figure of merit. The BB red MOT in our experiment has atoms enough to observe the scattered light with the naked eye (or a smartphone camera, as shown in Fig. 3.9). This is remarkable as the scattering rate for the red MOT transition is ≈ 4300 times lower than the blue MOT transition. When the experiment is aligned and all powers are optimized, we have seen up to 120 million atoms in the BB red MOT cooled down to 10-20 µK.

The beam path for the 689 nm red MOT starts with an injected diode laser "slave 2" (Fig. 3.10). Like slave 1, it is injected at a detuning $\delta_l/2\pi = +40$ MHz to ${}^1S_0 \rightarrow {}^3P_1$ resonance. The laser outputs 20 mW and ≈ 13 mW is coupled to a fiber that injects a tapered amplifier (TA). The TA is a Toptica BOOSTA with a maximum ouput power of 200 mW. With 13 mW of injection power, we reach typical power levels of $170 - 200$ mW. The TA output beam is guided towards the pump AOM which we use for producing short (typically 500-800

---

[1] The transition between the blue and red MOT is captured in this GIF: `https://photos.app.goo.gl/75AiokbfTHExv1Qh8`

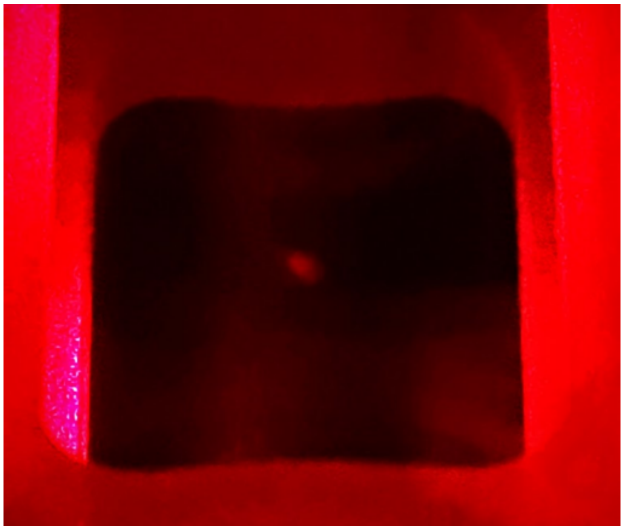

Figure 3.9: Picture of a BB red MOT with $N = 120e6$ atoms.

ns) population inversion or Ramsey pulses. This light is shifted to resonance and fiber coupled. Typically, we achieve 15-20 mW through this fiber, which is limited by quality of the beam shape after the TA. The first and zero order of the pump AOM passes through a mechanical shutter (SRS475) controlled by an SRS474 shutter driver. These shutters have a typical closing time of just a few hundred nanoseconds with very limited vibrations. The shutter is used to completely turn off all sources of 689 nm light to the atoms, and it is a useful tool for aligning AOMs in CW operation. The beam then passes through the MOT switch AOM, where the frequency is shifted +80 MHz. We use this AOM to turn on and off the red MOT beams when the shutter is open. To generate the frequency for the MOT beams, we shift the frequency with ≈ -123.3 MHz (depending on the desired detuning). We change the driving frequencies for an AOM (BB/SF MOT AOM) to switch from a broadband to a single frequency (SF) red MOT, which cools the atoms further. For this purpose we use a switch (ZASWA-2-50DR) in reverse, using the two outputs as inputs. We generate the driving frequencies on the two output channels of an AWG (Rigol DG4162). We transmit the red MOT AOM frequency through a mixer and use the I port to regulate the strength of the RF signal. This is useful for ramping the power of the red MOT beams for a secondary lower power SF red MOT stage, with which we can achieve a final atom cloud temperature of just a few µK.

Finally, the red MOT light is coupled into the XYZ fiber. Typically, we achieve $\approx 14 - 16$

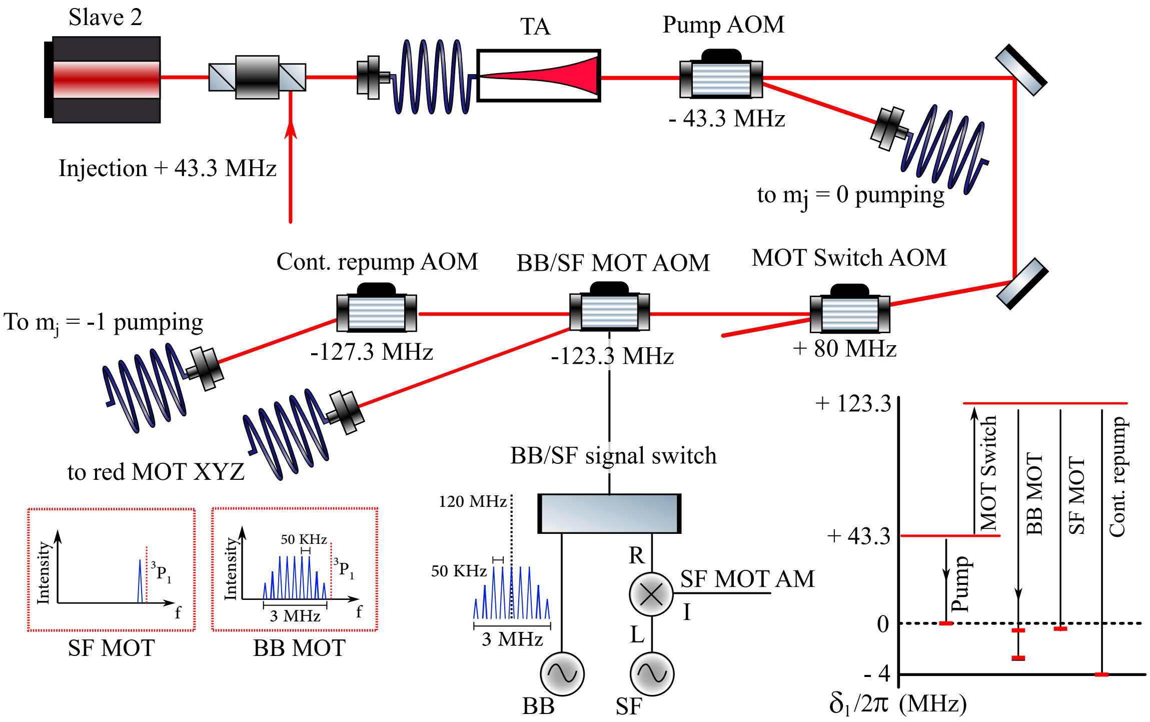

Figure 3.10: Optics and AOMs for 689 nm MOT beams.

λ	Power (out of fiber)	Transition	Application
707 nm	4 mW	$^3P_2 \rightarrow {}^3S_1$	blue MOT & continuous lasing
679 nm	8 mW	$^3P_0 \rightarrow {}^3S_1$	blue MOT & continuous lasing
688 nm	≈ 2 mW	$^3P_1 \rightarrow {}^3S_1$	continuous lasing
689 nm	< 1 mW	$^1S_0 \rightarrow {}^3P_1, m_j = \pm 1$	continuous lasing
689 nm	$15 - 20$ mW	$^1S_0 \rightarrow {}^3P_1, m_j = 0$	population inversion

Table 3.1: Pumping lasers and their functions in the experiment.

mW through this fiber. This light is split into two paths using a PBS. The transmission through the PBS is a free space path to the produce the Z MOT beam. The red MOT Z beam is overlapped with the blue MOT beam on a dichroic mirror, before passing through an achromatic $\lambda/4$ wave plate. The reflection of the PBS is fiber coupled into the red MOT XY fiber, the output of which is (similar to the Z beam) overlapped with the blue MOT beams on a dichroic waveplate before passing through an achromatic $\lambda/4$ wave plate.

3.3 Pumping lasers

Besides the 461 nm and 689 nm light directly applied for MOT operation, we use several different repumping transitions in the experiment. For blue MOT operation, the 679 nm and 707 nm repumpers bring atoms from $^3P_0, 2$ to $^3S_1$. From here, the atoms can decay into $^3P_1$ and subsequently $^1S_1$ to reenter the blue MOT cycle. The 679 nm and 707 nm repumpers are Toptica DL PRO laser heads controlled by the same DLC pro laser controller. The diode in the 679 laser head is a LD-0695-0040-AR-1 with a maximum power of 45 mW. The 707 nm repumper diode is a LD-0685-0050-AR-1 with a maximum power of 25 mW at 707 nm. The repumpers are overlapped on a non-polarizing beamsplitter and coupled to the same fiber (Fig. 3.11). The atoms are repumped through the Zeeman slower window at an angle perpendicular to the cavity axis. Note that the 679 nm and 707 nm repumpers stay on during the entire experimental cycle.

To address the $^3P_1 \rightarrow {}^3S_1$ transition we employ a 688 nm repumper. The 688 nm laser is a Toptica DL PRO laser head using an LD-0685-0050-AR-1 diode. This repumper works in tandem with the 689 nm repumper to excite atoms $^{1S_0} \rightarrow {}^3S_1$ through $^3P_1, m_j = \pm 1$, the goal of which is to populate the $^3P_1, m_j = 0$ excited lasing state with atoms decaying from $^3S_1$. We derive the 689 nm repumper from the zero order in one of the the red MOT AOMs. Both the 688 nm and 689 nm repumper is sent through an AOM for fast shuttering.

We shall go more in depth with the application of the 688 nm and 689 nm repumpers later when we discuss continuously repumped pulses.

A fraction of the 679 nm, 688 nm and 707 nm light is picked off for frequency locking. The locking arm of the 707 nm repumper setup is double passed through an AOM to allow for tuning the frequency offset of lock. The locking light for all aforementioned repumping wavelengths is overlapped on a non-polarizing beamsplitter and transported via a fiber to the transfer cavity breadboard used for frequency stabilization. Here, the repumpers are passing through a free space EOM to generate sidebands for PDH. The repumpers are coupled to the transfer cavity, and upon reflection the wavelengths are split up with color filters. A PDH signal is generated for each repumper which is used to stability the frequency to the transfer cavity length. Currently, the setup does not allow for locking all repumpers simultaneously - another filter separating the 679 nm and 688 repumpers is needed. However, the stability of the 679 nm is such that we usually only have to tuned the frequency once a day to completely saturate the repumping transition. Locking just the 688 nm and 707 nm repumpers allows for stable continuously repumped pulses.

The transfer cavity is stabilized using the reference light. The purpose of this cavity is to transfer the stability of the 689 nm reference laser to the repumper, hence the name. The 689 nm reference light passes through an EOM to generate a PDH signal to stabilize the cavity length. Both EOMs on the breadboard are resonant with a built in tank circuit, and can be driven with much lower voltages than usually required for achieving usable modulation depths. It suffices to drive them directly with the output of a RIGOL frequency generator (of output 10 dBm).

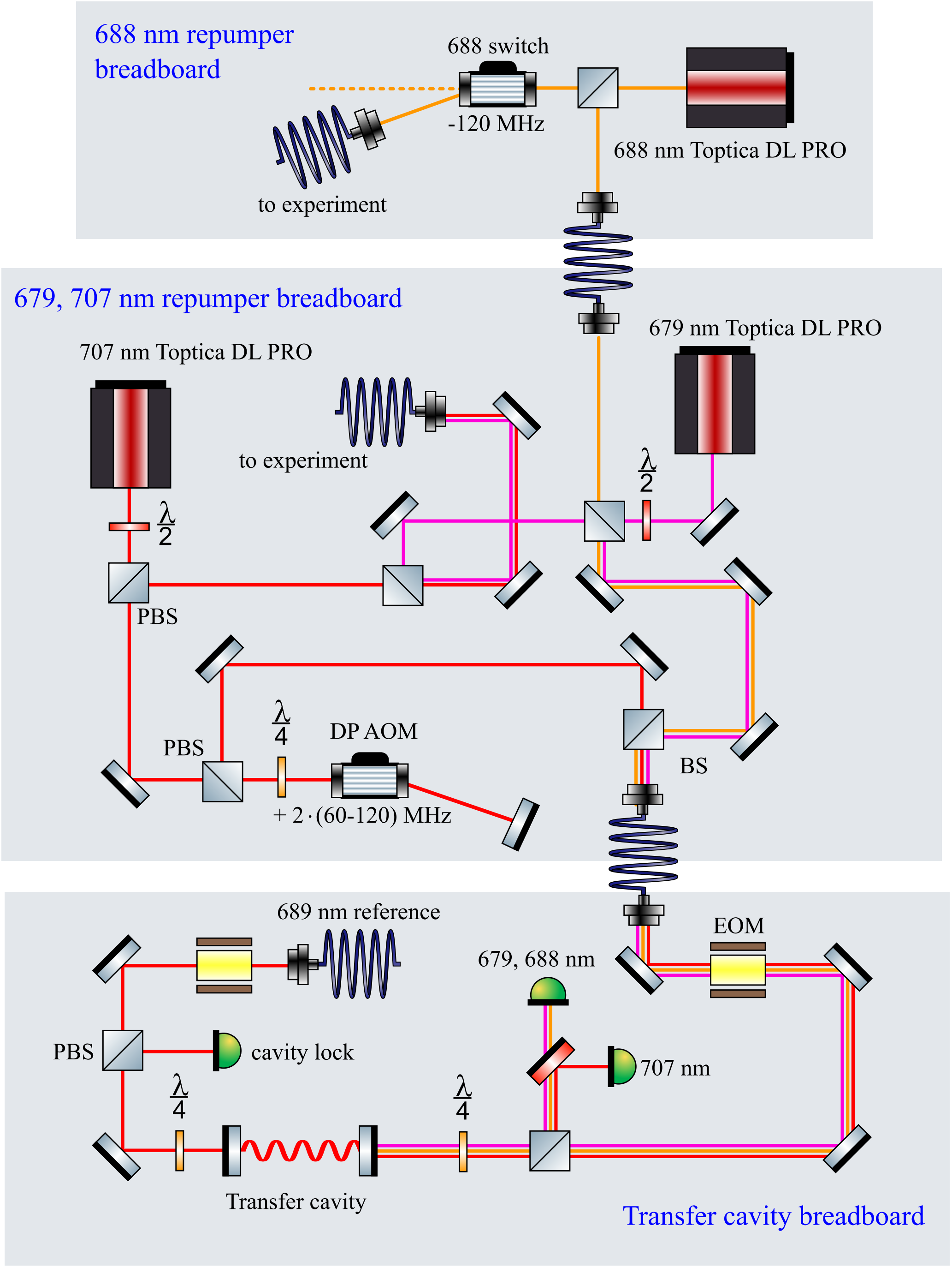

Figure 3.11: Layout of the breadboards housing the 679, 688 and 707 nm repumpers. The repumpers are locked to the transfer cavity using Pound-Drever-Hall, and the transfer cavity is in turn locked to the 689 nm reference laser.

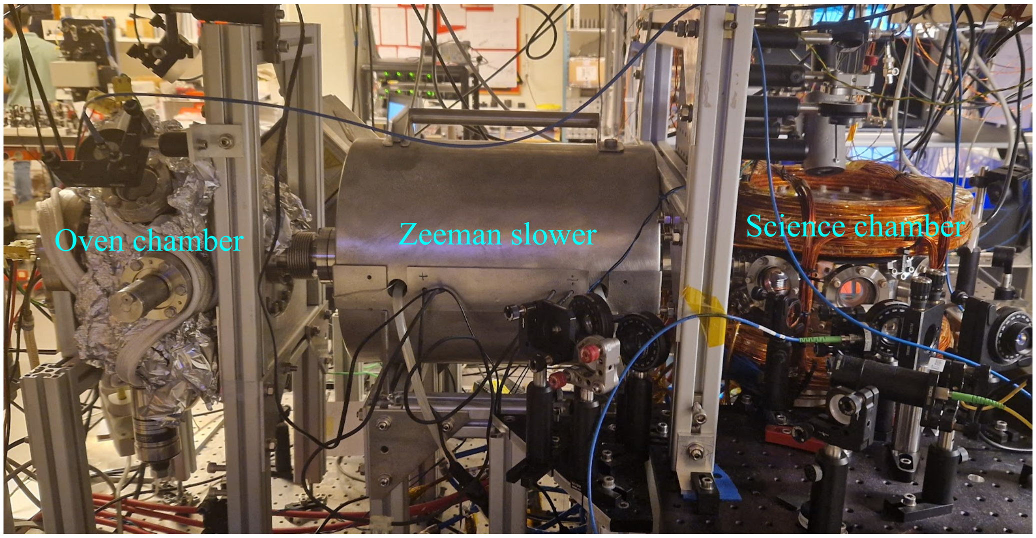

Figure 3.12: Vacuum system consisting of three main parts; the oven chamber, the Zeeman slower tube, and the science chamber.

3.4 Vacuum systems and strontium oven

The vacuum system consists of three main parts; the oven chamber, the Zeeman slower tube, and the science chamber. The Zeeman slower and the science chamber did not get exchanged or upgraded during the course of my PhD.

The science chamber is large circular chamber from Kimball Physics (MCF800-ExtOct-G2C8A16). The chamber has 8 DN40CF ports symmetric around the center, 2 DN166CF ports on the top and bottom, and an additional 16 DN16CF ports. Windows are mounted on all DN40CF ports except for one port connecting the Zeeman slower tube to the science chamber. The large opening diameter of these windows (41.3 mm) is useful for transmitting large diameter MOT beams to catch atoms. The science cavity spacer in our experiment is resting on Viton rings inside two opposing DN40CF openings on an axis perpendicular to the atom beam (center of the drawing on Fig. 3.1). The chamber is mounted on top of a tee piece chamber where an ion pump is mounted.

The Zeeman slower tube connects the oven chamber to science chamber. A solenoid coil is wrapped around the tube to form spatially varying magnetic field as atoms from the oven chamber travels towards the science chamber. The atoms interact with a counter propagating cooling laser slowing them significantly. The Zeeman slower vacuum tube has a small opening that creates a differential pump between the two chambers, which is useful

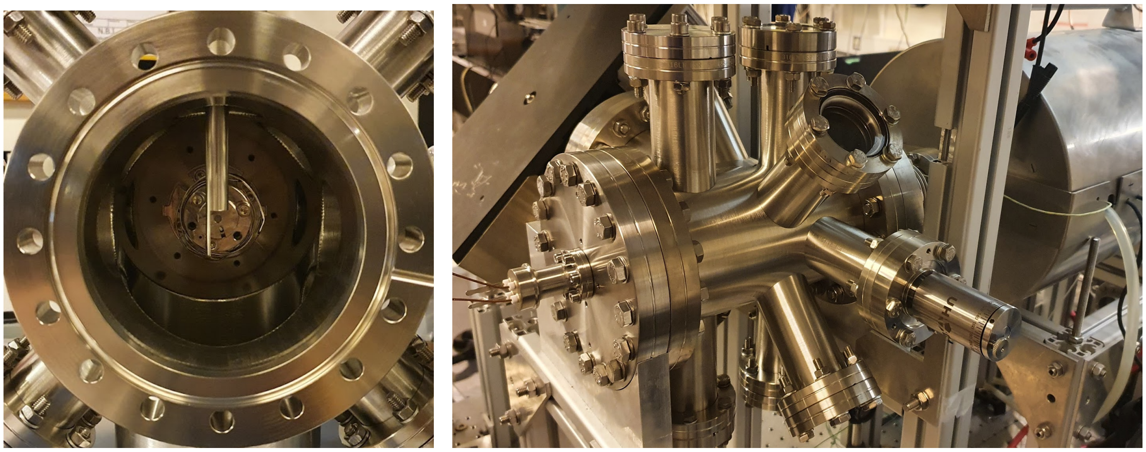

(a) A view into the oven chamber. **(b)** The oven chamber mounted on the Zeeman slower.

Figure 3.13: Oven chamber with strontium oven mounted. The oven has not yet the heat shields attached.

to keep the pressure low in the science chamber even when the oven is heated up. The Zeeman slower tube is long enough to efficiently slow down atoms from several hundreds of m/s to just tens of m/s. At such velocities they can be loaded into a 461 nm MOT (as we discussed in chapter 2). The spatially varying Zeeman shift is generated with a spin-flip solenoid geometry where the magnetic field varies linearly, but crosses zero halfway through the slower length. The has the advantage that the Zeeman slower can be run at a much lower current, and cooling of the coil and vacuum chamber is not necessary.

The oven chamber was upgraded as a part of a large experimental overhaul, that saw the MOT coils and the strontium oven completely redesigned. Due to a broken knife edge on the oven flange on the old oven chamber, the time was right for an upgrade.

The current oven chamber is a custom cylindrical chamber built by Kurt Lesker. The main body is a DN100CF tee in 316LN stainless steel, with an opening diameter of 101.6 mm suitable for fitting in an oven. The chamber is connected to the Zeeman slower tube using a DN100CF to DN16CF converter (right hand side of Fig. 3.13b). The oven is mounted on the DN100CF flange on the opposing side (Fig. 3.13a). The flange has a DN16CF adapter to mount a feedthrough for current carrying wire and a Type K thermocoupler, to heat the oven body and measure the temperature. Type K thermocouplers are well suited for measuring the temperature of strontium ovens, as they can handle up to 1100 °C[2] and

---

[2] https://www.thermocoupleinfo.com/type-k-thermocouple.htm

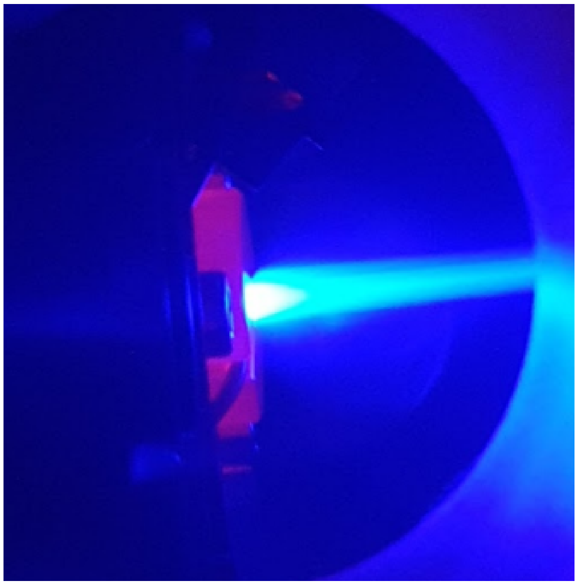

Figure 3.14: Fluorescence at the oven nozzle from the Zeeman slower beam. The oven lid operating at ≈ 560°C glows red due to black body radiation.

we typically run the oven at around 530 °C. Perpendicular to the oven flange, another DN100CF flange has an ion pump connected.

The chamber has 9 DN40CF flanges mounted, all pointed towards the center line of the oven chamber. One of these, closest to the oven flange, has another feedthrough to carry current and measure the temperature of the oven lid. Another flange sits opposite to this and houses a valve for connecting a turbopump. Four DN40CF flanges around the oven nozzle are mounted with windows to allow for optical molasses. As of yet, we have had no need to implement the optical molasses as our atom number is high and (usually) consistent. One flange has a rotary feedthrough mounted; a manually actuated MD40N MagiDrive also made by Kurt Lesker. The rotary feedthrough is mounted with a hockey stick type steel shutter, such that we can turn off the atom beam through the Zeeman slower. This is to limit the strontium coating of the windows in the science chamber when we are not immediately using the experiment. Two more DN40CF ports are mounted with windows, and these are intended for either monitoring the atomic flux or for producing a laser locking signal using saturation spectroscopy.

3.4.1 Strontium oven design

Strontium exists as a solid metal at room temperature and must be heated to produce strontium vapor [98]. The strontium vapor is subsequently cooled and captured into a dense sample of atoms.

The basic concept of our oven design is an in-vacuum hollowed out steel cylinder filled with strontium (the oven body). The cylinder is wrapped in heating wire and has a lid with a nozzle. When the reservoir of solid strontium in the cylinder is heated, it starts to sublimate at around 400 degrees °C and a warm strontium gas will spray out through the oven nozzle. A picture of the oven at operating temperature is shown in Fig. 3.14. The blue fluorescence is from the Zeeman slower beam passing through the Zeeman slower tube and hitting the nozzle of the oven. The lid is glowing red due to visible black body radiation [3].

The heating wire is wrapped around the oven body in a helix pattern and has a dual core such that it only needs an electric connection on one end. This prevents the formation of a magnetic field inside and outside the oven. The heating wire has a resistance of 28 Ω, and we run it at 21.74 V. This heats the oven to a steady-state temperature of 525°C, which is reached in $1-2$ hours after turning it on. The operating temperature can be reached much faster if the oven heater is overclocked by increasing the voltage to 35 V for ≈ 20 minutes when turning on the oven. Importantly (especially for future students), we have enacted an experimental protocol for overclocking the oven voltages; the oven temperature must be constantly monitored while it is climbing towards operating temperature. The temperature of the oven rises fast, and the steady state temperature for such voltages is $700-800$°C, which is more than the somewhat fickle electronic connections in the oven can (presumably) handle.

The oven has three external sets of heat shields to reflect the black body radiation. The outer set of heat shields are mounted on the flange. The inner two are mounted on the base plate on which the oven itself is mounted on four steel spacer legs. These heat shields significantly reduce the black body heating of the surrounding oven chamber walls to a level where no external cooling is necessary. Moreover, all physical contact points between the oven, oven base plate, and the flange are thermally isolated with ceramic spacers around the bolts. Figure 3.15a shows the graphical rendition of the oven components in Autodesk Inventor. The fully assembled oven mounted on the oven flange is shown in Fig. 3.15b.

---

[3] The black body emission can be used to gauge the temperature of the lid with reasonable accuracy - though this is not necessary when we have thermocouplers in both the oven body and oven lid.

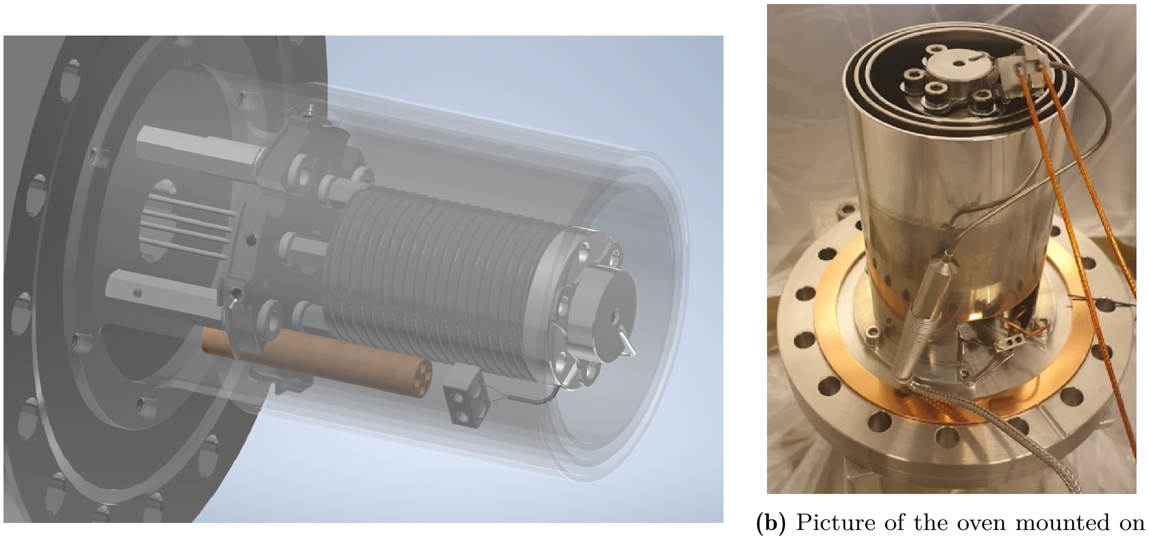

(a) Visualization of the oven mounted on the oven flange. The three layers of heat shields are transparent for a better view of the oven mounting base plate and the oven itself.

(b) Picture of the oven mounted on the oven flange with visible electrical connections, just prior to inserting it into the oven chamber.

Figure 3.15: Visualization and picture of the mounted oven.

The lid is heated to a higher temperature than the oven body to prevent strontium from building up around the nozzle. The dual core heating wire with $R \approx 13\Omega$ is wrapped around the nozzle that houses micro capillary tubes (Fig. 3.16). The lid has a cap on nozzle to hold the heating wire in place and create a circular opening for the triangular array of micro capillary tubes. We run the oven lid at 18 V, and upon turning on the oven and lid, the lid quickly reaches a temperature that is 200°C higher than the oven body because of its significantly smaller thermal mass. Over time, this difference becomes smaller, and the steady state temperature for the lid is ≈ 560°C (when the oven body is heated to ≈ 525°C.

The micro capillary tubes are 8 mm long, has an outer diameter of 300 µm and an inner opening diameter of 150 µm. Figure 3.17 shows the assembly of the oven nozzle, where ≈ 200 micro capillary tubes are placed between three steel plates forming a triangle. A screw pushes on the outside of one of the steel plates forming the triangle, and it can be tightened to force the micro capillary tubes into a stable honeycomb structure. The triangular geometry for the micro capillary array is preferable over a circular geometry, as the latter offers more stability to make the individual tubes stay aligned. The oven nozzle with micro capillary tubes significantly lowers the transverse spread of the atomic beam [99] after exiting the oven. The atoms that have a velocity closer to axis of the oven orientation

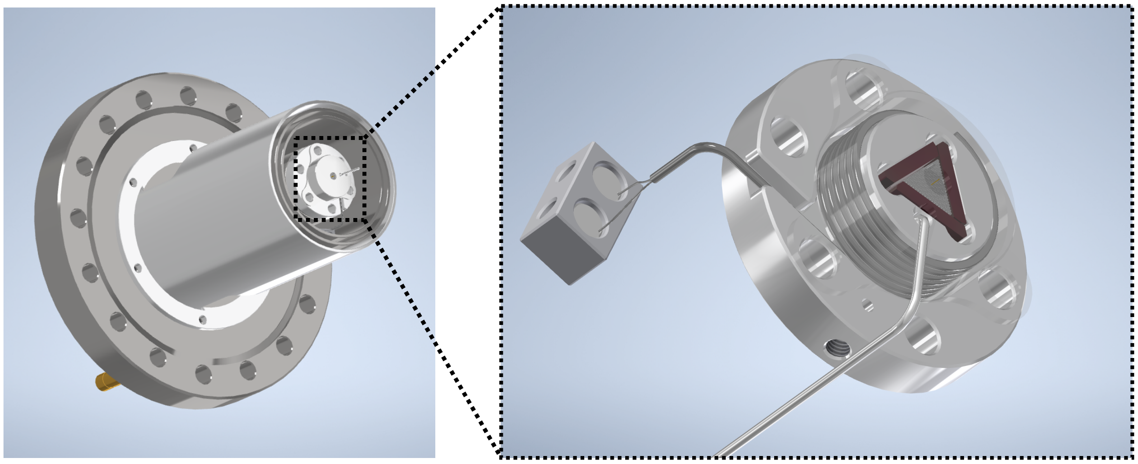

Figure 3.16: Visualization of the oven lid.

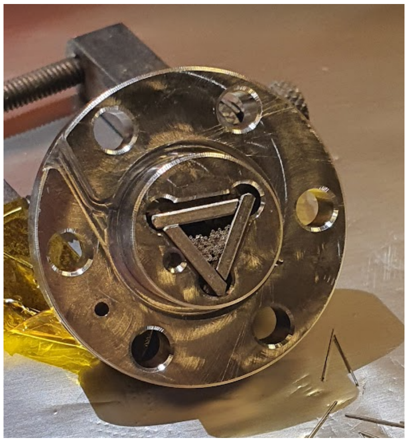

Figure 3.17: Filling the oven lid with micro capillary tubes. The triangular arrangement of steel plates can be tightened to push the tubes into a stable honey comb structure.

have a greater chance of making it through the tubes, as atoms hitting the inner sides of the micro capillary tubes are more likely to be reflected back into the oven. This limits the coating of the windows close to the oven, and increases the relative amount of usable atoms leaving the oven. The oven can operate longer without having to replace the strontium, as less strontium is wasted on velocity classes that we cannot cool and trap.

We measure the relative atomic flux by probing the atomic beam close to the oven nozzle with a weak 461 nm probe. The absorption from the oven nozzle as a function of temperature and laser detuning is plotted in Fig. 3.18. As the temperature of the oven body is increased, the optical depth of atomic beam rises sharply. The line shape of the absorption possesses an interesting kink at the maximum OD also observed in [99], which is most likely the consequence of the velocity selection imposed by the micro capillary tubes.

We can increase the flux of atoms from the oven by increasing the steady state temperature of the oven body further, but this would limit the time we could operate the oven without depleting the strontium. The oven is loaded with ≈ 1 mg of metallic strontium flakes. The oven has room for more, but the oven is only halfway filled to prevent the strontium from blocking the nozzle of the oven when the oven is mounted horizontally into the oven chamber. So far, we have operated the oven for thousands of hours since we loaded the oven with strontium 3 years ago.

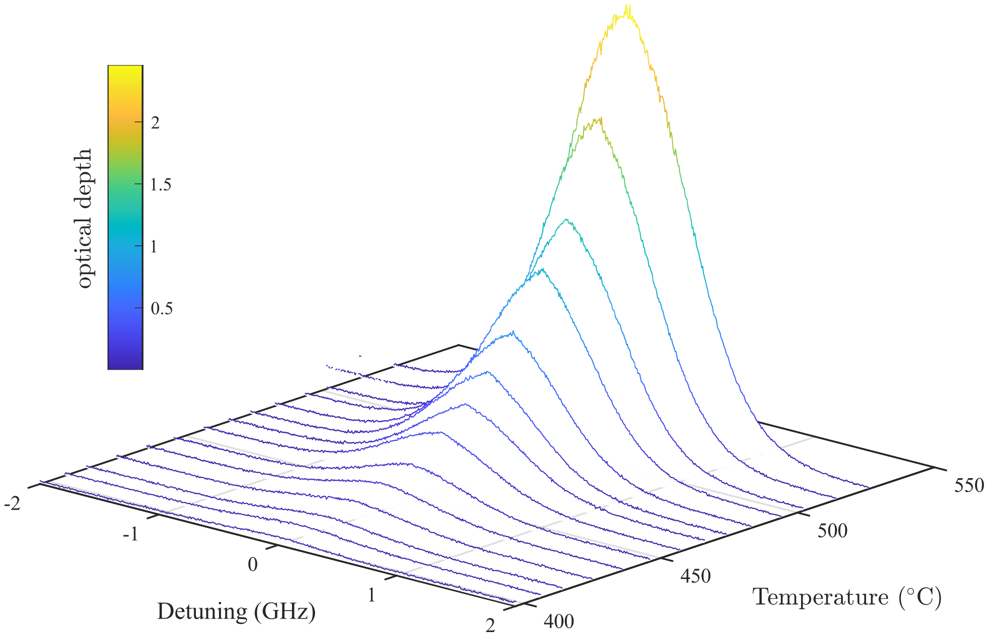

Figure 3.18: Oven absorption in optical depth as a function of temperature.

3.5 Magnetic fields

In the trapping and cooling of atoms, magnetic fields are essential. The MOT fields plays a role in forming an anti symmetric restoring force towards a single point where atoms will get trapped and cooled. After preparing the sample of atoms, the MOT fields are turned off, and the bias fields remains. These are tuned to center the MOT inside the cavity, and to provide a bias field to address the atoms with the right polarization for pumping and repumping.

3.5.1 MOT coils

A major challenge when transferring atoms between a 461 nm and 689 nm MOT is that each MOT works best with different magnetic field gradients. The 461 nm MOT usually requires a gradient of 20-40 G/cm, whereas the red MOT operates most efficiently with just 2-5 G/cm, due to a much longer lifetime of the $^3P_1$ state. This means that we have to change the magnetic field on the same timescale as the atoms leave the 689 nm MOT beam intensity profile after turning of the 461 nm beams. For atoms cooled to 2-5 mK, which is the usual end temperature of the 461 nm MOT, this timescale is just a few ms. Due to our chamber geometry, where the magnetic coils are separated by 21 cm, we need strong magnetic fields to generate a sufficiently high gradient for the 461 nm MOT. This requires high current and many coil windings, where the latter leads to an increased inductance of the circuit.

Shuttering the magnetic field in just a few ms is a technically difficult challenge as it can generate very high voltage drops and generate eddy currents in the surrounding components. Particularly, the previous generation of the experiment used MOT coils which were wound around a circular solid copper holder that has embedded cooling tubes. The strong coupling between the wires and the copper wire resulted in Eddy currents that could last as long as 10-20 ms upon turning off the magnetic field. To lower this characteristic timescale of changes in the magnetic field, the most important first step was to change the MOT coil holders to limit the eddy currents. In collaboration with the mechanical workshop at NBI, we devised a design for MOT coils where the coils were wound around a circular aluminium holder with a gap (Fig. 3.19a). In this design, the wires are wound around each coil holder in two parallel grooves separated by a fin of aluminium which has the function of increasing the thermal contact between the coil holder and the wires. Cooling canals are drilled into the top and bottom of each holder, sealed with a lid that is glued on using epoxy. With this design, we can adjust the magnetic field gradient from blue MOT to red MOT compatible in a just a few ms. However, this design had some decisive flaws which eventually forced us to adopt another solution for MOT coils. Namely, the epoxy holding the lids on the cooling canal eventually gives in to the constant pressure of the cooling water. Figure 3.19b shows a photo of the MOT coils after one of our many fixes with epoxy. We have added 6 clamps to both MOT coils to prevent the lid from bending and causing leaks. Even more fatal to the experiment, ramping the magnetic field fast produces a force on the individual wires. On a timescale of months, the wiggling of the wires scratches of their thin coating which results in short circuits.

The MOT coil problems was the casus belli [4] for a chain of upgrades to the vacuum systems; to change the MOT coils, we had to break the vacuum in the science chamber due to topology. Breaking the vacuum means that we had to change the strontium in the oven as it would oxidize. Since the knife edge on the oven flange was damaged, it was unlikely that the seal would be suitable for UHV applications again after the flange had been opened - and so we designed a new and improved oven chamber.

---

[4] *noun; an act or situation that provokes or justifies a war.*

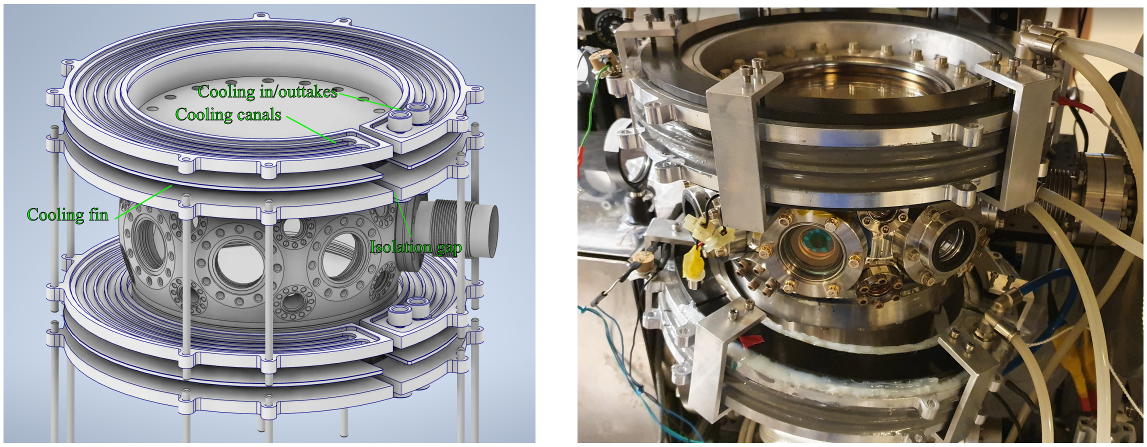

(a) First iteration of MOT coils for red MOT generation.

(b) MOT coils in place on the chamber. Clamps are applying pressure on the cooling canal lids to prevent leaks.

Figure 3.19: Previous iteration of MOT coils.

The new set of MOT coils that we designed was intended to be cheaper, simpler and easy to wind by hand. Inspired by the MOT coil design in [47], we wound new coils out of hollow copper wire (Fig. 3.20). The outer diameter of these wires is 5 mm, and the inner diameter where cooling water flows is 3 mm. To limit the fluid pressure drop, we sectioned each MOT coil into three parallel cooling circuits that are electrically in series. Each has 27 windings, adding up to a total of 81 windings. Our previous experience with enameled wire led us to meticulously cover the hollow copper wire with Kapton tape to ensure electronical isolation even under the stress that the forces of the rapidly changing magnetic field would induce on the wires. The cooling efficiency is surprisingly good, as the cooling water flows directly in the copper wire, rather than relying on good thermal contact between several layers of wire held together by epoxy (as in our previous design). We run the cooling water at 16°C at a pressure of just 1.5 bars, regulated by pressure valves just before entering each of the three parallel sections of the MOT coils. This is sufficient to keep the temperature of each MOT coils at around 25 °C even when operating at 75 A.

3.5.2 Control of MOT fields

We run the blue MOT at ≈ 75 A for both MOT coils. The red MOT runs at a much lower current at around $3-4$ A. As mentioned before, we want to ramp the magnetic fields between

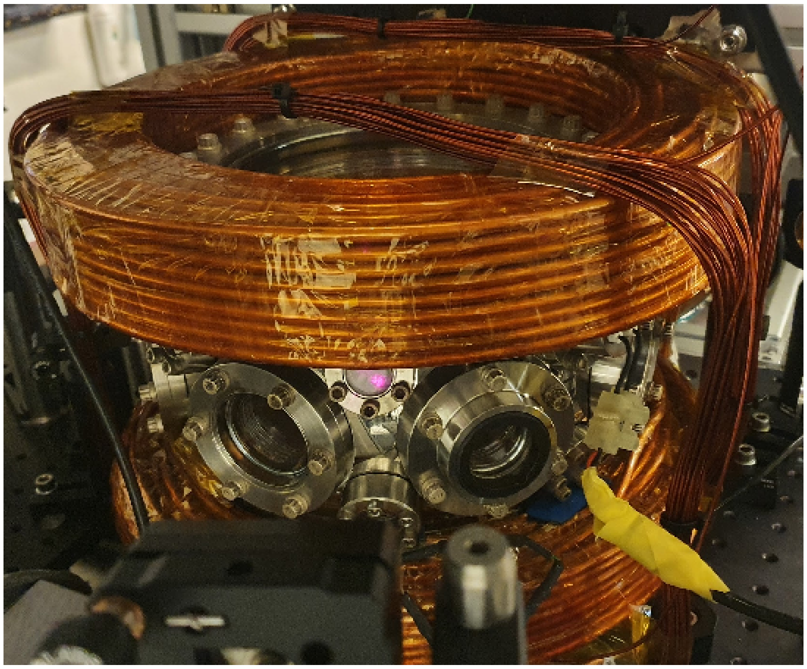

Figure 3.20: The new hollow core MOT coils in place on the science chamber.

the two MOT regimes in just a few ms. This requires dissipating a significant amount of current in this period of time. To address this, we built two identical control circuits for each coil to stop the current by switching the resistance of a MOSFET (APTM50UM09FAG [5]). This scheme is depicted in Fig. 3.21. The MOT coil is wired in parallel with a diode and a 10 Ω resistor. When the MOSFET resistance increases, the current running in the MOT coil will be dissipated through the resistor. If the MOT coil is shut off too quickly, the voltage over the MOSFET can reach thousands of volts, and the max rated voltage over the MOSFET is 500 V. To ensure we operate within a safe limit, we have put several varistors in parallel with the MOSFET. The varistors open for voltages over 47 V. The current is measured using a Hall probe (ACS758LCB-100B-PFF-T). To generate an errorsignal for stabilizing the current through the circuit, the Hall probe voltage is compared to a reference voltage set for a desired magnetic field strength. The errorsignal is fed to PID controller that controls the MOSFET resistance. Varying the reference voltage provides fast and efficient control over the magnetic field values throughout the experimental cycle.

Figure 3.22 shows the magnetic field decay times of the old and new MOT coils (red and

---

[5] https://ww1.microchip.com/downloads/en/DeviceDoc/APTM50UM09FAG-Rev3.pdf

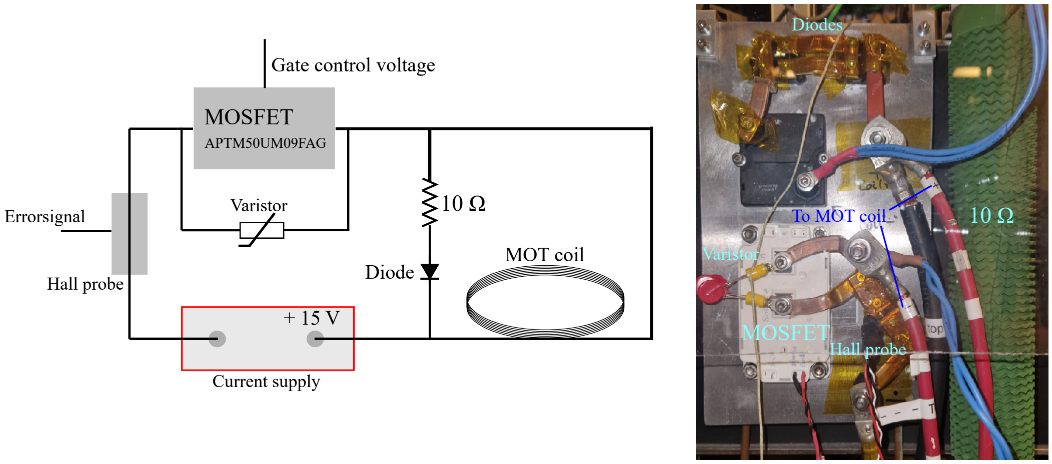

Figure 3.21: Schematic of the MOT coil circuirts. A MOSFET is used to regulate the current through the MOT coils on ≈ 1 ms time scales. The current in each MOT coil, measured by a Hall probe, is stabilized to a reference voltage by using a PID circuit.

blue graph, respectively). The magnetic field is measured with a Gaussmeter probe placed above the magnetic coils. The characteristic decay time for the old coils is $\tau = 10.33 \pm 0.04$ ms, whereas the new coils are an order of magnitude better at $\tau = 1.05 \pm 0.02$ ms. With the new coils the dynamics are much more suitable for catching atoms in the red MOT after releasing them in the blue MOT.

3.5.3 Bias fields

The bias fields are formed by three pairs of Helmholtz configuration coils, wrapped around the vacuum chamber. This gives us the freedom to move the MOT could in the x, y and z direction. We run the y-coils (horizontal, perpendicular to the cavity axis) at 1.67 A. The z-coils are run at a higher current of $3.5-4$ A, as they also form the bias field of ≈ 2G which increases the emission of the atoms into the cavity and forms a well defined quantization axis for targeting specific magnetic sublevels. The bias fields are always left on to limit experimental complexity, but the constant contribution from the z-coils means that the we have to create deliberate imbalance in the top and bottom MOT coil current to center the atomic cloud in the cavity before releasing it from the red MOT.

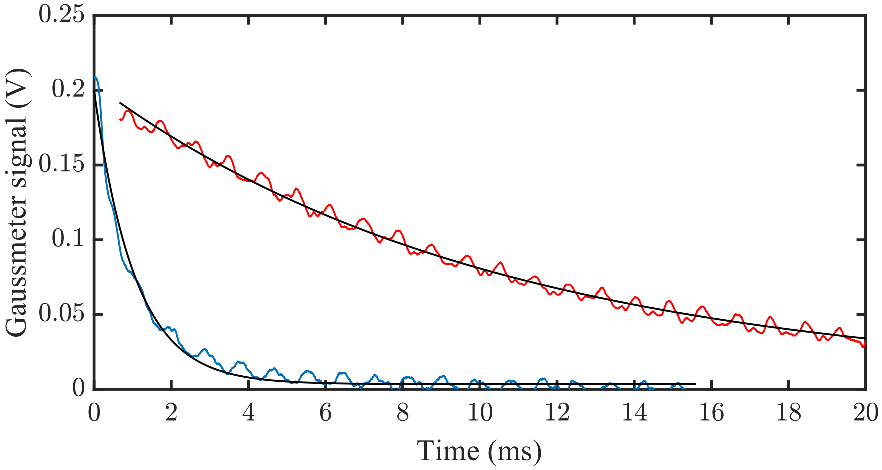

Figure 3.22: Magnetic field decay times for old and new coils. In red (blue), the old (new) MOT coils. The characteristic decay constant is $\tau = 10.33 \pm 0.04$ ms ($\tau = 1.05 \pm 0.02$ ms). The 1 kHz noise is from the Gaussmeter itself.

CHAPTER 4

Preparation and characterization of atoms

When starting my PhD, the big project on the horizon was the implementation of a 689 nm red MOT. This would give us a significantly colder ensemble of atoms, down to just a few µK, which would place the system in the bad cavity regime. By realizing the intracavity red MOT we had built a solid experimental platform to conduct studies of superradiant emission. In this chapter, we discuss the preparation and characterization of atoms with the goal of achieving a strong atom-cavity coupling to facilitate such experiments.

4.1 Experimental sequence

The timing of the experiment sequence is controlled using a national instruments card. The NI card is interfaced using a home built GUI (”StrontiumBrainGUI”) written in python that provides control over TTL timings (bottom left) and analog output (AO) voltages (bottom right). The TTL timings control the red and blue MOT light, the red and blue MOT light shutter, the imaging AOM, the camera trigger, the transition between the SF and BB red MOT, and the pumping pulse. The two AO’s of the NI card control the MOT coil currents. We define different voltages for each of the MOT coils for blue and red operation, and we have the option to ramp up the magnetic field towards the end of the red MOT. It is important to have precise control over the red MOT control voltages, as the MOT position is very sensitive to magnetic fields when the magnetic field gradient is low - being off by just 10’s of mV can result in the MOT not being centered in the cavity

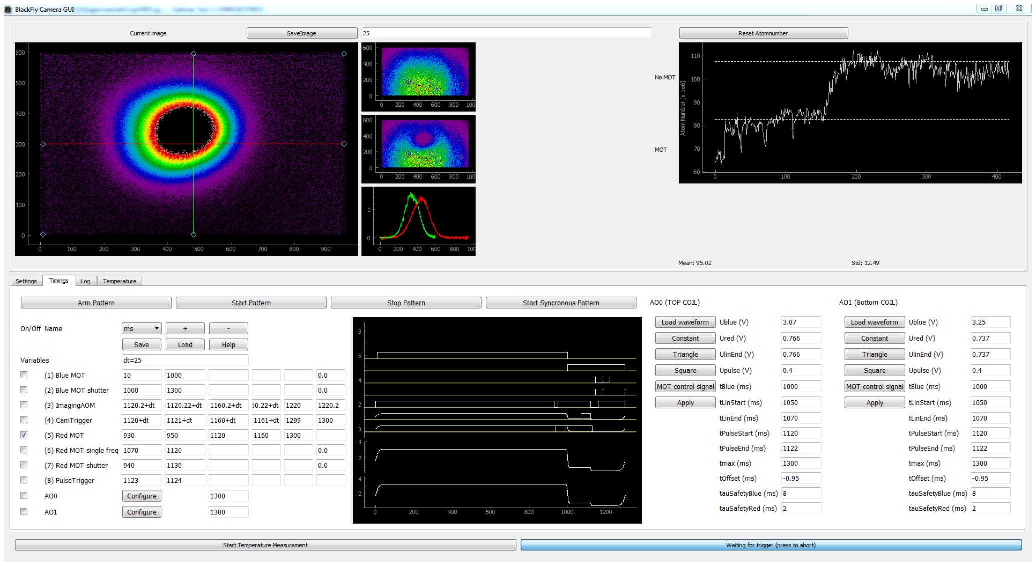

25

Mean: 95.02

Std: 12.49

Variables dt=25

On/Off	Name						
☐	(1) Blue MOT	10	1000				0.0
☐	(2) Blue MOT shutter	1000	1300				0.0
☐	(3) ImagingAOM	1120.2+dt	1120.22+dt	1160.2+dt	50.22+dt	1220	1220.2
☐	(4) CamTrigger	1120+dt	1121+dt	1160+dt	1161+dt	1299	1300
☑	(5) Red MOT	930	950	1120	1160	1300	
☐	(6) Red MOT single freq	1070	1120				0.0
☐	(7) Red MOT shutter	940	1130				0.0
☐	(8) PulseTrigger	1123	1124				
☐	AO0	Configure		1300			
☐	AO1	Configure		1300			

AO0 (TOP COIL)		AO1 (Bottom COIL)	
Ublue (V)	3.07	Ublue (V)	3.25
Ured (V)	0.766	Ured (V)	0.737
UlinEnd (V)	0.766	UlinEnd (V)	0.737
Upulse (V)	0.4	Upulse (V)	0.4
tBlue (ms)	1000	tBlue (ms)	1000
tLinStart (ms)	1050	tLinStart (ms)	1050
tLinEnd (ms)	1070	tLinEnd (ms)	1070
tPulseStart (ms)	1120	tPulseStart (ms)	1120
tPulseEnd (ms)	1122	tPulseEnd (ms)	1122
tmax (ms)	1300	tmax (ms)	1300
tOffset (ms)	-0.95	tOffset (ms)	-0.95
tauSafetyBlue (ms)	8	tauSafetyBlue (ms)	8
tauSafetyRed (ms)	2	tauSafetyRed (ms)	2

Figure 4.1: The camera GUI hosting the TTL and AO controls, along with a panel for displaying the absorption images. In the upper right corner, the atom number over time is plotted.

after the red MOT stage. The StrontiumBrainGUI is imported into a tab in a separate ”CameraGUI” GUI and combined with another server script, the ”BlackFlyCameraServer” to show both experimental timings and absorption images in the same window. Figure 4.1 shows an example of the camera GUI in operation, with the timings and absorption images in the bottom and top panel respectively. For more details on the interplay of the scripts involved in creating this GUI, I recommend reading the thesis of Mikkel Tang [61, p. 50], a former PhD student on the experiment.

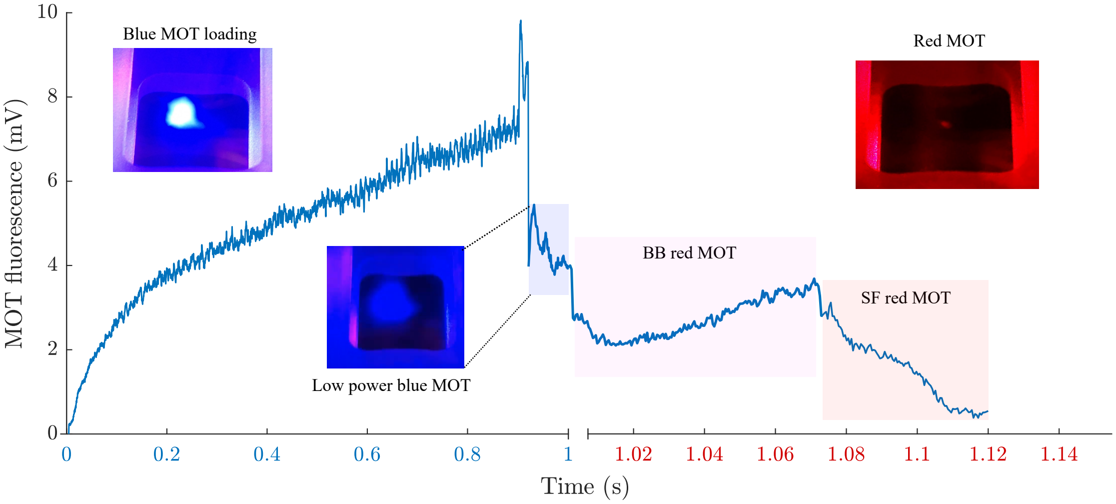

Figure 4.2: The experimental sequence by fluorescence of the MOT cloud. The blue MOT builds up a strong fluorescence signal over the course of 1000 ms, which drops upon transferring atoms to the red MOT.

Stage	Duration	Temperature T
blue MOT loading	950 ms	3-5 mK
low power blue MOT	50 ms	1-3 mK
strong BB red MOT	70 ms	10-20 µK
weak SF red MOT	50 ms	2-3 µK

4.2 Experimental sequence

The cooling and preparation cycle can be divided into four cooling stages. Figure 4.2 shows the MOT fluorescence as captured by a lensed camera sitting 30 cm above the science chamber. Note that the scale on the time axis changes between the blue and red MOT. The fluorescence signal is very sensitive to camera alignment, and it optimized to detect red MOT fluorescence.

The first cooling stage of the experimental sequence is 950 ms of blue MOT loading with maximum power in the blue MOT beams. Before we transfer atoms to the red MOT, we run a second stage blue MOT at half the optical power for 50 ms. The reduced power makes the blue MOT bigger and more diffuse, but significantly increases the transfer efficiency between the blue and red MOT by around a factor of two. The red MOT has two stages, a broadband (BB) and single frequency (SF) stage (for more details on the red MOT operation, see section 3.2.3). The BB red MOT slowly increases the fluorescence signal as the atoms are gathered from the cloud of atoms released from the blue MOT.

The fourth and final cooling stage is a 50 ms SF red MOT. The power in the MOT beams is linearly ramped an order of magnitude down over the course of the cooling stage. We tune the magnetic fields of the red MOT such that the atoms ends up centered in the cavity mode upon turning off this final cooling stage. Figure 4.3 shows absorption images taken from the start of the red MOT ($t = -120$ ms), up to the end of the red MOT and the start of experiments. Interestingly, the apparent optimal position for the blue MOT does not spatially overlap with the final position of the intracavity red MOT, and the atoms can be seen moving several mm when condensing into the red MOT cloud. This likely depends on an interplay between various parameters that we have not yet had the chance to study thoroughly, but the overall transfer efficiency between the blue and red MOT remains good.

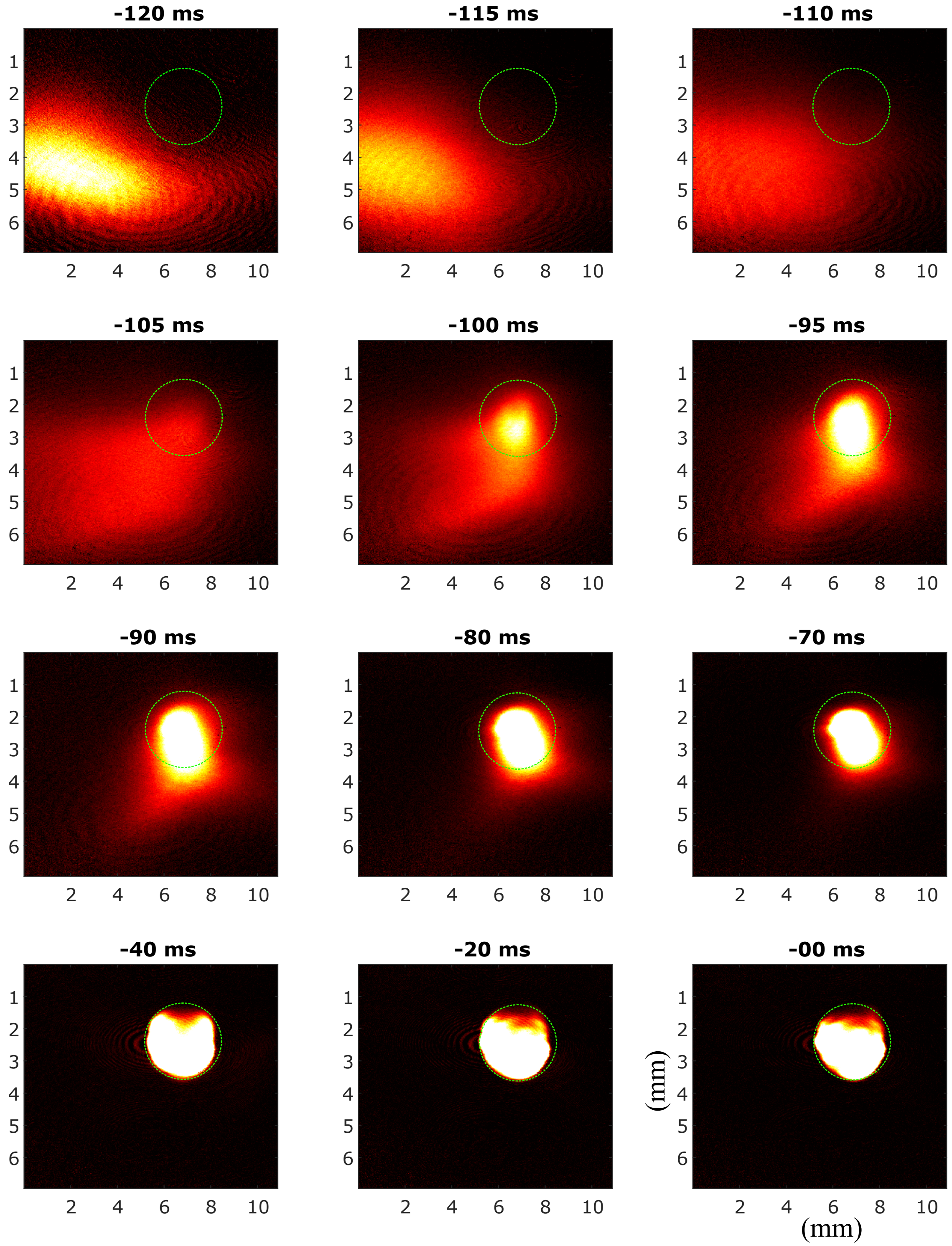

Figure 4.3: Absorption images of the red MOT (BB and SF) taken in increments from the end of the blue MOT (-120 ms) till the red MOT is turned off (0 ms). At the -50 ms mark, the BB MOT is replaced by the SF MOT, and the sample becomes more dense. The MOT is gathering in a different spot than the center of the blue MOT. The dashed green circle indicates the final position of the red MOT.

After the cooling stages, we turn off the MOT coils, and only the bias fields remains. We wait 3 ms before performing any experiments atoms to give the magnetic fields of the MOT coils time to ramp down. The vertical bias field is strongest and provides a quantization axis for pumping, repumping, and it is used to increase the rate of emission into the cavity mode. The bias fields split the magnetic sublevels by ±4 MHz, which prevents interference between superradiant emission of the different magnetic sublevels. With the atoms cooled and prepared in the center of the cavity axis, we generally use the atoms for three types of experiments - which will be explained in depth in the coming chapters.

- **Pulsed superradiance** - we produce short superradiant pulses on the $^1S_0 \rightarrow ^3 P_1$ transition by driving the atoms with a strong resonant beam. The beam is incident from a 90°angle such that the atoms does not inheret the phase of the pumping beam. We study the strength and the delay time of the superradiant pulses, and manage to produce several superradiant pulses using the same atomic ensemble before the atoms fall out of the cavity.

- **Continuously repumped superradiance** To increase the duration of the superradiant lasing and gauge the frequency stability, we continuously repump the ensemble. This is done by turning on a 688 and 689 nm repumper after the sample preparation, leaving the 679 and 707 nm repumpers on the whole time. Increasing the pulse length allow us to reach a lasing linewidth much lower than the natural linewidth of the lasing transition.

- **Superradiant Ramsey readout** We leverage the superradiant pulses to realize a cavity assisted read out scheme for a Ramsey type interferometer. The read out is non destructive to the atomic ensemble, which means that we can interrogate the same sample many times, as compared to traditional read out techniques which scatters many photons.

We save data by pulling it directly off the screen of an RTB2004 oscilloscope. The oscilloscope sends the data over LAN to our server ”datalager”. Next, we will discuss some of the tools that we have used or still use to evaluate the performance of the red MOT.

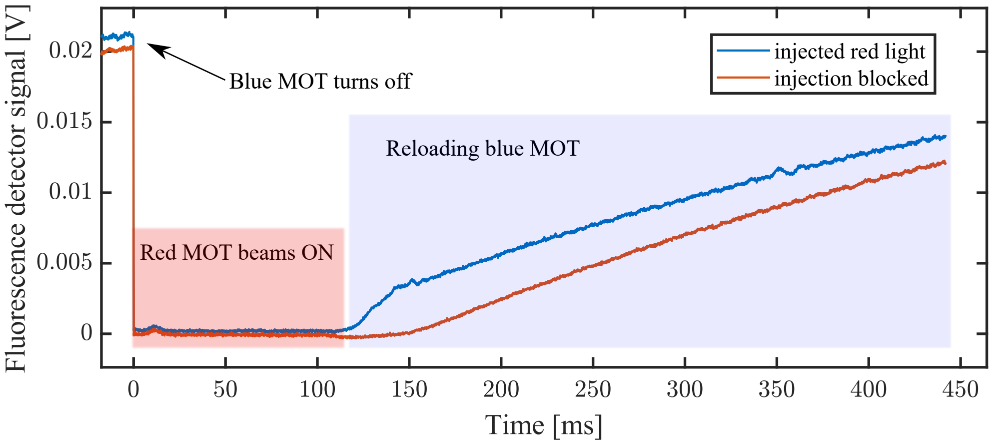

Figure 4.4: Using the fluorescence to find the first trace of the red MOT. The blue MOT is turned off for 100 ms where we shine the red MOT beams. When the red light is at the right frequency (injected), we see that the loading rate of the blue MOT after turning of the red MOT beams is increased, indicating that the red MOT beams are trapping, or at least slowing, the atoms.

4.3 Early realization of a red MOT

The implementation of a red MOT cooling stage resulted in a few upgrades on the experiment; new 689 nm laser systems and AOMs, precise magnetic field control, broadband wave plates compatible with 461 nm and 689 nm light, and a lensed imaging system. These upgrades adds a multitude of new uncalibrated variables, such as AOM frequencies, scan ranges, MOT beam power balances, and magnetic field offsets - just to name a few. To optimize these variables before actually observing the red MOT in the absorption images is challenging - At the time, we had to largely rely on intuition and educated guesses. Even if we manage to slow or catch atoms in the red MOT, there is no guarantee that the atom cloud will condense within the absorption imaging region, as the red MOT is much more sensitive to background magnetic fields than the blue MOT.

Instead of using the absorption images to look for the red MOT, we can measure the fluorescence when flashing the blue MOT beams. By reloading a blue MOT just after turning off the red MOT, we can look for signs that some of the atoms got trapped by the red MOT and got reloaded into the blue MOT. In Fig. 4.4 the fluorescence is shown with the red MOT beams at the right and wrong frequency (injected or free running laser diode). The difference is very noticeable in the beginning of the blue MOT loading - the step in the fluorescence indicates that a significant proportion of the atoms remains within the

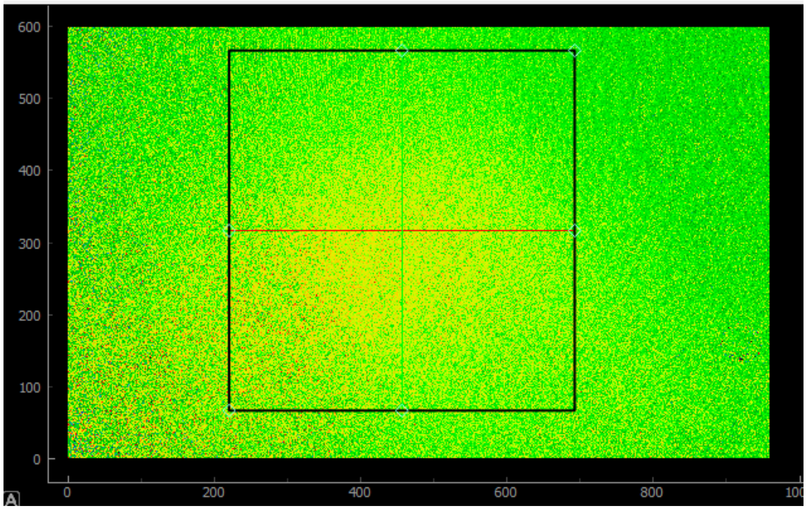

Figure 4.5: First image of atoms confined in a red MOT.

MOT capture region. This provides a metric that can be optimized by iteratively tuning the MOT parameters and beam alignment when increasing the red MOT duration. This technique is what gave us the first signs of atoms in the red MOT, and after optimizing the size of the fluorescence step we were able to see the red MOT with the imaging system. Figure 4.5 shows[1] the very first absorption image of the red MOT.

With the atoms caught in the red MOT, the next step is to facilitate the atom cavity interaction. To adjust the position of the red MOT, we tune the vertical and horizontal bias fields. The intracavity locking light is one FSR away (-780 MHz) from atomic resonance, and has very little influence on the atoms. However, if we use the fiber EOM to generate ±780 MHz sidebands on the locking light, the higher frequency sideband will be resonant with the atoms. The cavity finesse amplifies the power of the resonant sideband enough to completely saturate the atoms inside the cavity mode. If the intracavity resonant light is flashed just before imaging the atom cloud, a significant part of the atoms will be in the $^3P_1$ state ($\approx 50\%$ for saturation) and contribute to the image. We utilize this method to locate the cavity axis in the absorption image. In Fig. 4.6 two MOT realizations are shown; with and without resonant cavity light. The cavity axis is clearly visible through the red MOT in the picture with the resonant cavity light present.

The shape of the MOT in these pictures is not what you would expect from a red MOT.

---

[1] to the trained non-colorblind eye

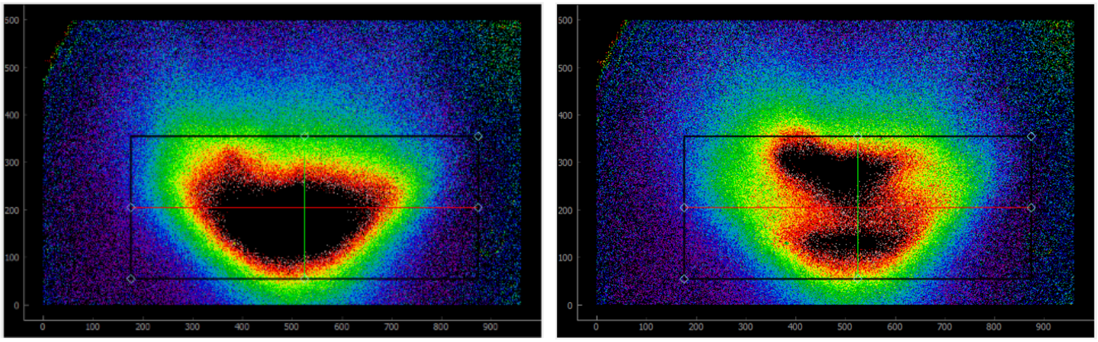

without resonant cavity light

with resonant cavity light

Figure 4.6: An early version of the red MOT with the old 689 nm laser system. Due to frequency noise on the laser, the cloud could not be condensed. However, the MOT is still sensitive to resonant 689 nm light. This we leveraged to scout for the optical cavity axis in the absorption image. The picture on the right has several µW of resonant 689 nm light resonant in the optical cavity, which creates a sizeable hole in the absorption profile of the cloud.

Although the temperature of the atom cloud is significantly lower than the blue MOT, a red MOT is usually much more compact due to a lower temperature and a much smaller capture range [57, 100]. Here, the size of the red MOT is comparable to that of the blue MOT. After working through the variables, we determined that the problem was frequency noise on the laser used to inject the 689 nm diode that generates the red MOT beams. Upon switching to a new and improved reference laser for injecting our red 689 nm diodes, the red MOT became significantly more compact (as seen in other absorption images of the red MOT presented in this thesis).

4.4 Absorption imaging

Absorption imaging constitutes our primary sense for evaluating the red MOT atom number, position, and temperature. We use 40 µs imaging pulses with ≈ 100 µW of on-resonance 461 light launched from a fiber. The beam is collimated with a diameter of ≈ 1 cm. This beam is passed through the center of the science chamber where the MOT resides, and the atoms inside the beam profile will absorb some of the photons passing through. When the intensity of the imaging beam is much below the saturation intensity of the transition, we write the attenuation of an on resonance beam passing through an atomic medium using Beer's law,

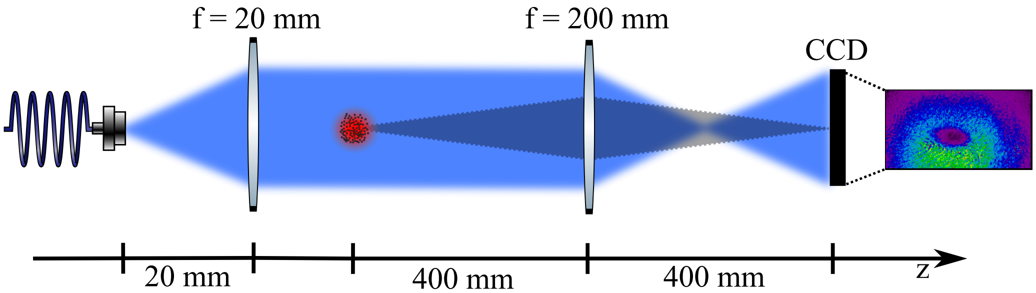

Figure 4.7: The lensing setup for the imaging system. The setup uses two $f = 200$ mm lenses to produce a 1:1 image of the MOT plane.

$$I(z) = I_0(z)\exp(-OD) \tag{4.4.1}$$

where OD is defined as the optical density. The OD can be written as $\sigma_0 n$, where n is atomic density and

$$\sigma_0 = \frac{3\lambda_0^2}{2\pi} \tag{4.4.2}$$

is the absorption cross section. After exiting the science chamber, the beam then passes through a lens (figure 4.7). This lens is placed at twice its focal length from the MOT cloud, and the beam is directed towards a CCD camera separated from the lens also by twice the focal length. This images the exact plane of the red MOT on the CCD camera (BFLY-U3-23S6C-C) with a magnification factor of 1. Comparing the picture of the imaging beam with and without the shadow of the MOT present we can calculate the atom number $N_{i,j}$ present in each pixel using that the density of atoms $n = N \cdot A$,

$$N_{i,j} = \frac{A}{\sigma_0} \ln\left(\frac{\text{noMOT}_{i,j}}{\text{MOT}_{i,j}}\right) \tag{4.4.3}$$

where $A = (2 \cdot 5.86 \cdot 10^{-6})^2$ m (due to binning) is the area of each pixel in the picture. Summing over i and j yields the total atom number present in the picture. This method is insensitive to the intensity profile of the imaging beam, as it measures the optical depth at each pixel. However, for high ODs, the calculated atom number can be artificially low if not all the imaging light is at the right frequency, such as is the case with a partly injected diode laser (which is why we derive the imaging light directly from the TOPTICA DL PRO). Furthermore, discretization errors might appear when the intensity of the imaging light becomes low. If the value of a pixel is zero, this translates to an infinitely high atom

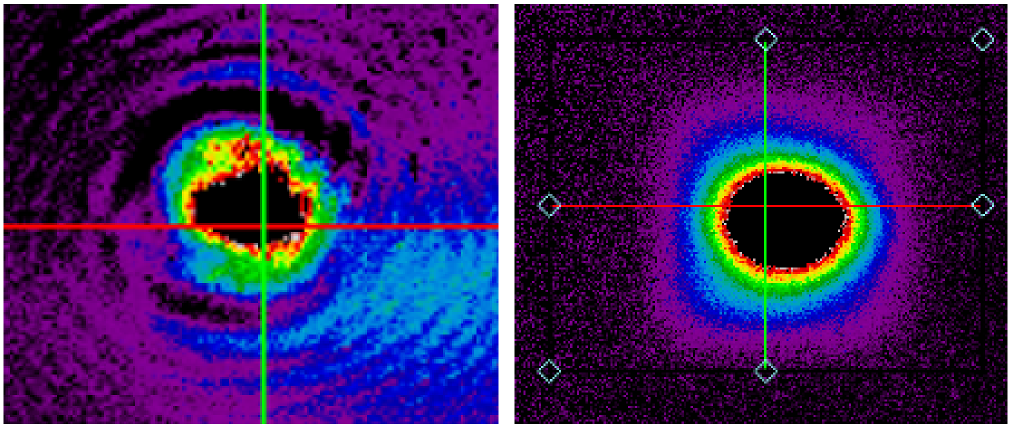

Figure 4.8: The difference between using a plane wave imaging method (left), and a proper imaging of the MOT plane (right).

number. In practice, this is fixed in the post processing of the image by putting a limit on OD in each bin.

The two pictures used in this calculation are usually taken immediately after turning off the red MOT and 40 ms later. This is to give the atoms time to leave the imaging area completely (mainly due to gravity). To accurately measure the atom number in the MOT, we start the imaging sequence 25 ms later to let the cloud expand (to a lower OD) before we start the sequence of images. We use the same delay of the imaging to not interfere with the superradiance experiments.

With this technique it can be useful to take a third picture without any atoms and without any light to subtract the background light from both images. The background can have a significant effect on the perceived OD, but with adequate screening of the camera we found no significant difference between using the third picture or not.

Fig. 4.8 shows two absorption images of the red MOT. The left image is using a plane wave imaging beam without imaging the MOT plane. As a result, the diffraction induced by the dense red MOT is very noticeable. The right image is using a proper 1:1 imaging setup, showing a red MOT with $N = 40e6$ atoms. The calibration of the pixel sizes from the camera spec sheet is verified by comparing the free fall of the atoms to the expected trajectory, since we are imaging perpendicular to gravity.

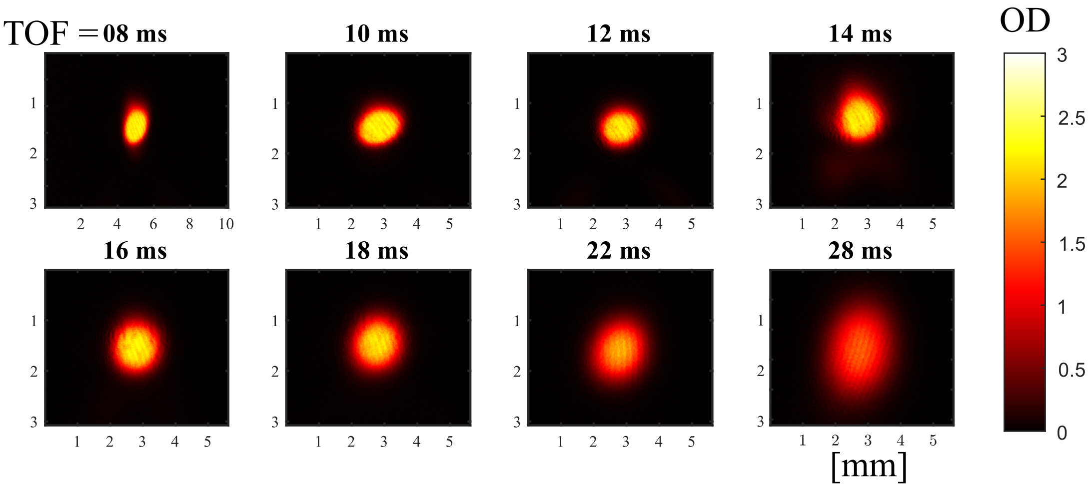

Figure 4.9: Time of flight measurement of the atomic cloud.

4.4.1 Thermal expansion

We cool the atoms in red MOT to reach the regime where the FWHM of the Doppler broadening is significantly smaller than the cavity linewidth $\gamma_{\text{Dopp}} \ll \kappa$. This improves the cavity mediated coupling between individual atoms, and puts the laser emission in the bad-cavity regime. A common way to characterize the temperature of the ensemble is to study the time dependent width of the atom cloud as it thermally expands after being released from the MOT. A series of such pictures is shown in Fig. 4.9. Assuming that the atom distribution is Gaussian, the time-dependent width of the cloud can be written as [101]

$$\sigma(t) = \sqrt{\sigma_0^2 + \sigma_v^2 t^2}, \tag{4.4.4}$$

where σ_0 is the initial width of the cloud, and

$$\sigma_v = \sqrt{\frac{k_B T}{m_{\text{sr}}}}. \tag{4.4.5}$$

is the time-dependent term that is governed by the temperature, T. In Fig. 4.10 we fit the time-dependent width of the atom cloud in Fig. 4.9 to Eq. 4.4.4. This yields a temperature

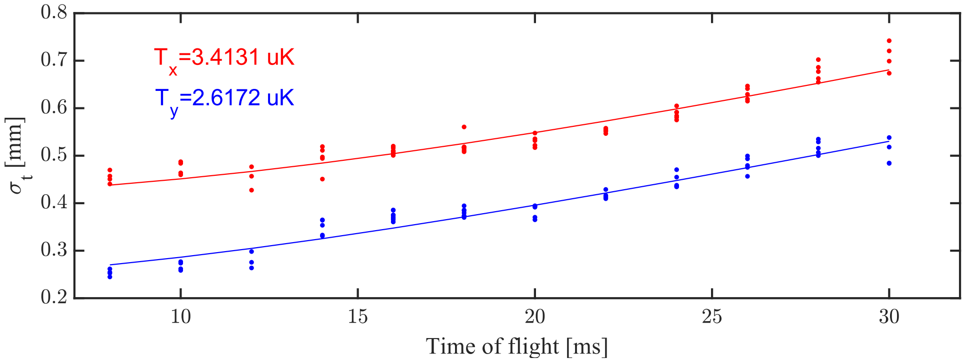

Figure 4.10: Time dependent width of the atom cloud. The fit to Eq. 4.4.4 can be used to determine the temperature of the ensemble.

in the x- and y direction of around $2-3$ µK, which corresponds to a Doppler FWHM of

$$\gamma_{\text{Dopp}}/2\pi = \sqrt{\frac{8kT\ln(2)}{mc^2}}f \approx 47 \text{ kHz}, \tag{4.4.6}$$

which is more than an order of magnitude lower than the cavity linewidth, $\kappa/2\pi = 800$ kHz. However, to give a decent estimate of the temperature of the red MOT it not usually required to take long series of MOT pictures. If the cloud is imaged when it has had time to expand significantly compared to its initial size, $\sigma_v t \gg \sigma_0$, the temperature can approximated by a single image,

$$\sigma_v = \sqrt{\frac{k_B T}{m_{\text{sr}}}} \cdot t, \tag{4.4.7}$$

as it is reasonable to assume a linear expansion of the atomic cloud. This means that the temperature can be approximated after each experimental cycle, whether it is with superradiant pulses, continuous repumping, or a superradiant Ramsey readout.

4.4.2 Gravitational sag

In the SF red MOT, gravity plays a role in shaping the cloud. This is because the low trapping force when scattering photons off the $^3P_1$ state with lifetime $\tau = 21.3$ µs can become comparable to gravity. For each photon absorbed from the red MOT beam, an

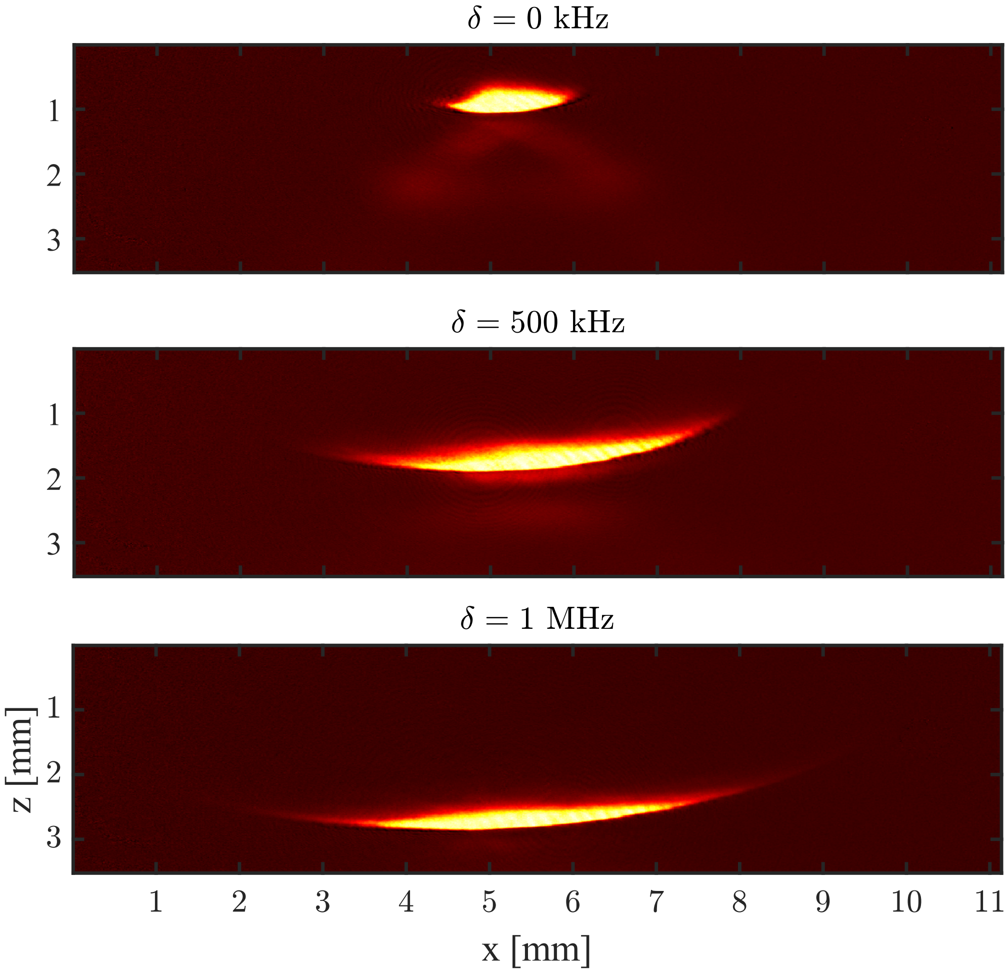

Figure 4.11: The gravitational sag of the SF red MOT for different red MOT detunings. The atoms arrange themselves in elliptical shells where the Zeeman shift is equal to the red MOT detuning.

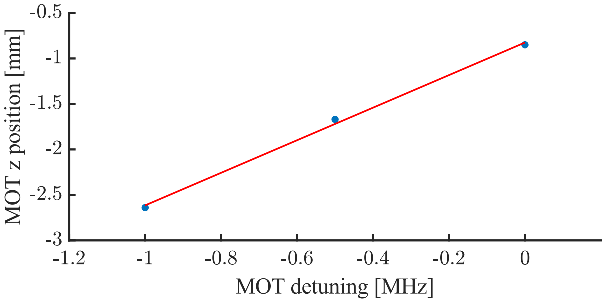

Figure 4.12: Magnetic field gradient calculated by sagging red MOT. The slope of the linear fit is 1.79 mm/MHz.

atom gains a velocity of

$$v_{\text{recoil}} = \frac{\hbar k}{m_{sr}}. \tag{4.4.8}$$

To counter gravity, an atom must absorb at least 1.5 photons every ms. Since the MOT beams at this stage operate with a single frequency addressing a narrow atomic transition, the trapping force is only big enough to counter gravity when the MOT beam frequency match the splitting of the magnetic sublevels. Depending on how much the MOT beams are red detuned in frequency, the atoms can be observed falling into elliptical shells where the magnetic field gradient again makes them resonant with the MOT beams. The outline of the atom shells are elliptical with a 2:1 length ratio, as the magnetic field gradient is twice as high along the z-axis. An example of this behavior is seen in Fig. 4.11. For bigger detunings the resonant elliptical shell becomes bigger and flatter in the bottom, which smears out the atom distribution horizontally. The center of these sagging MOT clouds can be used to determine the spatial magnetic field gradient, as seen in Fig. 4.12. The magnetic sublevels of $^3P_1$ gets shifted with 2.1 MHz/G. From the fit of MOT position versus MOT detuning on the plot, we can infer the magnetic field gradient to be 3.74 G/cm.

This effect is only visible if you have a well defined frequency of your red MOT beams. The fact that we could not observe this upon our first red MOT realization was one of the contributing factors that led to the replacement of the laser injecting the diode running the red MOT beams.

4.5 Resolved NMS regime

So far, we have mainly discussed the application of the imaging system to characterize our atomic ensemble after the cooling sequence. Through absorption of a weak blue probing beam, we can gauge the number of atoms and the shape of the atomic cloud. However, the atom number in the red MOT matters little if the atoms are not coupled well to the cavity. The final atom number can be high for a MOT cloud like shown in Fig. 4.11, but such a cloud does not couple well to the cavity, as most of the atoms are outside the waist of the fundamental cavity mode. In the end, the important metric is the amount of cavity coupled atoms and the strength of their interaction.

The NMS provides an important metric as it depends on g_0 (which is fixed) and the square root of the intracavity atom number N. The NMS can be measured using the transmission of the science cavity with a laser close to atomic resonance. From the theory discussed in

2.5.3, if the cavity is held on atomic resonance $\delta_{\text{cav}} = 0$, we observe a cavity transmission at probing laser frequencies $\delta_l = \pm\Omega_N/2$, where δ_l is the laser detuning from atomic resonance $\delta_l = \omega_l - \omega_a$. The probing laser is scanned linearly between these two resonances, and we calibrate the difference in time to a difference in frequency by using sidebands on the probing laser. This gives us a decent estimate of Ω_N. However, the signal-to-noise is low, as the resonant laser must operate at a fairly low power to not saturate the atoms (which lowers Ω_N), and the NMS resonances are drowned in background from the locking light resonant with the cavity one FSR away.

Instead, the NMS can be measured fast and with a high signal-to-noise by simply beating the cavity transmission against our reference laser. By conducting the measurement in a MHz beat note, the entire background from the cavity locking light is removed. As an added benefit, this technique requires no time-to-frequency calibration, as the information about the center frequency of the NMS resonances is given by the beat note.

To measure the NMS in a beat experiment, we add a pair of sidebands on the locking light. Figure 4.13 depicts the frequency modulation chain to generate frequency components for simultaneous locking and NMS probing. The locking light is one FSR from atomic resonance.

A DDS is generating a frequency corresponding to one FSR = 781 MHz. This signal is amplitude modulated by a mixer through a control voltage on the I port. The I port is driven with a frequency ω_{NMS}. After the mixer, the single tone of the DDS turns into two frequency components spaced symmetrically around the FSR at $\pm 2\pi\omega_{\text{NMS}}$. These frequency components are ramped in 2 ms with a linear frequency sweep, from 200 kHz to 10 MHz. When the science cavity locking light is modulated with this signal, it generates two optical frequency components sweeping away from the resonance frequency of the atoms, ω_a, from $\omega_a/2\pi + 200$ kHz to $\omega_a/2\pi + 10$ MHz, and $\omega_a/2\pi - 200$ kHz to $\omega_a/2\pi - 10$ MHz, respectively. When these optical frequencies are on resonance with the NMS modes at some point during the sweep, they are transmitted through the cavity, and a beat signal between the cavity output and our reference laser is observed.

The optical spectrum of the probing frequencies is also shown in Fig. 4.13. The frequencies for NMS probing and PDH locking are combined using the two output ports of a power splitter as inputs. The generation of additional sidebands at $\pm\text{FSR} \pm \omega_{\text{NMS}}$ lowers the amplitude of the PDH sidebands, which the locking electronics of the science cavity needs to be optimized for. The NMS can be measured in just 2 ms immediately after the red MOT and before the experiments without scattering a significant amount of photons. The

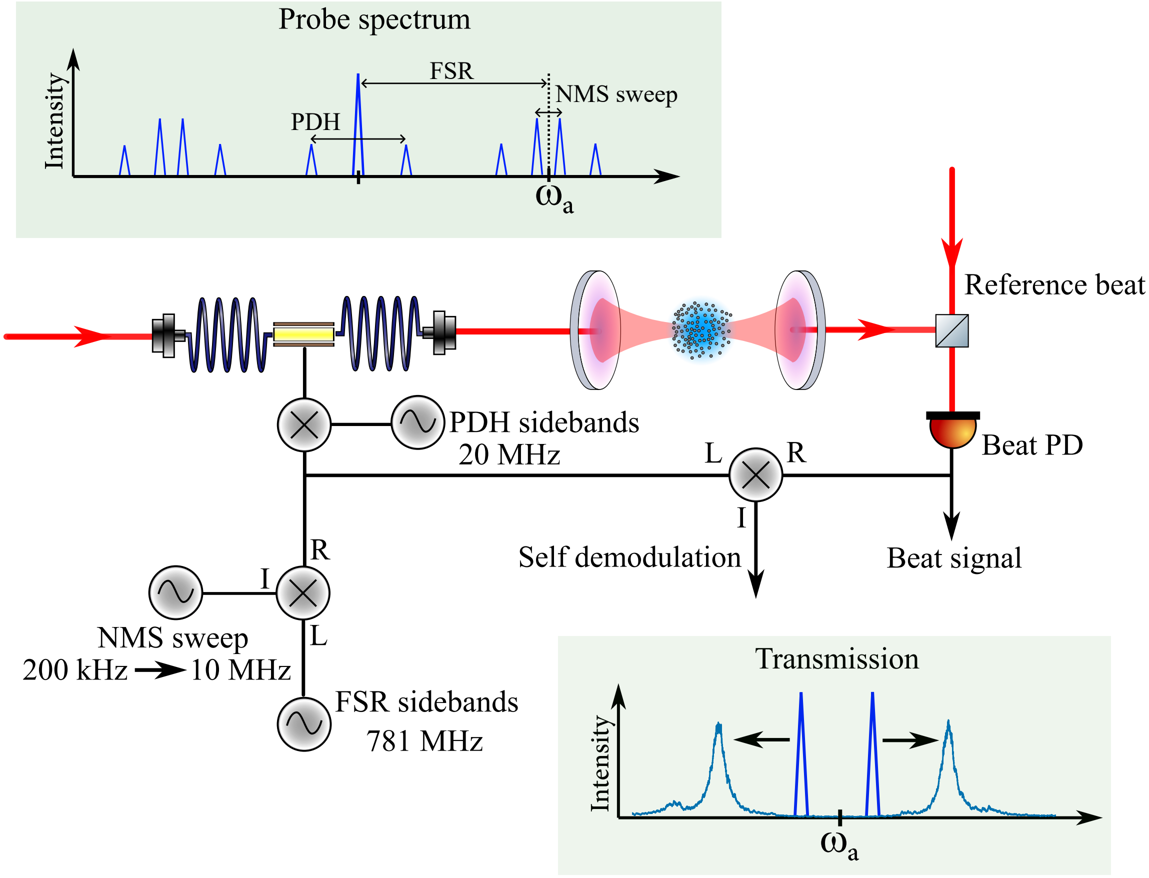

Figure 4.13: Scheme for probing the NMS. We generate additional sidebands at FSR $\pm\omega_{\mathrm{NMS}}$ to sweep across the upper and lower NMS solutions. The transmission of the cavity light is measured by beating against our reference laser, which removes the background noise from the locking light. Additionally, we can generate a noise filtered signal by demodulating the beat signal with the NMS sweep frequency by "self demodulation".

NMS measurement is started by triggering the sweep of the two NMS probing sidebands when the red MOT TTL signal turns off.

4.5.1 NMS self-demodulation

While the probing the NMS using an optical beat note is fast and low noise, one issue with this method is the bandwidth requirement of the data acquisition. Significantly more data points are needed to resolve a beat frequency, increasing the storage size of datasets. The critical point is when the oscilloscope takes longer than the experimental cycle to send data to the server. Missing data points means that long data sets with superradiant pulse statistics take even longer to complete. We address this by down mixing the beat note. We use the FSR $\pm\,\omega_{\text{NMS}}/2\pi$ signal generated by the mixer to demodulate the photodiode signal. The result is a NMS with a high signal-to-noise that requires much fewer datapoints. Later in this chapter this method is used to continuously probe Ω_N throughout the red MOT stage.

4.5.2 NMS probing applied

In Fig. 4.14 the cavity transmission is mapped as a function of laser detuning δ_l and cavity detuning δ_c. The absorption imaging indicates $N = 40e6$. The red dashed line follows $\delta_l = \delta_c$, the resonance criteria for no intracavity atoms. Instead, the cavity transmission is split into two solutions with a textbook avoided crossing around atomic resonance $\delta_l = 0$. When the cavity is on atomic resonance, $\delta_c = 0$, the splitting is $\Omega_N \approx 2\pi \cdot 5.3$ MHz and the resonances are well resolved (Fig. 4.15). Applying Eq. 2.5.7 with $g_0 = 2\pi \cdot 815$ Hz, this yields an intracavity atom number of $N_e = 21e6 \pm 0.1e6$, which is a little lower than the number suggested by absorption imaging. Since the longitudinal variation of the coupling is already taken into account by averaging g, the mismatch between the two numbers is either a sign that the transverse distribution of the MOT cloud cannot be ignored, or the atomic cloud is simply not centered in the mode of the optical cavity. It is also possible that the estimate of g_0 should be revised. If we instead calculate g_0 using the measured NMS and the atom number N obtained from absorption imaging, we get $g_0/2\pi = 635$ Hz. For now, Ω_N provides a useful metric for detecting shot-to-shot variation in atom number between MOT realizations.

With $\Omega_N \gg \kappa, \gamma_l$, the system operates in the strong coupling regime. In Fig. 4.15, a secondary set of peaks can be spotted around the NMS solutions. This is most likely the

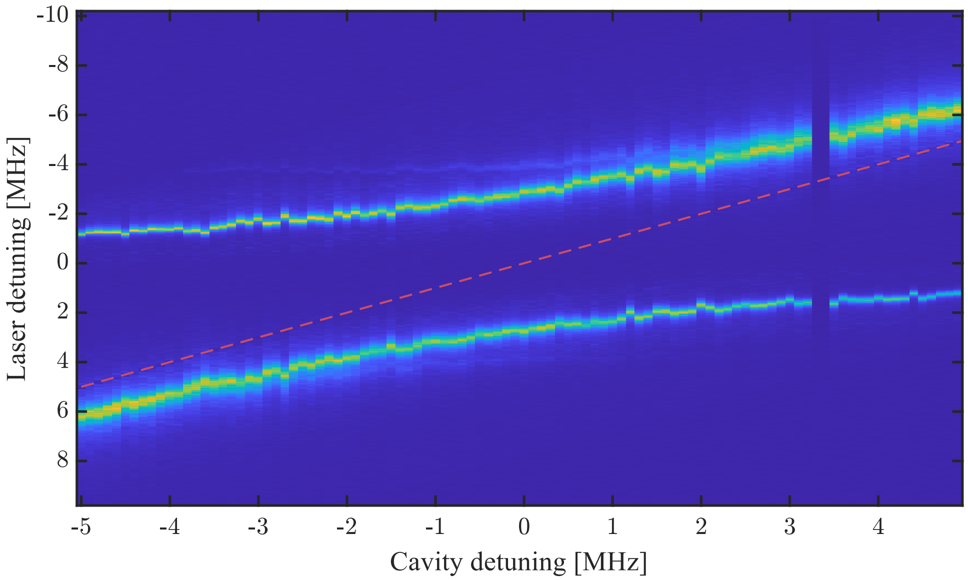

Figure 4.14: Two-dimensional scan of the NMS for $N = 40e6$ in the red MOT. The cavity transmission is split into two resonances which can be used to determine the number of intracavity atoms, N_e.

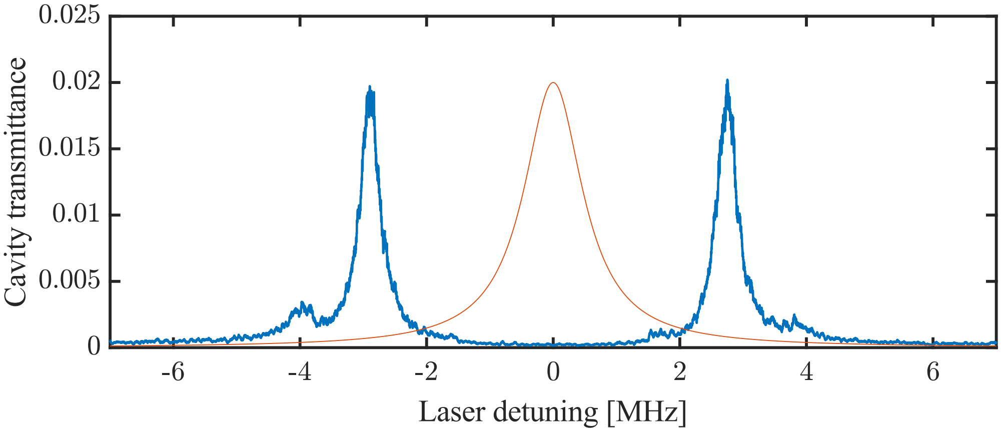

Figure 4.15: NMS for $\delta_c = 0$. In red, the expected Lorentzian line shape for a cavity with $\kappa = 2\pi \cdot 800$ kHz and no intracavity atoms.

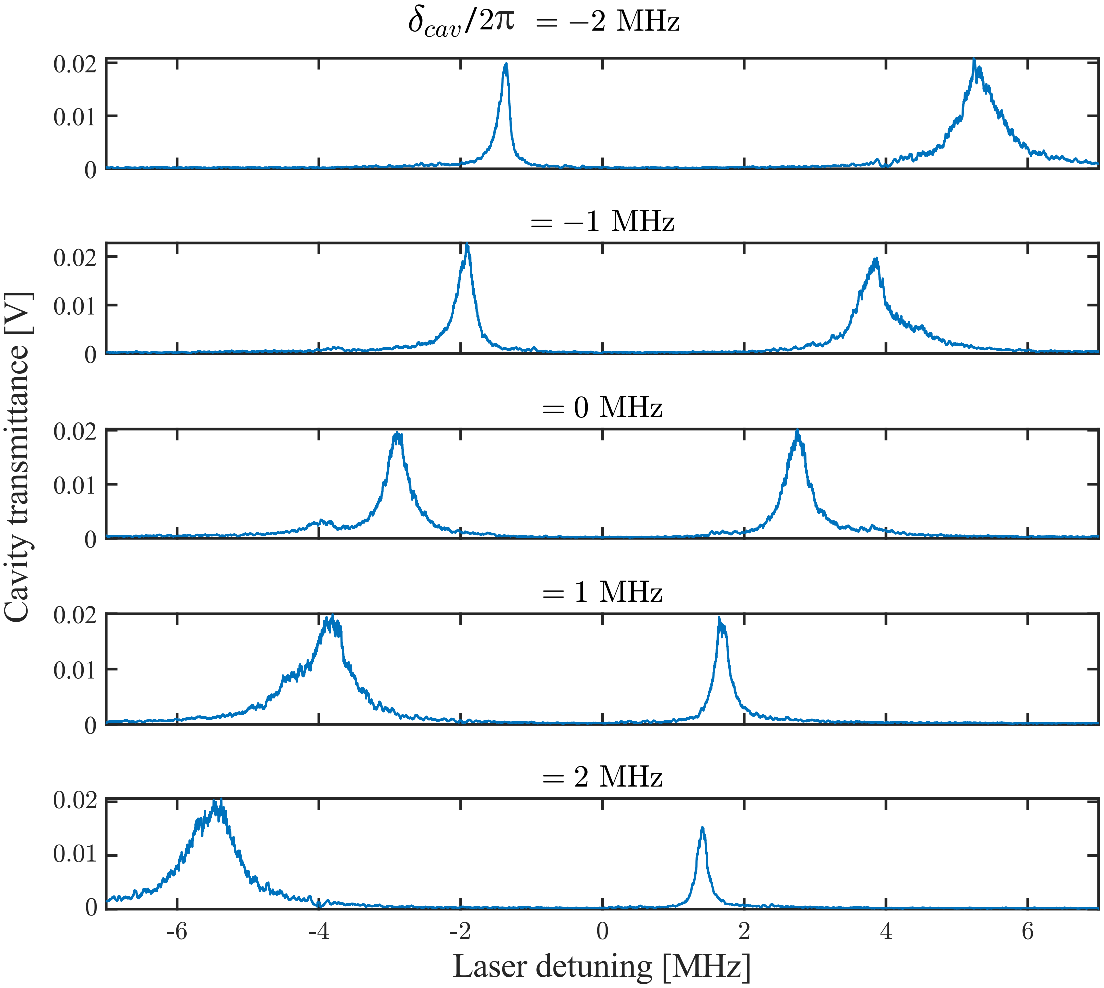

Figure 4.16: The NMS for 5 different detunings. For a large detuning, one of the transmission solutions is significantly stronger, and the line shape of both peaks appears visibly skewed due to the non linearity of the atomic and cavity dispersion curves.

contribution from the $m_j = \pm 1$ Zeeman substates, as these energy levels are expected to be shifted with ±4 MHz compared to $m_j = 0$. However, the NMS induced by the $m_j = \pm 1$ states is weak compared to the $m_j = 0$ NMS, as the polarization of the probing light is (intended to be) parallel to the magnetic field.

The line shape of each transmission is skewed and changes with δ_l and δ_c, which is a result of the non linearity of the two dispersion curves combining to produce alternative solutions for cavity transmission. This is clearly visible when plotting individual slices of Fig. 4.14 in Fig. 4.16.

4.5.3 Time-dependent NMS

Ultimately, we can use the NMS to monitor the number of atoms in the cavity throughout the cooling cycle. Leaving the cavity on atomic resonance $\delta_c = 0$, we continuously scan the EOM sidebands over the symmetrically shifted cavity resonances. We can measure the NMS every 2 ms seemingly without disturbing the operation of the red MOT.

The result is plotted in Fig. 4.17, where the red graph shows the raw data of cavity transmission over time. This data is generated by the self-demodulation technique (described in the previous chapter), where the beat signal is demodulated using the same frequencies that we use to generate the NMS probing sidebands. Using this scheme over measuring the frequencies of the beat note, it is necessary to convert the time axis into a frequency axis. This is easily done using knowledge of the scan span (10 MHz) and scan period (2ms).

The blue graph shows the time dependent Ω_N. Two vertical dashed lines marks the times at which we turn off the red MOT and pumps the atoms to produce superradiance. The number of intracavity atoms can be seen steadily increasing as the atoms are rearranging themselves from the BB red MOT to the SF red MOT. The atoms are packed considerably tighter in the SF red MOT, and the magnetic fields are optimized to center the last red MOT stage in the cavity. Worth noting is also that Ω_N peaks a few ms after turning off the red MOT. This is by design, as we need time to completely shut off the MOT quadropole fields. The center of the red SF MOT is intentionally a little higher than the center of the optical cavity. Upon turning off the red MOT, the atom cloud falls with gravity such that Ω_N peaks after a well defined bias field has been established. The atom cloud takes around 10 ms to completely leave the cavity mode. For us and the transitions that we experiment on, this is plenty of time to conduct atom-cavity experiments on the freely falling cloud.

To produce this graph, we have assumed that most of the atoms are in the ground state

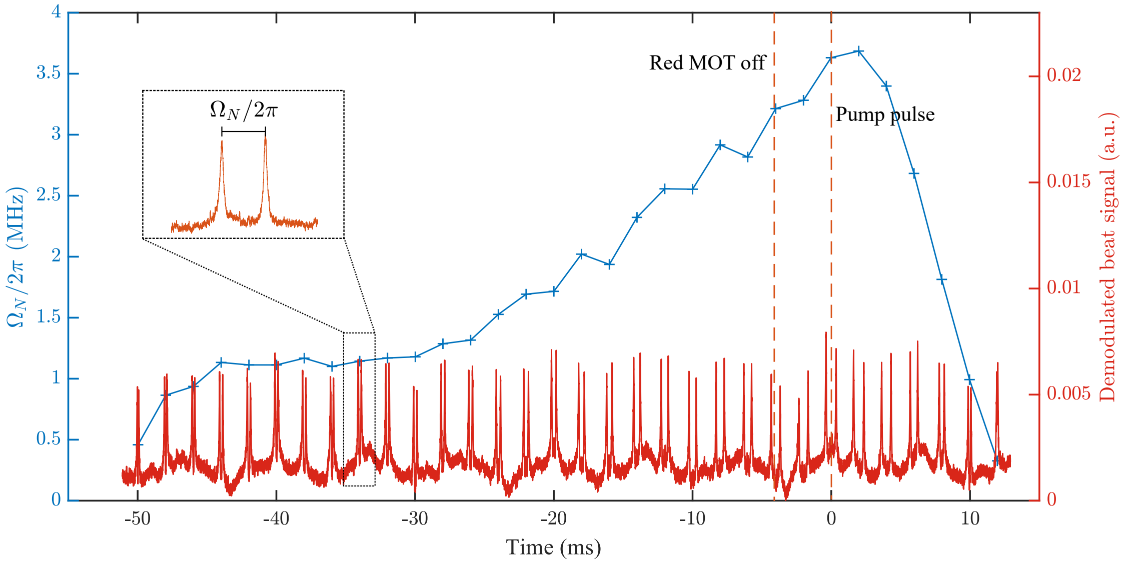

Figure 4.17: Time dependent measurement of Ω_N in the last part of the SF red MOT for $\delta_c = 0$. The red graph is the raw data of the sideband sweep probing the NMS cavity resonances. The blue graph shows the calculated value of Ω_N.

throughout the SF MOT and contribute to the NMS. From imaging the SF red MOT while the MOT beams are still on, a rough estimate is that maximally $5 - 10\%$ of the atoms are in the excited state at this stage. This is consistent with the amount of photons that the atoms need to scatter to counter gravity in the SF red MOT. Additionally, Ω_N does not increase significantly when the SF red MOT turns off.

CHAPTER

5

Pulsed superradiance

With cold atoms prepared by a red MOT in the center of the science cavity, our experiment is primed and ready to produce superradiant pulses.

Previously, our experiment generated lasing pulses on the $^1S_0 \rightarrow {}^3P_1$ transition using atoms cooled by a blue MOT only. Such pulses were used to test the model presented in [45] and could reach several hundreds of nW in peak power [61]. The simple experimental sequence with just one cooling stage can be leveraged to produce lasing pulses with a repetition rate of 1 ms, which has potential applications for laser stabilization [83]. In these experiments we are not able to attain the same pulse repetition rate as we have multiple MOT steps before interrogating the atoms. Rather, the generation of strong superradiant bursts on the $^1S_0 \rightarrow {}^3P_1$ transition serves as an important intermediate step towards the realization of continuous repumped superradiance and superradiant readout schemes. We use these pulses as a probe to optimize the atom cavity interaction and to gauge the typical system parameters. It is worth noting that the plots presented in this chapter are generated using data from different days in a time where the experimental results would improve at a rapid pace - meaning pulse characteristics can not be compared between different figures.

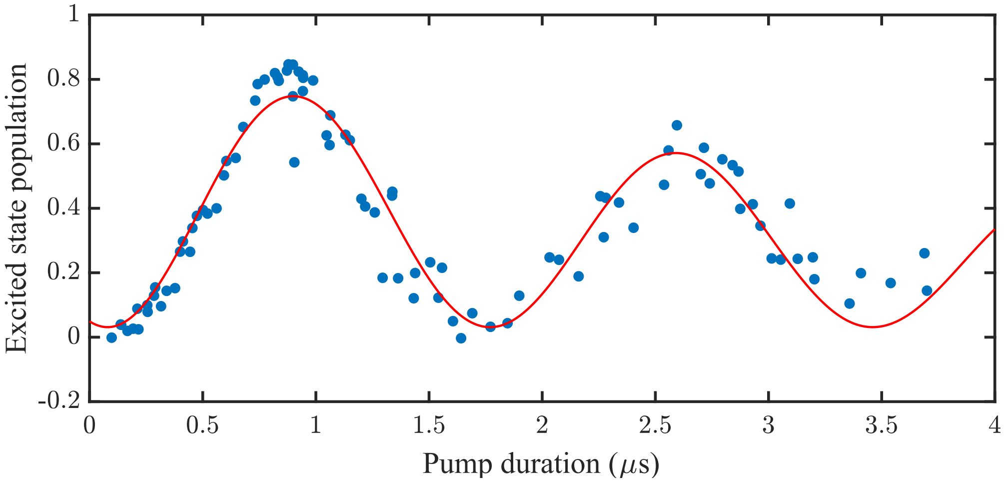

Figure 5.1: Rabi flopping on the clock transition. The considerable decay in contrast on a timescale faster than the natural lifetime is likely due to incoherent Rabi frequencies.

5.1 Optimization of superradiant bursts

We drive the intracavity atomic population from the ground state to the excited state using a π pulse. Such pulses have a duration of $400-700$ ns in our system, depending on the power of the pump beam. We typically use a pump beam with a power 16 mW, such that the atoms experience an intensity of $I \approx 1000\ I_{\text{sat}}$. This power broadens the transition sufficiently to drive the atom ensemble homogeneously, even though the estimated Doppler broadening is $\gamma_{\text{Dopp}}/2\pi \approx 40$ kHz. Figure 5.1 shows the population in the excited state for varying pump durations. This measurement is done using the fluorescence the gauge the number of atoms remaining in the ground state after a pump pulse, and it is associated with some uncertainty due to the relatively fast decay of the $^3P_1$ - the measured excitation fraction is likely lower than reality. From absorption images taken after an optimized π pulse, we infer that the excitation fraction is $80-90\%$. From the intensity profile of our pumping beam we expect that the ensemble does experience different Rabi frequencies, causing decoherence in the population oscillation. The fit is a sinusoidal oscillation multiplied by a decaying exponential to follow the contrast loss. From the fit, the Rabi frequency is determined to be $\Omega/2\pi = 570 \pm 10$ kHz.

Immediately after exciting the atomic population, we observe a superradiant pulse emitted from the cavity. The output power of the pulse is found from a calibration that compares a known cavity output power to the voltage of the photodiode recording the superradiant pulses. For most of the experiments described in this thesis, the calibration factor is ≈ 3 nW/mV. We optimize the superradiant pulses by tweaking a number of parameters;

- **Optimizing the SF red MOT frequency.** To strike the perfect balance between atom number, atom density and ensemble temperature, the SF frequency is tuned to maximize the atom cavity interaction. This optimization can also be done using the NMS measurement as discussed in the previous chapter.
- **Position of the red MOT.** We adjust the position of the red MOT finely with bias fields to create the maximum overlap between the atomic ensemble and the fundamental cavity mode.
- **Frequency and duration of the excitation pulse.** First, the frequency of the pump beam is optimized using a pulse duration that is purposely too short. Having optimized the frequency, the pulse duration is tuned to maximize the strength of the superradiant pulses.
- **Polarization of the pump beam.** Exciting the atoms with a polarization parallel to the bias field maximizes the spontaneous emission into the cavity, and limits the excitation of atoms into the magnetically sensitive $m_j = \pm 1$ states. The pump light polarization is aligned to the axis of the polarization maintaining fiber, and the output of the fiber is cleaned using a linear polarizer.
- **Alignment of the pump beam.** We tweak the alignment of the pump beam fiber launch to ensure that the atoms are driven with a high intensity and as coherently as possible.
- **Bias field strength.** Introducing a bias field perpendicular to the cavity increases the strength and consistency of the superradiant pulses. It limits interference between the m_j substates by introducing a big enough splitting that the $m_j = \pm 1$ are not populated even for a misaligned polarization of the pump beam. Figure 5.2 shows examples of pulses generated without a bias field (red) or with bias field with a strength of 1G. Time is measured since the end of the pump pulse. The peak emission time delay is notably smaller and more consistent when a bias field is present.
- **Cavity detuning.** The cavity detuning changes the superradiant dynamics as the atoms experience a lower coupling to the cavity when the cavity is detuned from atomic resonance.

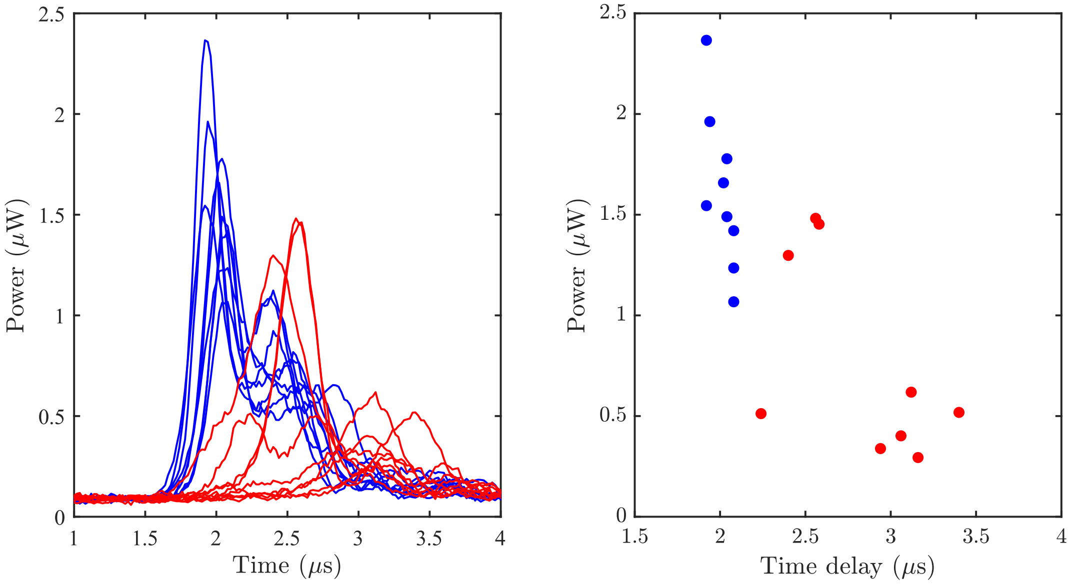

Figure 5.2: Superradiant pulses with (blue) and without (red) a bias field present. Time is measured since the end of the pumping pulse. The pulse amplitudes are higher and the time delays are more consistent when a bias field is present. The bias field increases the spontaneous emission into the cavity, and reduces the interference between magnetic substates of the excited level.

Besides the optimizations, we can modify the behavior of the superradiant pulses by seeding the lasing. Immediately after pumping the atoms to the excited state, we use the fiber EOM in the beam path leading to the science cavity to generate an additional sideband on atomic resonance. The power in the sideband is only a couple of nW, but it is more than enough to significantly influence the emission into the cavity. Figure 5.3 shows the effect of seeding the pulses (blue) versus pure atom cavity interaction (red). The time delay becomes smaller and more consistent (like the effect we see when adding a bias field). However, seeding the pulses with a constant intracavity field spoils one of the proposed benefit of superradiant light; mainly, that the lasing frequency is largely governed by the atomic coherence rather than the intracavity field. For our experiments with long, continuously repumped pulses A more likely application for seeded pulses is for a superradiant atomic state readout, as we shall discuss in a later chapter. In such a scheme the frequency stability of the lasing does not matter - we are only interested in the amplitude of the laser pulses, and consistent pulses makes for a more robust atomic state readout.

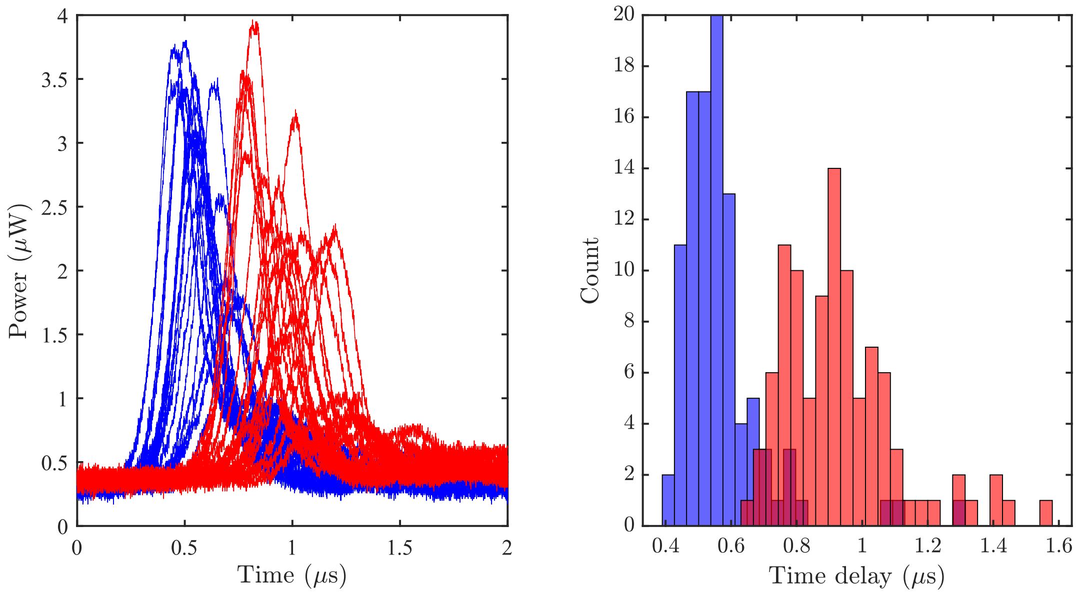

Figure 5.3: Seeding superradiant pulses (blue) versus pure atom cavity interaction (red). The time delay is significantly smaller and more consistent when the pulses are seeded. However, the lasing frequency is influenced by the seeding light.

5.2 Dependence on cavity offset

We study the behavior of the superradiant pulses by varying a key parameter, namely the cavity offset, δ_{cav}. Changing the cavity offset can change the strength of the effective atom-cavity coupling, allowing for a transition between different pulse regimes. Figure 5.4 shows a set of pulses with varying δ_{cav}. Each horizontal line is a superradiant pulse, and the pulses are aligned with their maximum intensity at $t = 0$. Figure 5.5 plots pulses for three different cavity offsets. If the cavity is on resonance, we observe an immediate and strong pulse where seemingly most of the atoms are deexcited, but a small bump in the trail of the main pulse indicates some reabsorption and emission from the intracavity field generate by the main pulse. Recalling chapter 2.5.2, the frequency of this exchange of excitations is Ω_N, and it depends on $\sqrt{N}$, the number of intracavity atoms. In the regime where $\kappa > \Omega_N$, we expect that the shape of the pulses to be that of a hyperbolic secant [48], but this we only observe when producing pulses with very low atom numbers. Our large collective coupling means that $\Omega_N > \kappa$, such that we observe power oscillations due to Ω_N before the cavity field can decay.

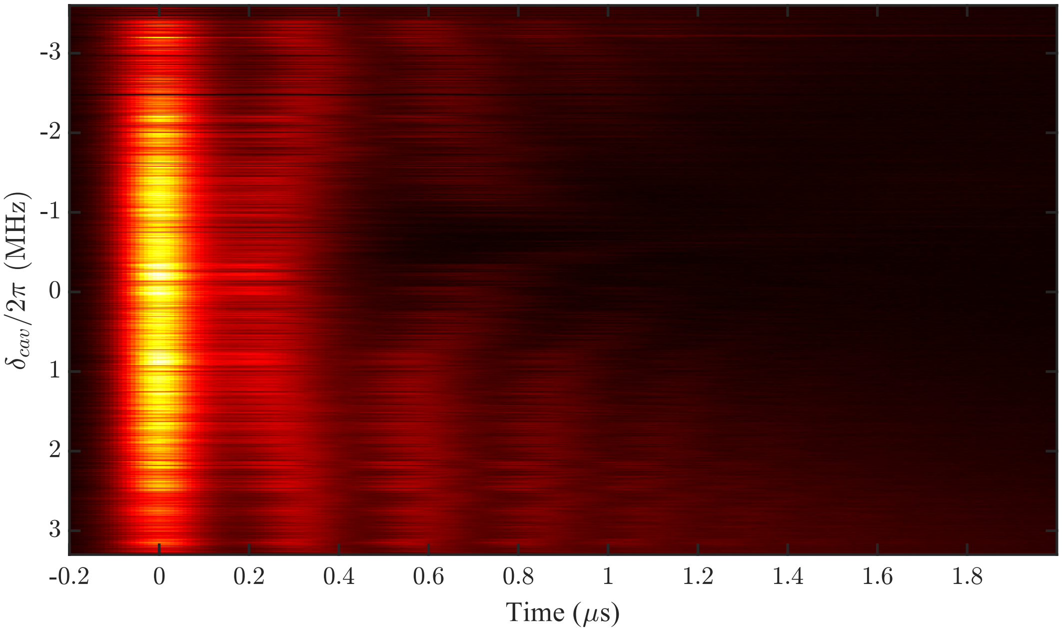

Figure 5.4: Superradiant pulse power as a function of time and cavity offset, δ_{cav}. Each horizontal slice is a pulse, and the pulsed are aligned with their peak powers at $t = 0$. For higher cavity detunings the peak power of the pulses decreases, but we observe longer lasting oscillations in the output power at a frequency presumed to be Ω_N. The peak power is ≈ 10 µW with $\delta_{\text{cav}} \approx 0$.

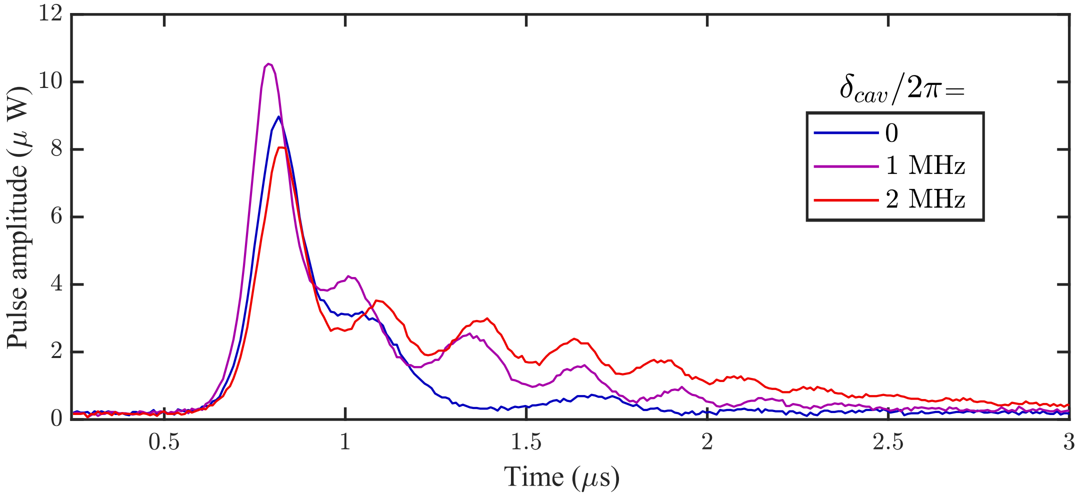

Figure 5.5: Superradiant pulse power for three different cavity offsets, δ_{cav}.

On Fig. 5.4 we observe lower peak pulse powers but longer lasting oscillations in the pulses as the cavity detuning is increased. At higher cavity detunings, the atoms are less likely to synchronize and emit into the cavity mode. Instead, a large fraction of the atoms hold onto their excitations which can support the formation of ”after pulses” as the atoms synchronise to the strong intracavity field generated by the initial pulse. From Fig. 5.5 we estimate $\Omega_N = 2\pi \cdot (3.9 \pm 0.1)$ MHz. Using the equations outlined in section 2.5.2, this suggests that we have $\Omega_N^2/(2g_0) = 11.5e6 \pm 0.5e6$ intracavity atoms. This is again a little lower than the atom number suggested by absorption imaging ($\approx 20e6$), but it matches the factor ≈ 2 in difference also found when Ω_N was determined in frequency space using the NMS.

5.3 Beat signals of the superradiant pulses

We assess the frequency stability of our superradiant pulses using a beat against our stable reference laser. Within a single MOT realization, we can produce 30-50 pulses at a repetition rate of 10 kHz without introducing additional cooling in between the pulses. Repeated pumping of the cloud does however increase the temperature (Fig. 5.6), and introduce a systematic Doppler shift of the pump beam - and we shall see the impact of this when the superradiant pulses are used for a Ramsey interferometer readout. Before we produce the train of pulses, we conduct an NMS sweep such that the intracavity atom number can be compared between MOT realizations. Figure 5.7 shows a spectrogram of 10 pulses

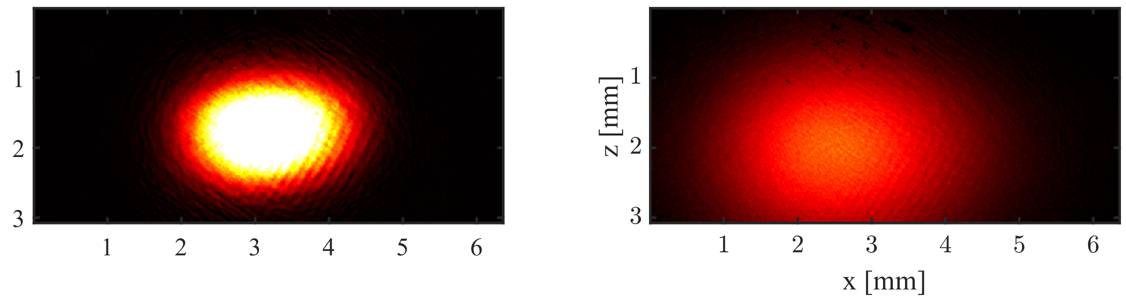

Figure 5.6: Absorption images of the atomic cloud 25 ms after release without producing pulses (left) and with 10 pulses (right).

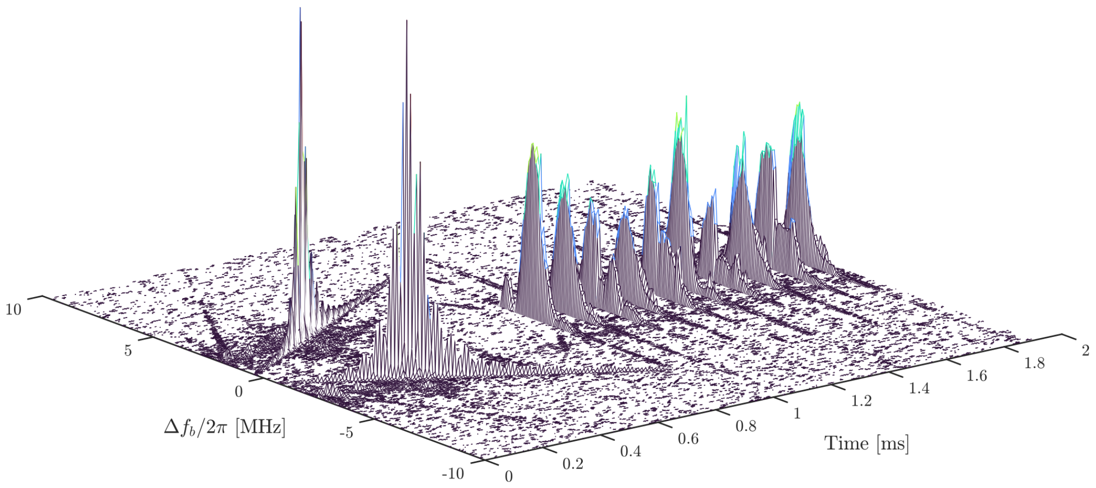

Figure 5.7: A spectrogram of an NMS sweep we the subsequent generation of 10 superradiant pulses.

preceeded by an NMS sweep. Δf_b is deviation from the mean beat frequency. The NMS sweep and the generation of 10 pulses is done in just 2 ms.

We study the spectrum of the single superradiant pulses. On the left plot in Fig. 5.8 the spectrum of four pulses are shown. The frequency features are much wider than the natural linewidth of the transition, $\gamma = 2\pi \cdot 7.5$ kHz, which is a result of the collectively enhanced emission, that lowers the lifetime in the excited state and increases the linewidth of the emitted light. To achieve below natural linewidth superradiant light, we must have phase information stored in the atoms for a time longer than τ, the lifetime of the excited state - which is inherently not possible without repumping and continuous synchronization of atoms.

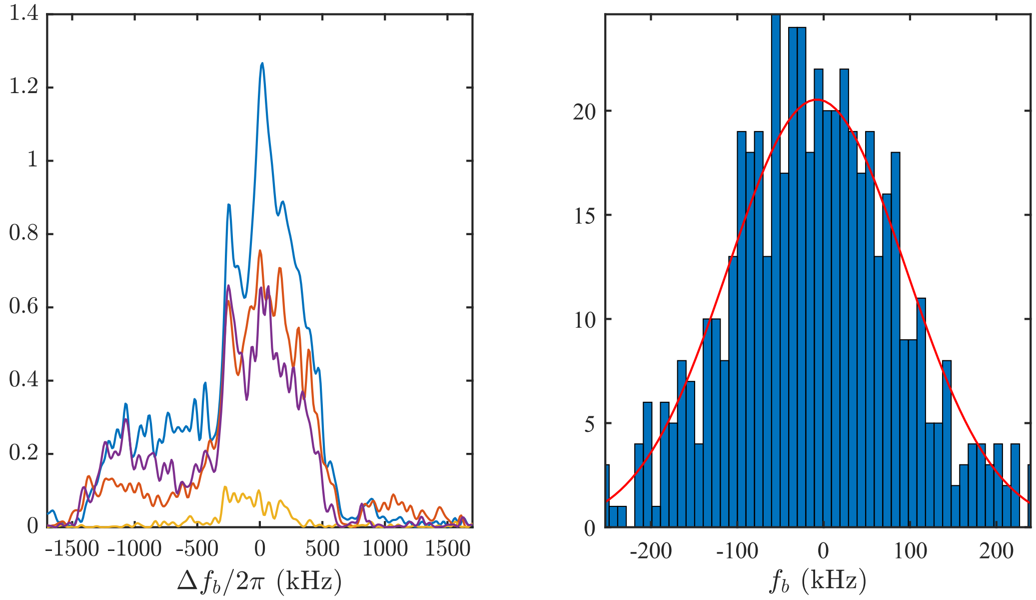

Figure 5.8: Histogram of superradiant pulse center frequencies. The Gaussian distribution has a width $\sigma = 102$ kHz

In Fig. 5.8, the plot on the right, we assess the stability of the center frequency of the pulses. Using 535 pulses separated by 1.3 seconds, we find that the center frequencies follows a Gaussian distribution with a standard deviation $\sigma = 102$ kHz, with an uncertainty on the mean value $\sigma_\mu/\sqrt{n} = 4.4$ kHz.

CHAPTER

6

Continuous lasing in the bad cavity regime

In the previous chapter we described the superradiant bursts that our system can produce when we subject the atoms to a single population inversion pulse. In the bad cavity regime, the frequency of such laser pulses have suppressed sensitivity to cavity mirror vibrations, which is an essential selling point for superradiant lasers. So far, most studies investigating the frequency properties of superradiant emission used single population inversion pulses on the respective lasing transition to gauge the frequency characteristics of superradiant light [45, 92, 102], where [103] reached a Fourier limited linewidth of order 10 Hz on the mHz linewidth $^1S_0 \rightarrow {}^3P_0$ transition in ^{87}Sr. These pulses are strong in intensity due to the enhanced collective emission, but the power is emitted much faster than the atoms would naturally decay without the coupling to the cavity. In[103] the achieved linewidth is actually ≈ 10000 times larger than the natural linewidth. This is an inherent feature of superradiant pulses; the collectively enhanced emission of the atom-cavity system produces pulses with a shorter duration than the natural lifetime of the respective transition. This results in Fourier limited spectral features of the emitted light, which complicates studying the proposed benefits of using an active lasing schemes a frequency reference without actually building a fully continuous superradiant laser.

In the frequency analyses of superradiant pulses, one way to circumvent the Fourier limitation is to concatenate multiple short pulses, but this adds noise at the repetition frequency of the lasing. Moreover, these single population inversion pulses do not operate in a steady state regime, and as such are not a true indicator of how a true active lasing scheme would behave. In order to demonstrate the potentially narrow linewidth features of superradiant emission, one have to extend the emission. This was achieved in the seminal work [104], where lasing on the $^1S_0 \to {}^3P_1$ in ^{88}Sr was extended to several hundreds of µs, many times longer than the natural lifetime of the transition. Using 150 µs subsamples of multiple pulses and recentering the PSD of each, an average power spectral density depicted an average lineshape with a smaller width than the natural linewidth of the lasing transition (an indicated linewidth of 6.0 kHz from a Lorentzian fit). Norcia et. al uses $N = 36000$ atoms caught in a deep intracavity optical lattice, with a single atom cavity cooperativity of $C_0 = 0.41$.

In our experiment we use the same approach as [104] to extend the duration of superradiant pulses. We opt to use the relativity broad 7.5 kHz for a stronger atom cavity coupling. The demands of an interrogation laser addressing this transition are lower than one adressing the mHz line in ^{87}Sr, and the lasing time in our system is still ultimately limited by the time it takes the atoms to fall out of the cavity due to gravity. By repumping around the excited lasing state, $^3P_1, m = 0$ we can improve the lasing duration by several orders of magnitude as compared to the simple population inversion pulses. The science cavity in our experiment has a single atom cooperativity of $C_0 = 4.5e - 4$ which allows for a very low fundamental linewidth to the lasing [49] if the lasing duration is sufficiently extended. We routinely cool and trap $N \approx 40e6$ atoms at $T = 2$ µK in the optical cavity, but we can sustain lasing with much less atoms. This gives us some flexibility when choosing lasing gain parameters in order to achieve steady state lasing, which turns out to be essential in our efforts to emulate the behavior of a truly continuous superradiant laser. The work described in this chapter is also described in our publication [1].

6.1 The repumping scheme

After the initial preparation and cooling described in chapter 4 we turn on two additional repumpers, the 689 repumper to the $^3P_1, m_j = -1$ Zeeman state and the 688 nm repumper that drives transitions between $^3P_1$ and $^3S_1$. We leave on the 679 and 707 nm repumper on throughout the experimental sequence, and all repumpers are coaligned with an incidence angle perpendicular to the cavity axis. The polarization of the 689 nm repumper is oriented perpendicular to the magnetic field axis such that can only drive the transition to the $m_j = \pm 1$ magnetic sublevels. The 688 nm repumper polarization is parallel to the magnetic

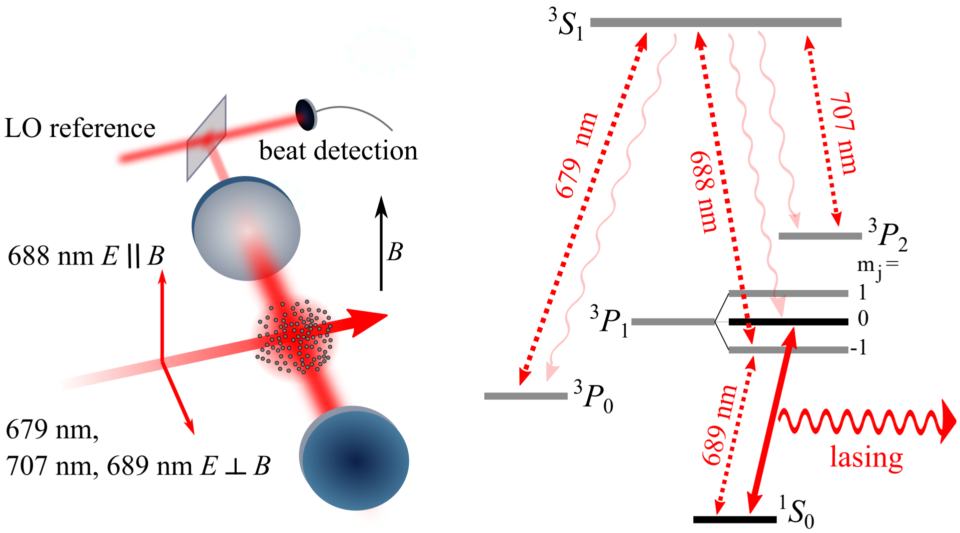

Figure 6.1: Continuous repumping scheme. Figure partly adapted from [1].

to avoid depopulating the upper lasing level $m_j = 0$. This scheme is depicted in Fig.6.1. Turning on the two additional repumpers creates population inversion on the $^1S_0 \rightarrow {}^3P_1$ transition which initiates the lasing. It is important that the atoms reach the upper lasing level $^3P_1, m = 0$ via spontaneous decay from $^3S_1$. If the atoms are repumped directly to the upper lasing level, the phase of the repump lasers would be imprinted on the lasing transition. Because the superradiant lasers operate in the bad cavity regime, the result is that the emission frequency is tied to the frequency of the repump lasers.

From numerical simulations we estimate that each atom on average absorbs 9 repumping photons and spontaneously emits 8 before reaching the upper lasing level. The majority of these photons are absorbed to depopulate the $^3P_2$ state. Thus, we expect the temperature of the atomic ensemble to increase significantly during the lasing process. When all repumpers are operating at saturation intensity, the lasing scheme can be described as a 3-level system, as all pumping and decay rates in the system are $\gg \gamma_l$. Essentially, the intermediate states in the pumping schemes can be viewed as a combined third level in the lasing system. In a 3-level laser, at least half of the population atoms must be excited to achieve population inversion [76], as the decay from the third level is much faster than the decay of the lasing state. To sustain such a population of atoms in the excited state requires a significant amount of repumping photons, which results in deflection and heating of the atomic cloud [105].

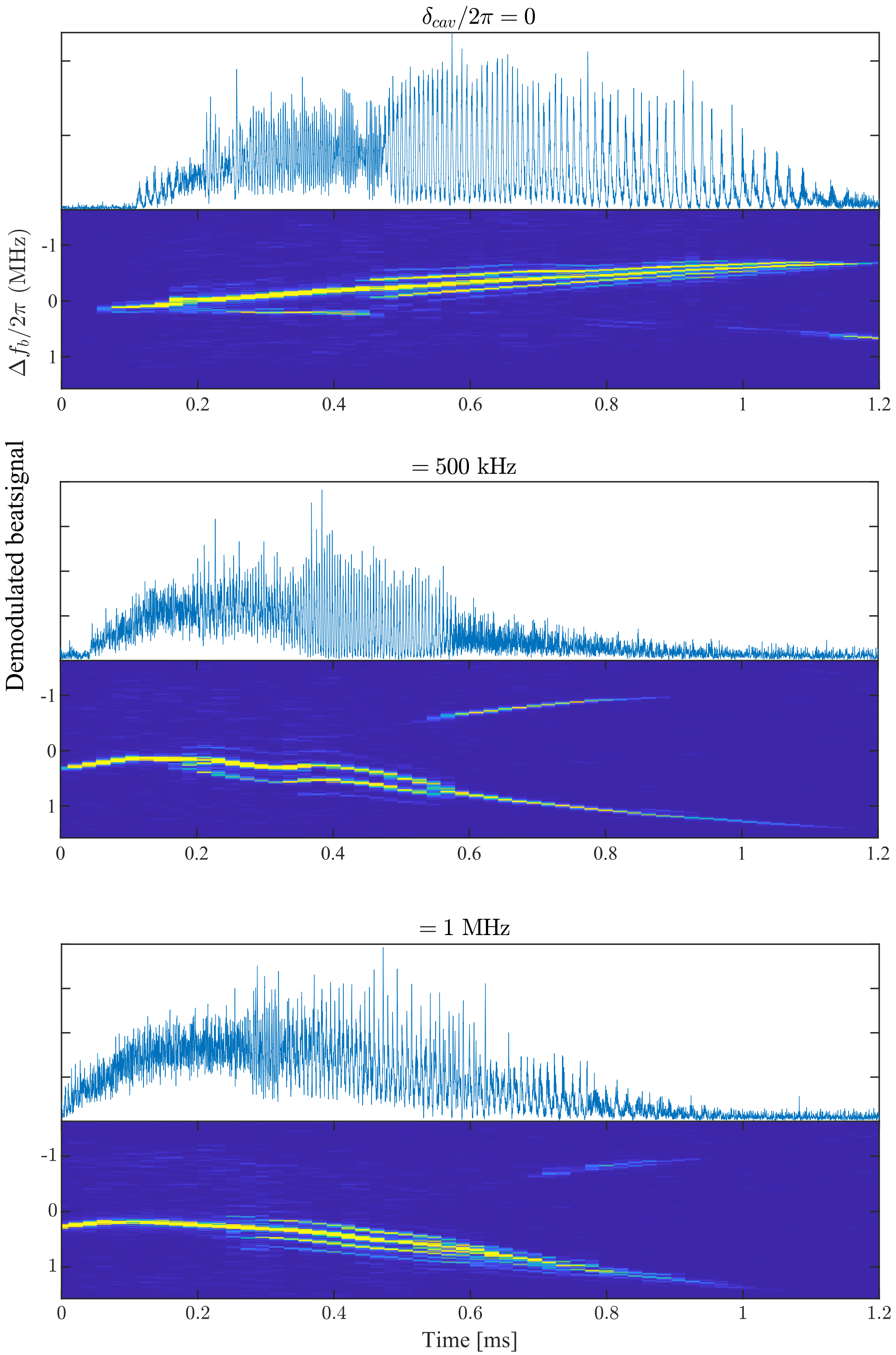

Figure 6.2: Bi-stable continuously repumped superradiant pulses for different cavity offsets.

6.2 Initial results and bi-stable behavior

Before diving into narrow linewidth superradiant lasing, we will briefly discuss some interesting initial observations with the repumped superradiant pulses. While the current iteration of the experiment has all repumpers coaligned, the initial setup producing repumped superradiant pulses had the 679 and 707 nm repumpers pumping the atoms incident from an orthogonal angle to the cavity axis, while the 689 and 688 nm repumper was at a 45° angle. The 679 and 707 nm repumpers were incident on the atom cloud from below in an effort to prolong the time the atoms spend in the cavity by counteracting gravity. The bias field separating the magnetic sublevels of $^3P_1$ was realized by ramping one of the magnetic coils after the cooling sequence to create an magnetic imbalance in the anti-Helmholtz configuration. This allowed us to produce very intense yet unstable continuous superradiant pulses of much longer duration than the pulses we see from a simple population inversion pumping pulse. Three pulses with different cavity offsets δ_{cav} are plotted in Fig. 6.2. In the bottom of each panel we plot a spectrogram of the beat note between the superradiant pulse and our stable reference laser, while the top of the panel shows the down mixed superradiant pulse output power. The spectrograms are calculated using a fast Fourier transform (FFT) algorithm in MATLAB with overlapping 40 µs square windows every 20 µs. We define Δf_b to be the deviation from the average beat frequency during lasing. Over the course of a pulse of length ≈ 1 ms, the frequency of the lasing can drift up to a MHz. This large drift is likely the result of a frequency bifurcation induced by repumping the atoms along the cavity axis as predicted in [106], where the condition $k_c v_x \tau < \pi$ must be satisfied to achieve steady state superradiant lasing (where k_c is the wave vector of the intracavity field, v_x is the average ensemble velocity along the cavity axis, and τ is the transit time of the atoms through the cavity waist). When the k-vector of the repumpers have a projection unto the cavity axis, we will gradually increase v_x until $k_c v_x \tau > \pi$ and we transition into the bistable regime. One of the bifurcations can be emphasized by changing the cavity detuning δ_{cav} as evident in Fig. 6.2. However, other factors contribute to the instability of the lasing frequency. Besides the obvious bifurcation of the lasing frequency on the scale of MHz, we also observe heavy amplitude modulation that be observed in the time domain and frequency domain. Figure 6.3 shows more pulses in the bi-stable regime for $\delta_{\text{cav}} = 0$. The deflection of the MOT cloud due to repumping photon kicks changes the cavity coupling over time. Moreover, since the repumpers are oriented perpendicular to each other, the light pressure from one repumper moves the atom cloud across the intensity

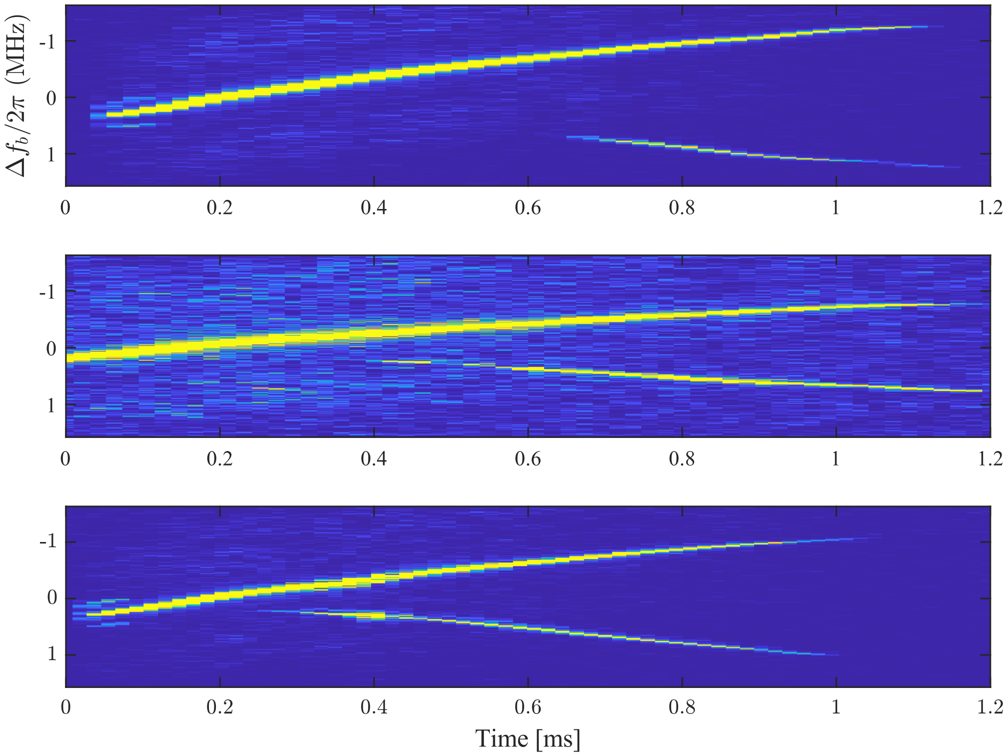

Figure 6.3: Bi-stable continuously repumped superradiant pulses for $\delta_{cav} = 0$.

profile of the other. This creates time-dependent repumping rates, which can cause the pulses to transition between operating in two different regimes; a quasi-steady state regime with almost constant power, and an oscillating regime where the output power is heavily amplitude modulated. The movement across the intensity profile of the repumpers also results in an unavoidable time-dependent light shift of the ground state by the 689 nm repumper.

6.3 Improvements and gain control

The observation of the bistable regime continuous pulses is an interesting experimental observation relevant for future realizations of continuous superradiant lasers. However, to experimentally demonstrate narrow linewidth superradiant lasing we need to stay in the regime where $k_c v_x \tau < \pi$, which requires us to rethink our repumping scheme. We want to apply repumping only perpendicular to the cavity axis, eliminating the systematic Doppler

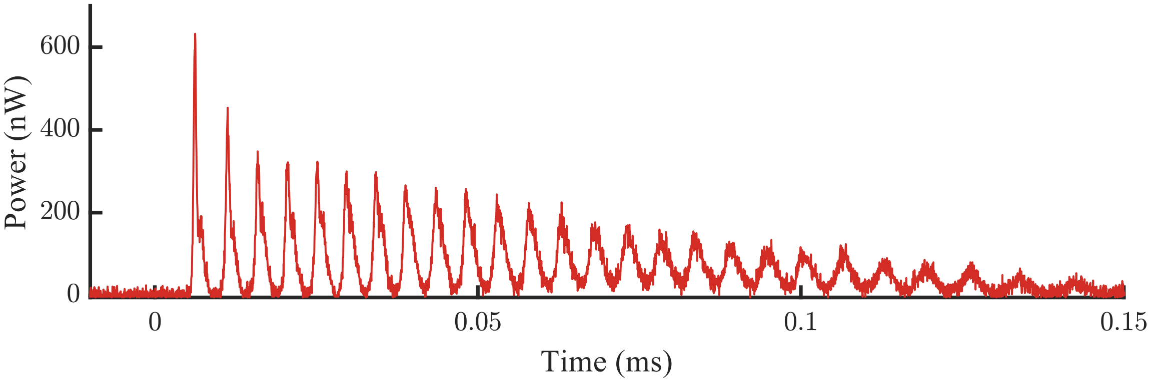

Figure 6.4: Continuously repumped pulse. The output power is heavily oscillating due to a high pumping power.

shift along the cavity axis. This should prevent us from transitioning into the bistable regime by limiting the velocity of the atoms along the cavity axis during repumping. It is equally important to manage and homogenize the light shifts from the repumpers, such that there is no time-dependent frequency shift of the lasing frequency. This we achieve by overlapping all the repumpers and launching them at the atoms from an angle perpendicular to cavity axis, as depicted in Fig. 6.1. The final improvement that we implemented was to wind bias coils to apply a homogeneous magnetic field during repumping. This is crucial in order to avoid time-dependent repumping rates and light shifts caused by the Doppler shift of the 689 nm repumper laser frequency.

With these improvements in place, and with all the repumpers tuned to their respective resonances by maximizing the deflection of the atomic cloud after turning on each repumper, we start to see lasing in the cavity that exhibits different behavior than previously observed. An example of such a pulse is depicted in Fig. 6.4. The repumping produces something that resembles a train of pulses, but it is actually a continuous signal with heavy amplitude modulation. These pulses we refer to as in the oscillating regime. We pose that this behavior is due to a high repumping rate that produces a population inversion on a time scale much smaller than τ, the natural lifetime of ${}^3P_1$. This in turn results in a high collectively enhanced emission rate, Ω_N, that momentarily exceeds the pumping rate out of the ground state. We can limit these oscillations by turning down the atom number (lowering Ω_N), but this ultimately results in a much lower power output and shorter pulses. The high repumping rate results in a larger deflection of the atomic cloud, limiting the time the atoms spend in the cavity. Moreover, each atom can only absorb a certain number of photons before being Doppler shifted off resonance with the 689 nm repumper. In an effective 3-level system like this, half of the atoms are in the excited state at all time when lasing. This means that repumping recoils are wasted on atoms just to sustain population inversion, as a large majority of the excited state atoms are ”cancelled out” by the ground state atoms. In effect, we gain much shorter pulses with unstable power output.

6.3.1 Transitioning to a 4-level scheme

As such, we wish to tweak the lasing scheme to transform it from an effective 3-level system to a 4-level system. In a 4-level lasing scheme lasing can be sustained using just a fraction of the total number of atoms in the excited state, which provides more stable lasing dynamics and allows us to use the available gain over a longer period of time.

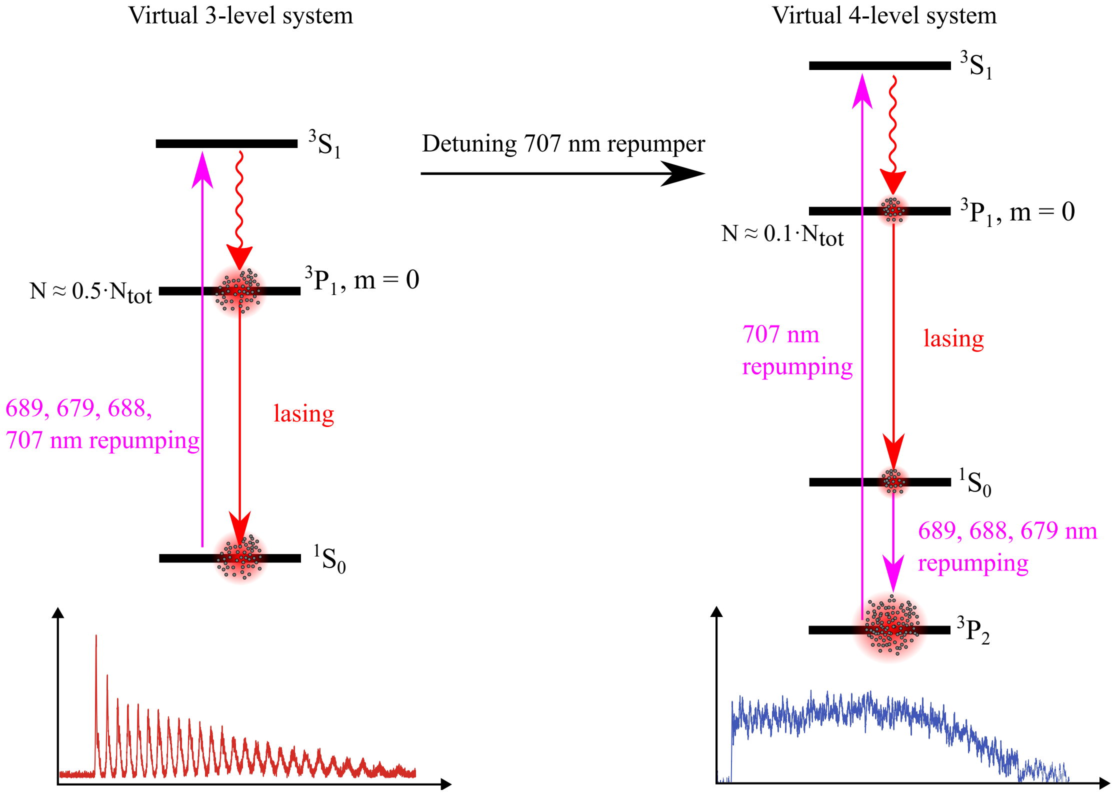

Figure 6.5: Transition between 3-level and 4-level virtual lasing system. In the 3-level system, all atoms are either in the ground or excited state. The pulse power is highly oscillatory. In the 4-level system the majority of the atoms are shelved in the metastable $^3P_2$ state, which results in stable lasing dynamics.

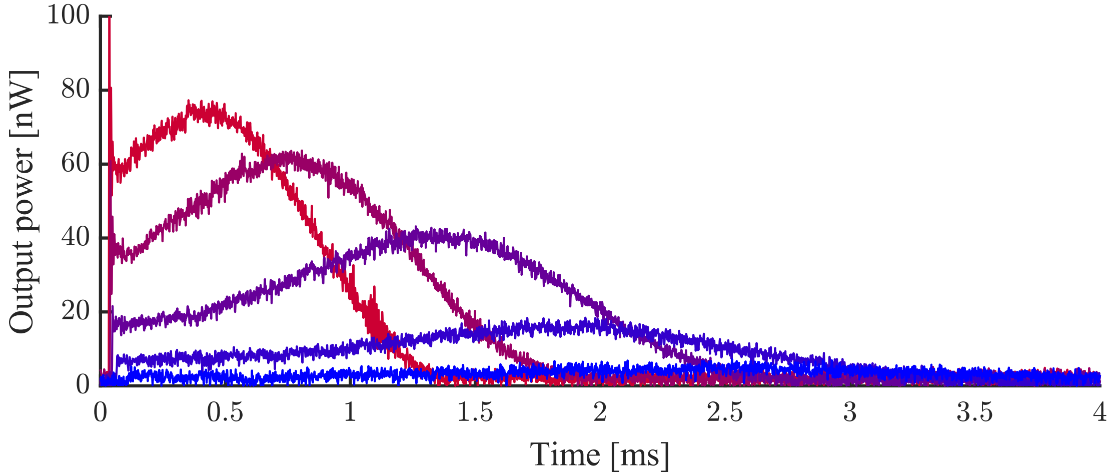

Figure 6.6: Tuning the 707 nm laser to shelve atoms in $^3P_2$ during lasing. From red to blue, the 707 nm laser detuning to atomic resonance is shifted from -10 to -60 MHz. The pulses produced with large detuning on the 707 nm repumper are more stable in power.

We add an effective level to repumping scheme by detuning the 707 nm repumper such that each atom now are shelved for hundreds of µs in $^3P_2$ when repumping. This means that the atoms are no longer directly repumped out of $^3P_1, m = -1$ into $^3P_1, m = 0$ on time scales much shorter than τ, which we use to break the ensemble state coherence in the repumping process. In other words, we can more quickly establish a steady state population of atoms in each of the relevant repumping levels. We depict our interpretation of two such lasing level schemes in Fig. 6.5.

In the virtual 3-level system, the atoms are almost instantaneously brought from the ground state to the excited state through $^3S_1$. However, the 4-level lasing scheme decouples the population of the ground and excited state, and it requires less pumping power to sustain population inversion. This helps us manage lights shifts and lower the deflection of the atomic cloud. We use $^3P_2$ for shelving atoms, as the atoms are 5 times more likely to decay into this state than $^3P_0$ [64]. Figure 6.6 shows how tuning the frequency of the 707 nm laser modifies the pulse dynamics by shelving atoms in $^3P_2$. The 707 nm laser operates with $I \approx I_{\text{sat}}$. From red to blue, the 707 nm detuning $\delta_{707}/2\pi$ is changed in increments of 10 MHz, from 20 MHz to 60 MHz below atomic resonance. At the onset of the pulse we see power oscillations, but these quickly die out in favor of a more steady state behavior. Detuning the 707 nm laser to 60 MHz, we can achieve pulses with a relatively stable power output for a duration of around 4 ms, which is an order of magnitude longer than in the oscillating regime. This regime is what we refer to as the steady state regime of lasing.

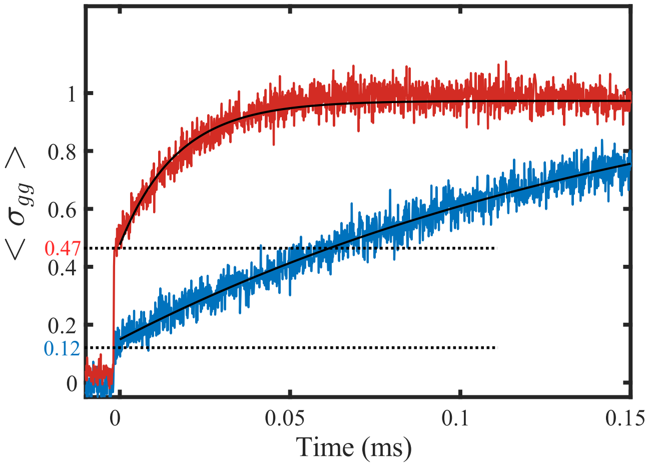

Figure 6.7: Measuring blue fluorescence from the atoms immediately after 100 µs of lasing in the steady state (blue) and oscillating (red) regime. The step at the onset of the fluorescence measurement gives an indication of the number of atoms in the ground state during lasing. Notably, the lasing in the oscillating regime has close to half the atoms in the ground state, which is consistent with behavior of a 3-level laser. The steady state pulse has $\approx 12\%$ of the atomic population in the ground state.

In Fig. 6.7 the repumping rates of the oscillatory and steady state regimes are quantified. We apply all of the repumper lasers for 100 µs, and end the superradiant emission by turning off 689 nm repump laser. We measure the fluorescence to determine the proportion of atoms that returns to the ground state, $\langle\sigma_{gg}\rangle$, as a function of time after the lasing has ceased. In red, (high repumping rate, oscillatory regime), $\delta_{707} = 0$. In blue (low repumping rate, steady state regime), $\delta_{707}/2\pi = 60$ MHz.

In the oscillatory regime, we find a characteristic decay time of $\tau = 20.4(4)$ µs for atoms to return to the ground state. This is consistent with the natural decay rate of ${}^3P_1$, and it means that almost all atoms are in the ground and excited state during lasing. This is also evident from the step in the fluorescence observed at the onset off the measurement, which indicates that $\approx 47\%$ of atoms are in the ground state immediately after the lasing ceases. We expect this behavior from a 3-level laser, where the atom population are almost equally split between the ground and excited state during lasing. For the steady state regime the time constant is $\tau = 190(19)$ µs, and the step at the onset of the measurement indicates that a much smaller fraction of atoms (about $\approx 12\%$) are in the ground state during lasing. This behavior is expected from an effective 4-level lasing scheme, where population inversion can be sustained with just a fraction of the total ensemble.

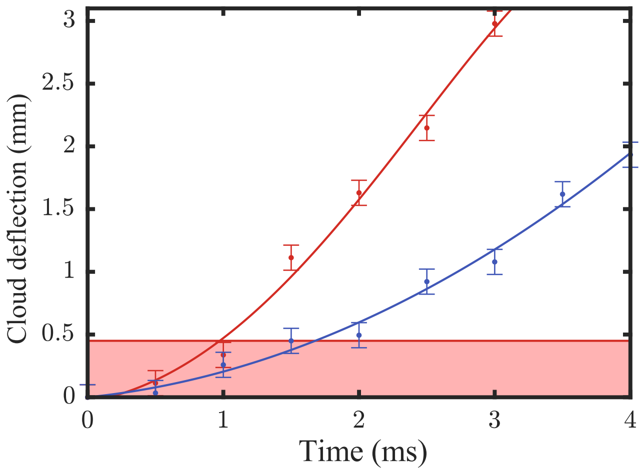

Figure 6.8: In-situ physical deflection of the atomic cloud while repumping in the steady state (blue) and oscillating (red) lasing regime.

The physical deflection of the atomic ensemble due to repumping is shown in Fig. 6.8. We measure the position of the atomic cloud by taking absorption images at variable times after turning on the repumpers at $t = 0$. The blue and red data points corresponds to the same repumping regimes (oscillating and steady state output power) as shown in Fig. 6.7. The red shaded area indicates the cavity waist radius. In the steady state regime, the reduced repumping rate leads to a decrease in physical deflection of the atomic cloud, which prolongs the interaction with the cavity. The lasing ceases when the atom cloud moves outside the cavity waist, and the collective coupling falls below the lasing threshold. After repumping for 3 ms, the speed of the atom cloud is $\approx$ 1m/s. This creates a Doppler shift of $v/\lambda \approx 1.45$ MHz for the 689 nm repumper (but not for the emitted lasing, as we are repumping perpendicular to the cavity). This is high compared to the 7.5 kHz natural linewidth of the transition. However, the ${}^1S_0 \rightarrow {}^3P_1 \rightarrow {}^3S_1$ transition should be treated as a two-photon interaction where the combined Rabi frequency is the product of the two single photon Rabi frequencies, and the strength decreases as $1/\Delta$ [89].

In the oscillatory pulse regime, the large acceleration quickly results in a large enough Doppler shift to bring the repumping rate below the lasing threshold, causing the lasing to terminate even before the atom cloud leaves the cavity waist.

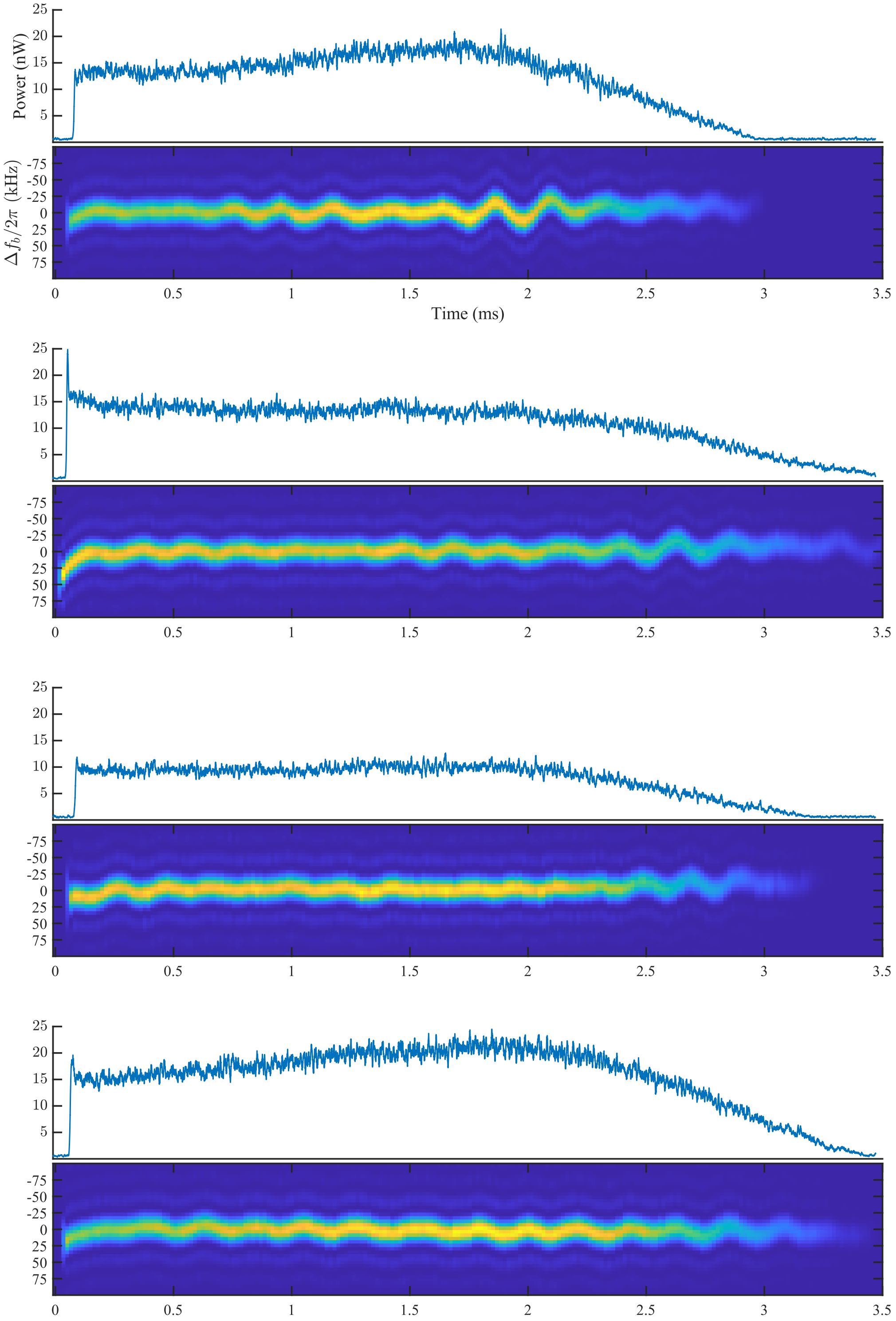

Figure 6.9: Four continuously repumped pulses and their calculated spectrograms in the steady state regime. The frequency experiences a notably shift in the beginning of the pulse. The $3-5$ kHz oscillations in the spectrum is caused by an inadequate cavity lock.

6.4 Beat experiments

We investigate the frequency stability on the pulses in the steady state regime by beating the cavity output light with our stable reference laser. Figure 6.9 shows the calculated spectrograms of four pulses with similar parameters. The spectrograms are again calculated using a fast Fourier transform (FFT) algorithm in MATLAB, and use overlapping 60 µs square windows every 30 µs to assess the instantaneous frequency. Each square signal window has been zero padded to interpolate the spectrum of each time bin to a finer resolution. This does not change the measurables in the spectra, but it can make it easier for the human eye to perceive the patterns. The center frequency of the beat note $f_b = 2\pi \cdot 43.148$ MHz is subtracted such that we instead plot the deviation Δf_b. We observe that the lasing frequency has a systematic drift at the onset of the pulse, but stabilizes after $200 - 300$ µs. The frequency is now stable on the kHz level compared to the MHz frequency drifts of the bi-stable pulses (Figs. 6.2 and 6.3). The biggest contribution to the frequency noise is $3 - 5$ kHz oscillation of the center frequency visible in all the spectrograms plotted in Fig. 6.9. This noise originates from cavity piezo resonances that we have not been able to suppress yet.

6.4.1 Cavity pulling

Next, we address a key prediction of bad cavity lasing. Namely, the insensitivity to cavity fluctuations. The so-called cavity pulling factor c_p is indicative of whether the lasing frequency of the system ω_l is mostly governed by the atomic or cavity resonance,

$$\omega_l = c_p \cdot \omega_{\text{cav}} + (1 - c_p) \cdot \omega_a, \tag{6.4.1}$$

and it can be defined as the derivative $c_p = \delta\omega_l / \delta_{\text{cav}}$. The lasing is said to be in the bad cavity regime, where the lasing is dictated by the atomic resonance, if $c_p < 0.5$. For a $c_p = 0$, the lasing frequency ω_l is unaffected by any changes to the cavity resonance. Worth noting, it is also possible to determine c_p using the derivative involving the atomic resonance. Essentially, if the atomic resonance frequency is modulated with a well known strength, one can measure how well the lasing frequency follows. In the case of $c_p = 0$, the lasing frequency will follow the shifted atomic resonance perfectly. This is also a reminder of the importance to control the external factors shifting the atomic energy levels when building a superradiant laser.

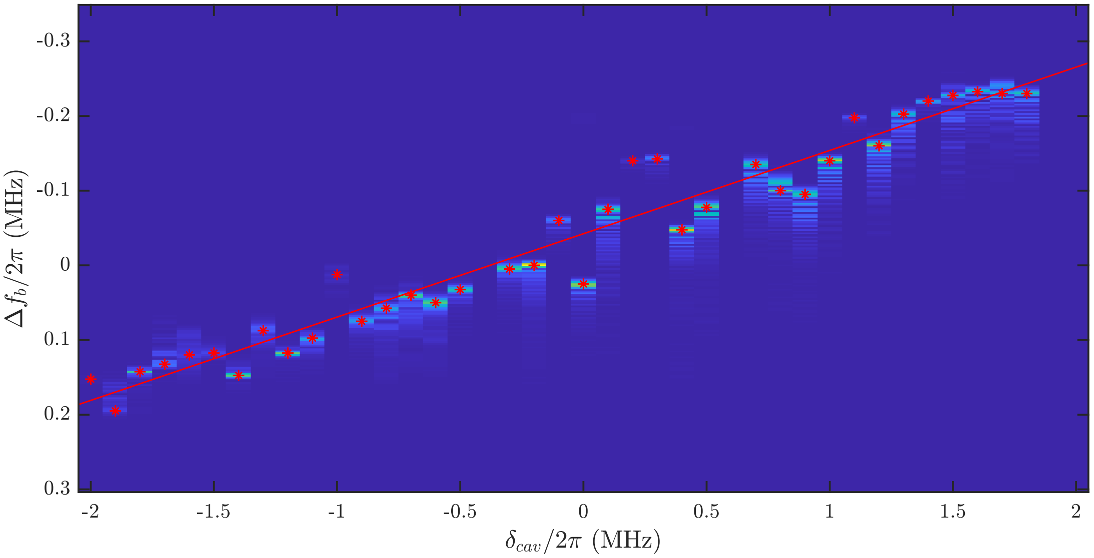

Figure 6.10: Spectra of continuously repumped pulses as a function of cavity offset, δ_{cav}. Each vertical slice is the Fourier transform of a superradiant pulse with a specific cavity offset. The y-axis is the deviation from the mean beat frequency, which is linearly proportional to lasing frequency. The red stars marks the most intense frequency components for each pulse, and we use these points to fit a straight line to extract the cavity pulling parameter $c_p = 0.111 \pm 0.005$.

We test our continuously repumped superradiant pulses to determine which regime our lasing operates in. We produce many pulses using different cavity offsets δ_{cav} and beat them against our reference laser. The beat signals are Fourier transformed to extract their frequency content. Figure 6.10 shows the spectra of pulses created with cavity offsets varying from -2 to 2 MHz. Each vertical slice is the Fourier transform of a continuously repumped pulse, and the y-axis is the deviation from the mean frequency and it is proportional to the lasing frequency ω_l. The red stars marks the strongest frequency component for each pulse (and associated δ_{cav}), and we fit a straight line to obtain a cavity pulling coefficient $c_p = 0.111 \pm 0.005$ for this set of pulses. This is well within the bad cavity regime. Theoretically we expect the cavity pulling to depend on the Doppler broadening δ_D and the cavity linewidth κ [46, 51],

$$c_p(t) = 2\gamma_{\text{Dopp}}/(2\gamma_{\text{Dopp}} + \kappa). \tag{6.4.2}$$

Using $\gamma_{\text{Dopp}}/2\pi = 40$ kHz and $\kappa/2\pi = 800$ kHz we get $c_p = 0.09$, which is reasonably close to our measurement. Though, this approach is inherently an incomplete description of

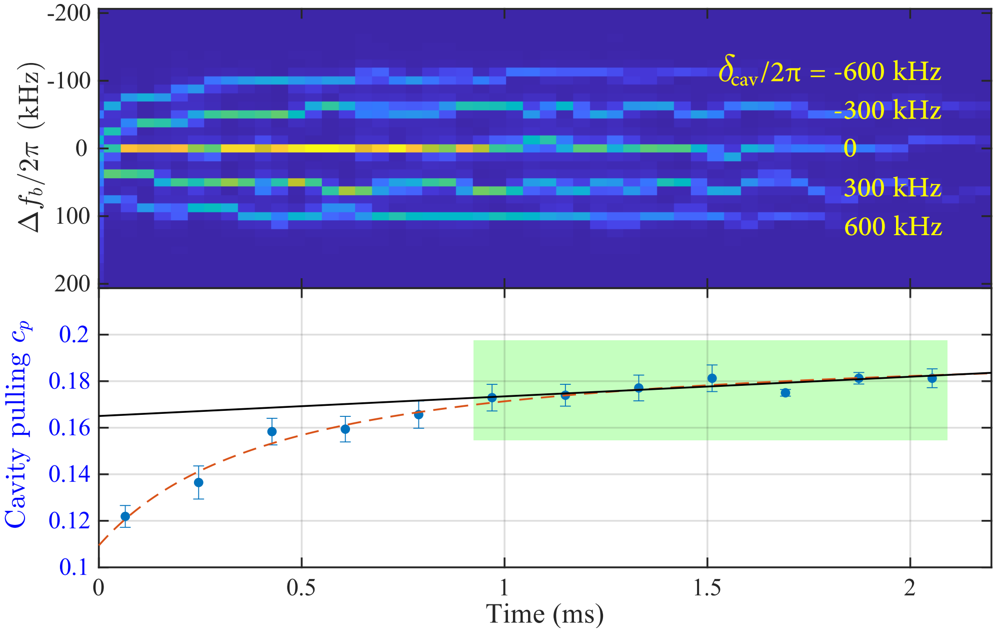

Figure 6.11: Combined spectrogram of five pulses with different cavity detunings, $\delta_{cav}/2\pi$, from -600 kHz to 600 kHz in steps of 300 kHz. The bottom plot shows the calculated cavity pulling coefficient, $c_p(t)$. We observe a region (green rectangle) where $\Delta c_p(t) = 0.008(3)$ for $\Delta t = 1$ ms (black solid line fit)

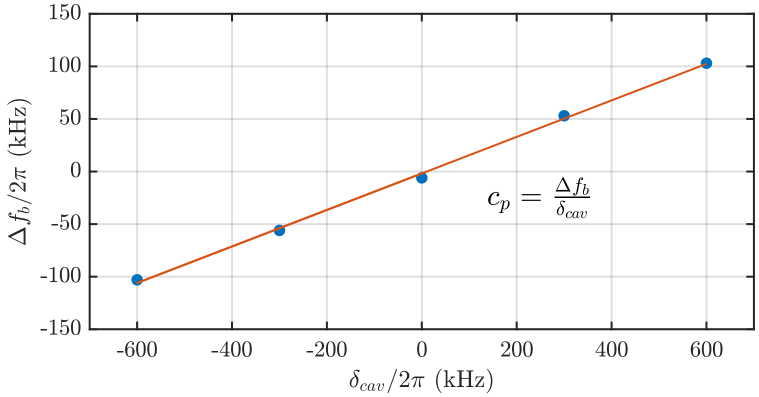

Figure 6.12: Using the most intense frequency for each time bin in Fig. 6.11, we find the time-dependent c_p from the slope of a straight line fit between the cavity offset and the lasing frequency.

the pulse dynamics, as the continuous repumping increases the temperature throughout the pulse, which in turn makes the cavity pulling increase over time. We address this by producing another set of pulses in the steady state regime with identical parameters except varying the cavity offset. We ensure that the slight change in collective coupling due to the changing cavity offset does not modify the pulse behavior significantly. Figure 6.11 shows a spectrogram that combines five pulses with different cavity offsets. Using the same technique as in Fig. 6.10, we find the most intense frequency component for each of the five pulses for each time bin in the spectrogram. For various times c_p is calculated using a straight line fit between the most intense frequency components as shown in Fig. 6.12. With this, we can construct time-dependent cavity pulling coefficient, $c_p(t)$ (bottom part of Fig. 6.11).

We observe that $c_p(t)$ increases quickly at the onset of the pulse. We approximate this behavior by a converging exponential function (dashed red). This increase in cavity pulling is most likely due to a rapid increase in temperature of the ensemble (recalling the influence that just 10 recoil photons had on the red MOT in Fig. 5.6). We also speculate that the atoms initially contributing to the lasing has suffered from significantly fewer repumping recoils just due to statistics. The cavity pulling of ≈ 0.18 towards the end of the pulse corresponds to a Doppler width of 100 kHz. However, the absolute value of the cavity pulling is not the only concern. It is desirable to have the cavity pulling vary as little as possible as a function of time, as any change in cavity pulling will cause a change in the lasing frequency unless the cavity is parked exactly at atomic resonance. In practice, we cannot expect $|\delta_{\text{cav}}|$ to be lower than 10 kHz. This means that a change in cavity pulling Δc_p of 0.1, like we see in Fig. 6.11, will lead to a frequency shift of at least 1 kHz between the start and end of the pulse. In a possible future realization of a continuous superradiant laser it is reasonable to assume that parameters such as cavity pulling will be steady state variables, but in our experiment any time dependent variables must be mitigated to emulate the behavior of such a laser. We observe a region (green rectangle) between $t = 1$ ms and $t = 2$ ms where the cavity pulling changes only with $\Delta c_p(t) = 0.008(3)$ for $\Delta t = 1$ ms (black fit), which demonstrates low first order sensitivity to the offset of the cavity locking point after the initial 1 ms of lasing.

It is worth mentioning that these measurements only probe the cavity pulling for a constant cavity offset. In the future it will be relevant to probe the frequency dependent cavity pulling - or, to measure the transfer function of the cavity fluctuations to the lasing frequency. From the errorsignal of the science cavity PDH lock we estimate that the center frequency

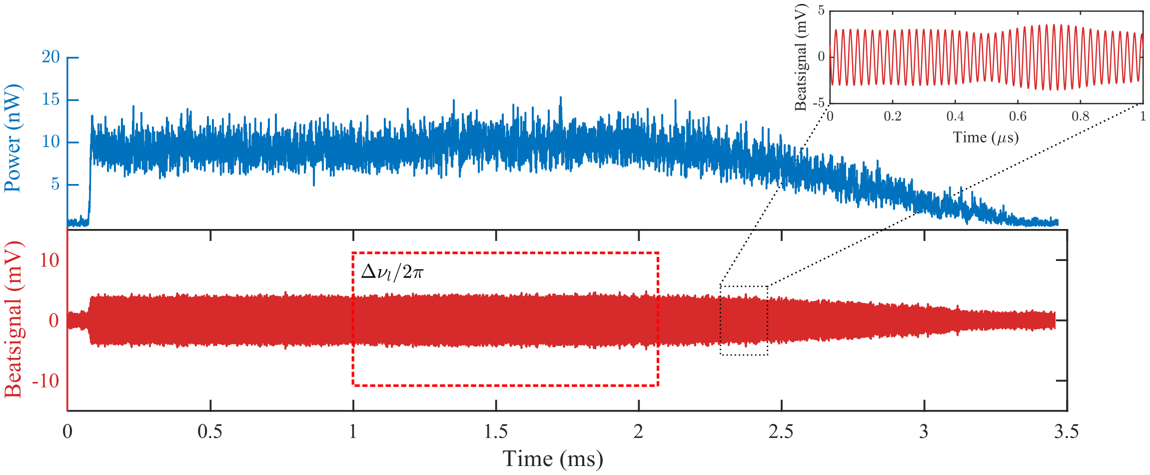

Figure 6.13: Steady state continuously repumped pulse and its raw beat signal. The red box indicates the subset of the beat signal that we use to calculate the linewidth.

of the cavity fluctuates with $50 - 80$ kHz due to several piezo resonances at $3 - 5$ kHz (the oscillations also seen in Fig. 6.9). However, the measurement of the lasing linewidth presented in the next subsection suggests that the lasing frequency is less sensitive to fluctuations in cavity length than the DC cavity pulling measurements indicates.

6.4.2 Subnatural linewidth superradiant light

We have now arrived at the culmination of this chapter - the generation of narrow linewidth superradiant light. This is the key result presented in our paper [1]. We have eliminated the time dependent light shifts and ensured that the atomic velocity is low along the cavity axis. The repumper parameters have been finely adjusted to achieve stable lasing conditions for extended periods of time. The last piece of the puzzle was the mitigation of the time-dependent cavity pulling to ensure a reduced sensitivity to locking the cavity at a slight offset compared to atomic resonance.

Figure 6.13 shows the power and the beat signal of a continuously repumped pulse. We investigate the linewidth of the beat signal between $t = 1$ ms and $t = 2.1$ ms (marked by the dashed red box), as this is where we observe the most stable lasing parameters. Figure 6.14 shows the measured linewidth of the beat note $\Delta\nu_l/2\pi$, defined as the full width at half maximum (FWHM) of the power spectral density (PSD). The top plot shows how using increasingly bigger fractions ΔT of the 1.1 ms cutout of the beat note lowers the linewidth by increasing the integration time. From [78], the Fourier limit to the linewidth of a square pulse (like our cutout of the beat note) is $\Delta\nu_{\mathrm{Fourier}}/2\pi = 0.89/\Delta T$. This limit is plotted with a yellow line alongside the measured linewidth. The natural linewidth of the lasing transition $\gamma_l/2\pi = 7.5$ kHz is indicated with a dashed blue line. If we continue integrating the beat note for longer than the box in Fig. 6.13 indicates, the measured $\Delta\nu_l$ starts to increase due to technical noise and lasing instability towards the end of the pulse. We see the lowest linewidth after an integration time of ≈ 1.1 ms, as shown in the bottom plot on Fig. 6.14. The red line is the PSD of a pure sine burst with constant amplitude at the same frequency as the lasing (to emulate the "perfect" beat note). The blue data points is the calculated PSD (again zero padded to interpolate points, which has no influence on the perceived linewidth). The agreement between the PSD of the lasing and the pure sine suggests that we are, in fact, Fourier limited. We achieve a linewidth of $\Delta\nu_l/2\pi = 820$ Hz, which is almost an order of magnitude lower than the natural linewidth of the transition - the Fourier limit is 800 Hz for 1.1 ms of integration time.

We expect the Purcell linewidth limit to be ≈ 3.3 Hz [49]. The modified Shawlow-Townes limit for a steady-state 10 nW pulse with $\gamma_{\mathrm{Dopp}}/2\pi = 100$ kHz is ≈ 0.9 Hz. To probe this limit, we would need to produce lasing pulses with a duration of 270 ms - several orders of magnitude longer than our current superradiant signals.

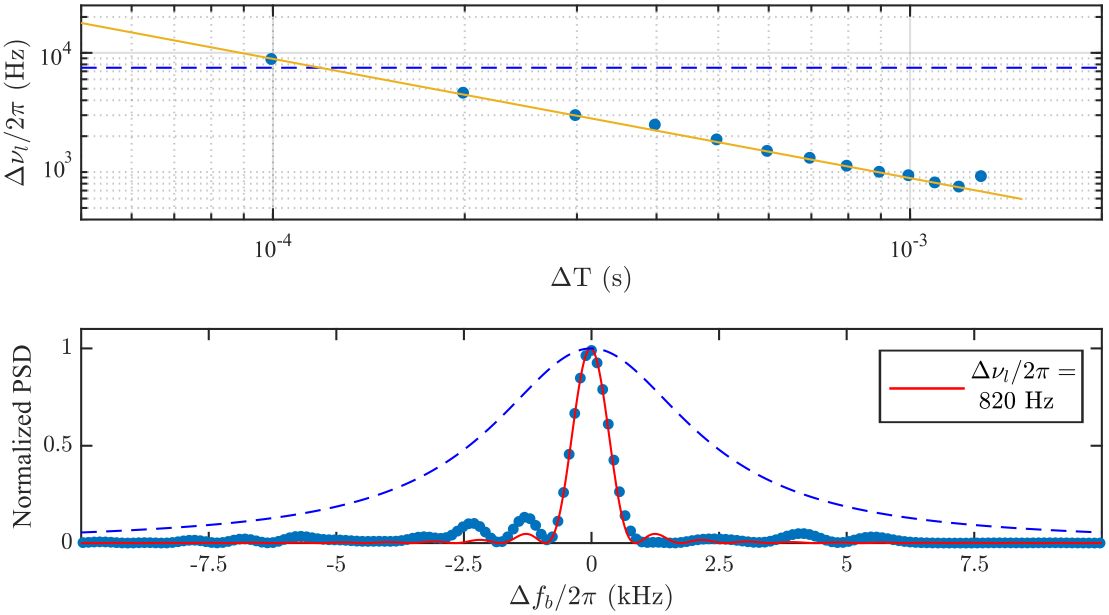

Figure 6.14: Linewidth of steady state superradiant pulse. Top plot: Blue points is the measure linewidth at an integration time ΔT. The yellow line is the Fourier limited linewidth, $\Delta\nu_{\mathrm{Fourier}}/2\pi = 0.89/\Delta T$. Bottom plot: The linewidth $\Delta\nu_l/2\pi = 820$ Hz, achieved after 1.1 ms of lasing. The blue dashed line indicates γ_l for comparison.

CHAPTER 7

Superradiant Ramsey readout spectroscopy

In an atomic clock, the long term frequency stabilization of the clock laser is usually done using a Rabi or Ramsey type [23] interrogation scheme. In a Rabi interrogation scheme, a low intensity beam is driving an ensemble of atoms between the ground and clock state for a duration τ_P, such that $\Omega_R\tau_=\pi$. If the population transfer is maximized, the laser is on resonance. The Ramsey sequence is a two $\pi/2$ pulse temporal interferometer sequence that allows the phase of an atomic superposition to evolve with respect to the phase of clock laser. Depending on the phase accumulated between the two interrogation pulses, the average population of atoms will oscillate between the ground and excited clock state. In both the Rabi and the Ramsey type interrogation methods, the readout of the atomic population translates into a frequency deviation of the clock laser. Traditionally, such atomic state readouts have been realized using fluorescence measurements. In ^{87}Sr the broad $^1S_0 \rightarrow {}^1P_1$ transition can be used to determine the number of atoms in the ground state when operating a clock on the $^1S_0 \rightarrow {}^3P_0$ transition [107, 108]. To measure the number of atoms in the excited state, a pulse of repumping light can bring the remaining atoms in $^3P_0$ back to the ground state where an additional fluorescence measurement can be performed.

The drawback of a fluorescence measurement on a broad transition is that it destroys the interrogated atom ensemble. The atoms scatter many photons in all directions to increase the quality of the signal measured by a camera or photodiode, as the camera can usually only capture a fraction of the photons scattered due to a small solid angle. This causes

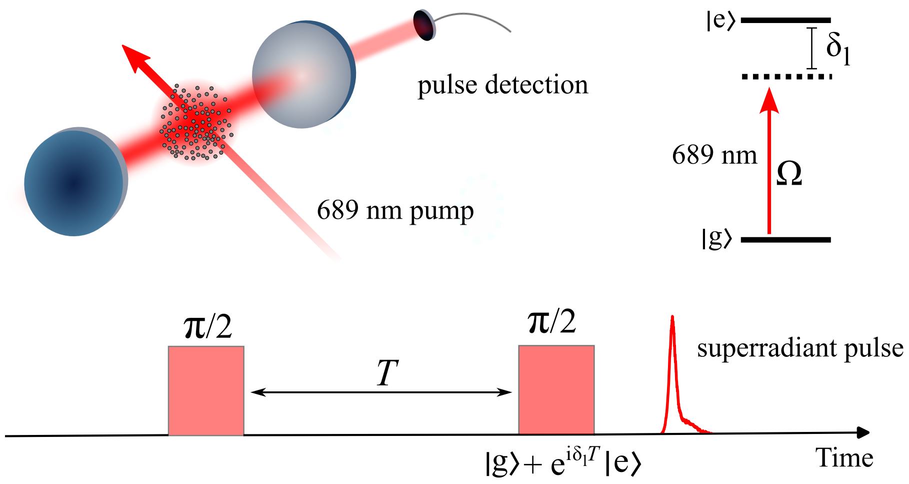

Figure 7.1: The Ramsey readout scheme. Two $\pi/2$ pulses constitute a Ramsey interferometer sequence. If there is population inversion after the Ramsey interferometer, a pulse will be emitted with an amplitude corresponding to excited state population.

significant heating and deflection of atoms, and usually a new sample of atoms needs to be caught and cooled in several MOT stages.

In our experiment we have developed an alternative way of reading out the atomic state after a Ramsey frequency interrogation sequence. Originally proposed by Christoph Hotter et. al. [3], we have realized a scheme where the amplitude of a superradiant a pulse can be used to determine the atomic state population for frequency metrology. Instead of scattering many photons and measuring the fluorescence, the readout is generated using strong collective effects in an ensemble of atoms in an optical cavity. This scheme scatters on average less than one photon per interrogation, yet yields a measurable signal as the state detection superradiant pulse is emitted along a well defined cavity axis. This means that the ensemble can be used for many interrogations in the same MOT realization. The scheme is shown in Fig. 7.2. The optical cavity is tuned to atomic resonance, and we use that $\delta_l = \omega_l - \omega_a$ as the laser detuning. Between two Ramsey interferometer pulses separated by a time T, the phase difference accumulated between the laser and the atomic superposition is $\phi_R = \delta_l T$. The second Ramsey pulse closes the interferometer and the number of atoms in the ground and excited state is determined by ϕ_R. For $\phi_R = n \cdot 2\pi$ ($n \in \{0, 1, 2, 3, 4..\}$) the excited state population is maximized, and the atom cavity system emits a strong superradiant pulse. Between the two $\pi/2$ pulses, the atoms are protected from collective emission as the lasing threshold is not exceeded.

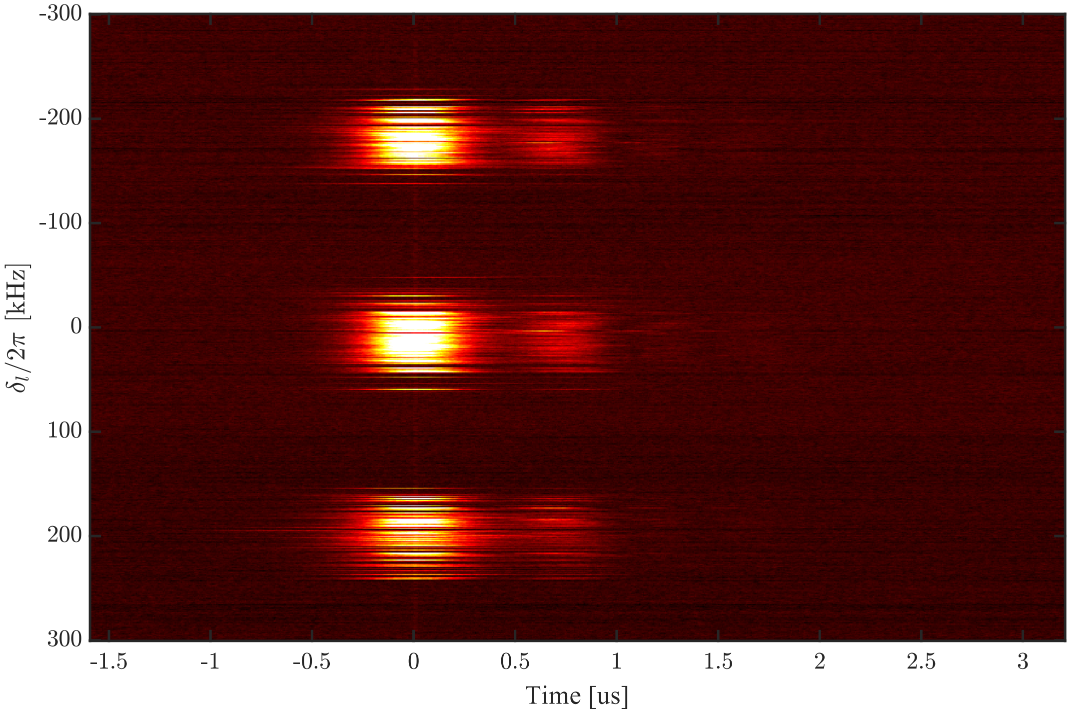

Figure 7.2: First Ramsey fringe with superradiant readout. Each horizontal slice is a superradiant pulse. The pulses are aligned with their maximum intensities.

The readout signal can be generated very fast as the collective effects can drastically enhance the emission rate into the cavity, and the scheme in principle can be applied in any quantum sensor relying on the state readout of a quantum particle. The experimental realization has resulted in the publication [2], which is under review with Nature Communication at the time of writing. For more details on this scheme, I recommend reading the upcoming thesis of my colleague Eliot Bohr which has an emphasis on this part of our experiments.

7.1 First realization

We generate the two pulses by triggering a pulse generator with two TTL pulses. The two pulses have a length of $\tau_R = 300$ ns, which corresponds to $\pi/2$ pulses for a Rabi frequency $\Omega_R = 2\pi \cdot 833\text{kHz}$. The spacing between the pulses is 5 μs. This T was chosen as a balance to resolve multiple Ramsey fringes while also retaining a reasonable amount of coherence to see contrast in the fringes. Figure 7.2 shows the first measurement of a superradiant readout Ramsey interferometer fringe. Each horizontal slice depicts the cavity output for a certain δ_l. The pulses are aligned to their maximum value. We observe strong pulses when $\phi_R = n \cdot 2\pi$, and no pulses when $\phi_R = n \cdot 2\pi + \pi$. The pulse intensity oscillates with a periodicity of $\approx 2\pi \cdot 1.4$ MHz, which is the collective Rabi frequency Ω_N. This Ω_N is lower than what we observe from the superradiant pulses produced by a π pump (as described previous chapter). This is most likely due to coherence loss in the interrogation time T which results in fewer atoms participating in the superradiant emission. The fundamental limit of the interferometer contrast is the lifetime of the excited state, $\tau = 22$ μs. After 5 μs around 20% of the atoms in the excited state have decayed. The second $\pi/2$ pulse excites half of those atoms, meaning that the maximally 95% of the atoms can be in the excited state after closing the interferometer. It also means that at least 5% of atoms will always be in the excited state even when the Ramsey pulses are perfectly out of phase with respect to the laser phase.

The contrast is also limited by the temperature of the atomic ensemble. The Doppler width of $\approx 2\pi \cdot 47$ kHz makes the atoms experience different laser detunings, and it is likely a bigger source of decoherence in the interferometer than spontaneous emission. This can be remedied by applying a π pulse halfway between the two Ramsey $\pi/2$ pulses which inverts the phase drift of the individual atoms. This rephases the inhomogenous drift at the time of the second Ramsey pulse. This technique is commonly referred to as a spin-echo pulse [109], and the implementation of such a pulse is an interesting future prospect.

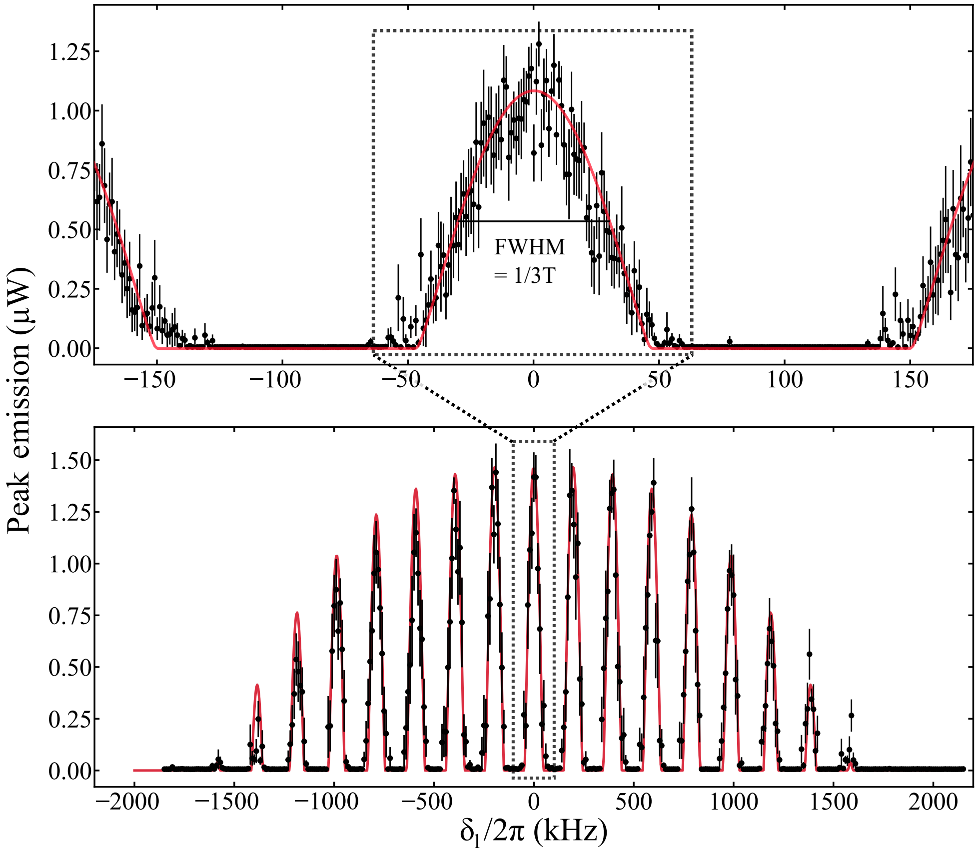

Figure 7.3: Ramsey fringe with superradiant readout. Each data point is the average of the maximum power of ten superradiant pulses.

7.2 Superradiant Ramsey readout fringes

We produce another Ramsey fringe with the same experimental parameters to study the shape of the interference fringes. We map out the entire envelope of a superradiant Ramsey fringe (Fig. 7.3). Each data point is the mean of ten measurements for different δ_l's (and for different MOT realizations). The width of the envelope is given by $1/\tau_R = 3.33$ MHz. The top plot presents a zoom in on the center fringe with a width $1/3T$ as predicted by [3]. For $|\delta_l|/2\pi > 50$ kHz the population inversion goes below threshold and no superradiant pulses are observed, the "Ramsey dead zone". We propose that the steep slope of the fringe between the maximum of the fringe and the threshold is optimal for frequency stabilization purposes.

With the superradiant Ramsey readout we do not directly get information on the interferometer contrast. Using a fluorescence readout scheme, one can observe the low values of the interference fringes to assess the contrast. We can probe the amount of atoms interfering by our ability to coherently transfer atoms from a superposition back to the ground state. However, with a superradiant Ramsey readout we only observe signal when more than 50% of atoms end up in the excited state. For an interferometer with considerable decoherence the atomic population oscillates just around 50% for varying δ_l. The shallow slope of the interference fringes results in a fuzzy superradiant threshold that is mostly dominated by noise. We can estimate the interferometer coherence (or the amount of atoms contributing to the contrast) by integrating the superradiant pulses and count photons, or we can compare the pulse heights to the superradiant pulses that we produce using π pump pulses rather than a Ramsey pulse sequence.

7.3 Repeated superradiant Ramsey interrogations

Since the atoms maximally absorb a single photon during the Ramsey interrogation, an interesting prospect of the superradiant Ramsey readout is the reusability of the atomic ensemble for multiple interferometer sequences. The top plot on Fig. 7.4 showcases our ability to produce 9 superradiant Ramsey readouts (numbered from 1 to 9) within a single MOT realization for a certain δ_l. The cloud of atoms is not influenced by any external forces and is freely falling while we pump the atoms perpendicular to gravity. We use $T = 2$ μs to increase contrast. The time between each pulse is 100 μs to make sure all atoms have returned to the ground state between consecutive Ramsey sequences. The bottom plot shows Ramsey fringes using a specific pulse number in each MOT realization, such that the first pulse of every MOT realization produces the blue fringe with the highest contrast, and the last pulse produces the red fringe with the lowest contrast. We observe that the fringes produced by the later pulses receive a significant frequency shift - the Ramsey fringe produced by using the 9th pulse has a shift of $40-50$ kHz towards a higher frequency. This is due to absorption of pump photons. We can counter this by either switching the pumping direction every other Ramsey interrogation, or we can erase the momentum by flashing the red MOT light for few ms in between Ramsey interrogation. This means that we cannot produce pulses with 100 μs spacing, but the fringes generated using pulses from the same MOT realization should have the same center frequency.

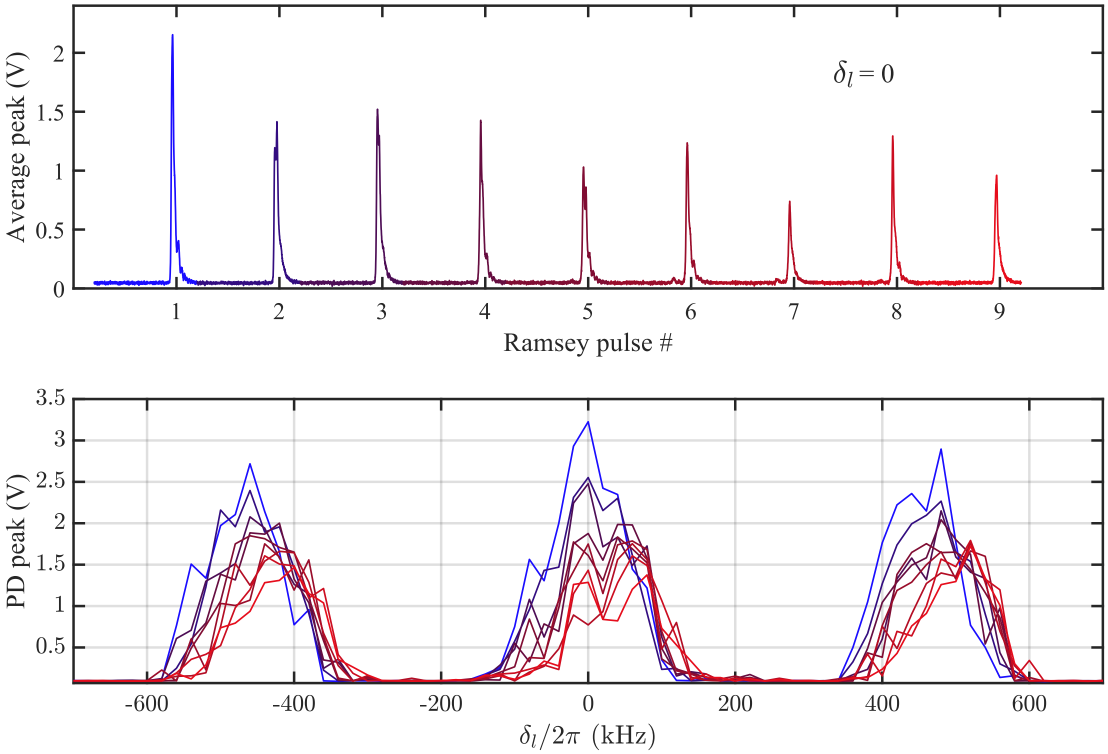

Figure 7.4: Effect of multiple Ramsey interrogations. Top plot: multiple Ramsey pulses within one MOT realization. The pulse intensities drop as the pump beam induces a Doppler shift on the cloud for every pumping pulse. Bottom plot: mapping out a Ramsey fringe using a specific pulse number. The colors correspond to the pulses in the top plot. Mapping out a Ramsey fringe with the 9th pulse results in a Ramsey fringe with a lower contrast and a systematic shift in center frequency.

In the red MOT, the atoms number has a characteristic decay time of several hundreds of ms. Instead of switching off the MOT coils before the Ramsey sequence to create a proper bias field, we leave it on. This results in lower amplitude superradiant pulses, but it allows us to recapture the atoms after a superradiant Ramsey readout. The characteristic decay time of the MOT coils would allow us to switch the red MOT magnetic fields on and off on a few ms timescale, but we are limited by our experimental control system.

We turn off the red MOT for 1 ms while we do a Ramsey interrogation, after which the MOT beams are flashed for 2 ms to remove the photon momentum from the pumping beam. We can repeat this sequence hundreds of times. Figure 7.5 shows the pulse amplitude over time when shifting the probing frequency between atomic resonance and the middle of the Ramsey dead zone, such that only every other Ramsey interrogation generates a pulse. This is to emulate a typical frequency interrogation scheme, where the frequency of the probing laser is shifted around the fringe to probe the center frequency. Each datapoint is an average of pulses generated in 5 different MOT realizations (with 100 pulse repetitions in each). The background of ≈ 50 mV is the cavity locking light. The pulse intensity reduces by $10 - 15$ over 100 recapture cycles. For now, the biggest limitation of this interrogation scheme is the inconsistent pulse amplitudes for similar laser detunings. We attribute this to superradiant pulse statistics and decoherence of the atomic ensemble, but it is subject to further investigation.

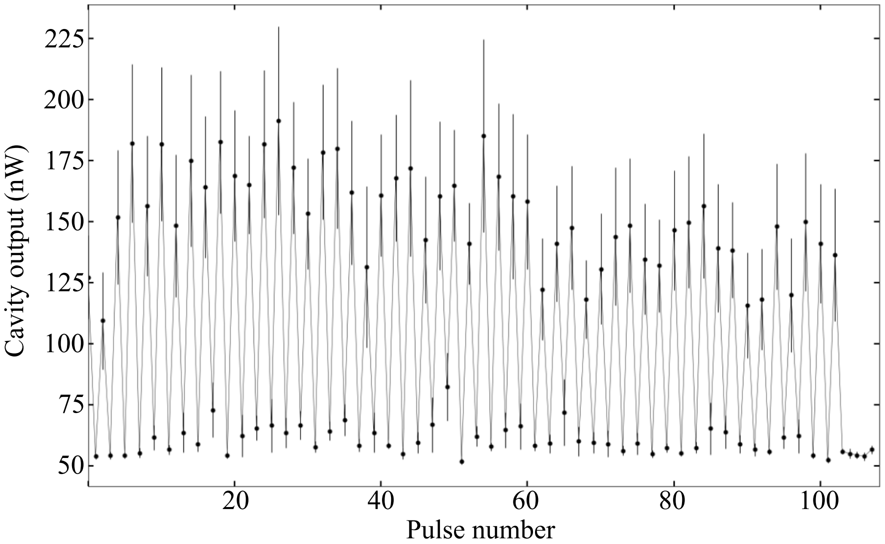

Figure 7.5: Repeated Ramsey interrogations with cooling in between. This allows us to Ramsey pulses with the same center frequency, as the cooling removes the recoil from the pump beam. The pulses are generated with 2 ms spacing in time. Every other pulse is stepped in frequency to emulate an interrogation of the center frequency of the fringe.

CHAPTER

8

Conclusion and outlook

The first part of this thesis describes the development of an experimental setup to produce strong collective interactions in an atom cavity system. A significant part of my PhD work was dedicated to implementing and upgrading experimental hardware in the pursuit of a red MOT. One of the main challenges for generating the red MOT is the narrow linewidth of the transition and the associated low scattering force. To gather a dense cloud of atoms in a single frequency red MOT requires a narrow 689 nm laser [100], and our old reference laser did not perform as expected. While we did manage to catch some atoms in the red MOT using diode lasers injected by our old reference laser, the behavior of the red MOT seemed unusual and we could never reach the intra-cavity atoms numbers necessary to comfortably move into the strong coupling regime. Our new 689 nm reference laser solved this problem, and we can now trap more than 120 million atoms and cool them to 2 µK. We verify our transition into the strong coupling regime $\Omega_N \gg \kappa, \gamma$ by resolving the NMS.

The most significant result presented in this thesis is the generation of narrow linewidth continuously repumped superradiant lasing at technologically relevant powers. We put our efforts into homogenizing atomic shifts and control lasing parameters, which allowed us to produce narrow linewidth superradiant pulses with a duration of 3-4 ms. The seminal work in [104] managed to reach a Lorentzian linewidth of 6.0 ± 0.3 kHz on the same lasing transition. This was achieved using the frequency centered average of multiple 150 µs beat note samples. Building upon their lasing scheme, we have managed to observe a lasing linewidth almost an order of magnitude lower than the natural linewidth using just a single pulse. Stable lasing parameters and the mitigation of time-dependent light shifts allow us to use a longer signal sample to push the Fourier limit much below the natural linewidth. An interesting future application of the narrow linewidth pulses is to probe the proposed theoretical fundamental limit of our system $\delta\nu_p = C\gamma \approx 3.3$ Hz [49]. To push the Fourier limit below $\delta\nu_p$ we need to extend the lasing to > 270 ms, which is two order of magnitudes longer than our current pulses. To achieve such lasing durations we need to implement schemes to continuously cool and/or trap the atoms while they are lasing. Currently, our lasing duration is limited by the atoms simply falling out of the cavity mode. Moreover, the performance of the science cavity lock needs to be improved if the lasing is not be limited by technical noise. While every continuously repumped superradiant pulse we generate in our current setup shows sub-natural linewidth features, the reproducibility of each pulse is limited by technical noise of the system.

In [1] we proposed to run a MOT using $^3P_2$ as the ground state [110–112] while the atoms are lasing on the $^1S_0 \rightarrow {}^3P_1$ transition. We have already determined that the atoms spend $\approx 80\%$ of their lasing cycle in $^3P_2$ (in the steady state regime), which leaves plenty of time to remove the repumping recoils. It is also likely that introducing a lattice in the science cavity would give us enough integration time to probe the Purcell limit. However, if the cooperativity was increased or a different transition was used, the Purcell limit could be in a regime where it makes sense to probe with our 3-4 ms pulses. As an example, lasing on the $^3P_1 \rightarrow {}^3S_1$ transition with a linewidth of 4.3 MHz would put the Purcell limit at 1.8 kHz. Of course, this would require rethinking the repumping scheme.

Other possible directions for the experiment includes converting the experiment into a truly continuous machine. One such idea is to use a continuous 461 nm and 497 nm 2D horizontal MOT beam configuration centered just above the cavity axis. The vertical MOT beam is missing, such that atoms diffuse through the cavity axis after leaving the 2D MOT. Simulations have shown that such a scheme is likely to generate a high enough intra-cavity atom number to exceed the lasing threshold. Alternatively, it might be possible to realize lasing while running a blue MOT continuously. It has been suggested that continuous narrowband lasing can be generated using two coherently driven transitions in a V-level atom [113, 114], such as the 461 nm and 689 nm transition in strontium. Lasing in a V-level system has been already been observed using ytterbium [115] which shares physical properties with strontium. However, the mechanism behind this lasing is different than suggested by the V-level proposals and the linewidth would likely be high.

The second part of the experimental results concerns the realization of a superradiance enhanced readout scheme of a Ramsey interferometer sequence, based of the proposal of [3]. The readout is fast and scatters much fewer photons than traditional fluorescence readout method. To apply this scheme for a consistent a accurate atomic readout, the statistics governing the fluctuating pulse amplitude needs to be understood; it is possible that seeding the pulses with resonant intra-cavity light can decrease the variation in shot to shot amplitude. The frequency of the pulse will be influenced by the seeding light, but in this scheme we are only interested in the pulse amplitude and not its frequency contents. However, if such fluctuations are understood and reduced, the superradiant readout could be implemented in a number of quantum sensors carrying information in the atomic state population inversion. In an atomic clock, the state of an ensemble of atoms after a Rabi or Ramsey type interrogation could be determined using a designated readout cavity, which generates a collectively enhanced and directional readout.

Currently, the work on the experiment is geared towards investigating different lasing mechanisms present in our system. We regularly observe lasing when we apply just the 689 nm repumper to ${}^3P_1, m_j = \pm 1$. This lasing will show up if the 688 nm repumper frequency is not on resonance, and it was a nuisance when we had yet to observe the first proper lasing signal. However, the polarization of this lasing is linear and perpendicular to the magnetic bias field (as opposed to the lasing originating from $m = 0$), and placing a polarizer at the output of the cavity can reject the unwanted lasing signal. While lasing in the strong coupling regime has been shown using just a single pumping frequency [116], the mechanism behind the lasing that we observe is not completely understood yet. Ultimately, the experiment will be used to investigate superradiance originating from the coupling of bright and dark atom-light dressed states [117].

As a final remark, I will say this. The experiments with continuously repumped superradiant lasing gives an indication of the performance that we can expect from future realizations of continuous superradiant lasers. Throughout my PhD, I have had the pleasure to work with some very talented and dedicated individuals. It will be exciting to follow the developments in the field in the coming years, as the first continuous superradiant laser is likely right around the corner!

References

[1] Sofus Laguna Kristensen et al. “Subnatural Linewidth Superradiant Lasing with Cold ^{88}Sr Atoms”. In: *Phys. Rev. Lett.* 130 (22 May 2023), p. 223402. DOI: `10.1103/PhysRevLett.130.223402`. URL: `https://link.aps.org/doi/10.1103/PhysRevLett.130.223402`.

[2] Eliot Bohr et al. *Collectively enhanced Ramsey readout by cavity sub- to superradiant transition.* 2023. arXiv: `2306.12544 [quant-ph]`.

[3] Christoph Hotter, Laurin Ostermann, and Helmut Ritsch. “Cavity sub- and superradiance for transversely driven atomic ensembles”. In: *Phys. Rev. Res.* 5 (1 Jan. 2023), p. 013056. DOI: `10.1103/PhysRevResearch.5.013056`. URL: `https://link.aps.org/doi/10.1103/PhysRevResearch.5.013056`.

[4] Sofus L. Kristensen et al. “Raman transitions driven by phase-modulated light in a cavity atom interferometer”. In: *Phys. Rev. A* 103 (2 Feb. 2021), p. 023715. DOI: `10.1103/PhysRevA.103.023715`. URL: `https://link.aps.org/doi/10.1103/PhysRevA.103.023715`.

[5] Sofus Laguna Kristensen. “Interferometri med ultrakolde atomer”. English. In: 31 (2020), pp. 16–19. ISSN: 0905-8893. URL: `https://www.ucnbib.dk/da/search/ting/48171478%7C870971`.

[6] Victoria Xu et al. “Probing gravity by holding atoms for 20 seconds”. In: *Science* 366.6466 (2019), pp. 745–749. DOI: `10.1126/science.aay6428`. eprint: `https://www.science.org/doi/pdf/10.1126/science.aay6428`. URL: `https://www.science.org/doi/abs/10.1126/science.aay6428`.

[7] Hidetoshi Katori et al. “Magneto-Optical Trapping and Cooling of Strontium Atoms down to the Photon Recoil Temperature”. In: *Phys. Rev. Lett.* 82 (6 Feb. 1999), pp. 1116–1119. DOI: `10.1103/PhysRevLett.82.1116`. URL: `https://link.aps.org/doi/10.1103/PhysRevLett.82.1116`.

[8] C. L. Degen, F. Reinhard, and P. Cappellaro. “Quantum sensing”. In: *Rev. Mod. Phys.* 89 (3 July 2017), p. 035002. DOI: `10.1103/RevModPhys.89.035002`. URL: `https://link.aps.org/doi/10.1103/RevModPhys.89.035002`.

[9] Helmut Ritsch et al. “Cold atoms in cavity-generated dynamical optical potentials”. In: *Rev. Mod. Phys.* 85 (2 Apr. 2013), pp. 553–601. DOI: `10.1103/RevModPhys.85.553`. URL: `https://link.aps.org/doi/10.1103/RevModPhys.85.553`.

[10] Luca Pezzè et al. “Quantum metrology with nonclassical states of atomic ensembles”. In: *Rev. Mod. Phys.* 90 (3 Sept. 2018), p. 035005. DOI: `10.1103/RevModPhys.90.035005`. URL: `https://link.aps.org/doi/10.1103/RevModPhys.90.035005`.

[11] David DeMille, John M. Doyle, and Alexander O. Sushkov. “Probing the frontiers of particle physics with tabletop-scale experiments”. In: *Science* 357.6355 (2017), pp. 990–994. DOI: `10.1126/science.aal3003`. eprint: `https://www.science.org/doi/pdf/10.1126/science.aal3003`. URL: `https://www.science.org/doi/abs/10.1126/science.aal3003`.

[12] Richard H. Parker et al. “Measurement of the fine-structure constant as a test of the Standard Model”. In: *Science* 360.6385 (2018), pp. 191–195. DOI: `10.1126/science.aap7706`. eprint: `https://www.science.org/doi/pdf/10.1126/science.aap7706`. URL: `https://www.science.org/doi/abs/10.1126/science.aap7706`.

[13] G. Rosi et al. “Precision measurement of the Newtonian gravitational constant using cold atoms”. In: *Nature* 510.7506 (June 2014), pp. 518–521. DOI: `10.1038/nature13433`. URL: `https://doi.org/10.1038%5C%2Fnature13433`.

[14] G. Lamporesi et al. “Determination of the Newtonian Gravitational Constant Using Atom Interferometry”. In: *Phys. Rev. Lett.* 100 (5 Feb. 2008), p. 050801. DOI: `10.1103/PhysRevLett.100.050801`. URL: `https://link.aps.org/doi/10.1103/PhysRevLett.100.050801`.

[15] V. Andreev et al. “Improved limit on the electric dipole moment of the electron”. In: *Nature* 562.7727 (Oct. 2018), pp. 355–360. DOI: `10.1038/s41586-018-0599-8`. URL: `https://doi.org/10.1038/s41586-018-0599-8`.

[16] C. W. Chou et al. “Optical Clocks and Relativity”. In: *Science* 329.5999 (2010), pp. 1630–1633. DOI: `10.1126/science.1192720`. eprint: `https://www.science.org/doi/pdf/10.1126/science.1192720`. URL: `https://www.science.org/doi/abs/10.1126/science.1192720`.

[17] Yousef Abou El-Neaj et al. “AEDGE: Atomic Experiment for Dark Matter and Gravity Exploration in Space”. In: *EPJ Quantum Technology* 7.1 (Mar. 2020). DOI: `10.1140/epjqt/s40507-020-0080-0`. URL: `https://doi.org/10.1140%5C%2Fepjqt%5C%2Fs40507-020-0080-0`.

[18] P. Hamilton et al. “Atom-interferometry constraints on dark energy”. In: *Science* 349.6250 (2015), pp. 849–851. DOI: `10.1126/science.aaa8883`. eprint: `https://www.science.org/doi/pdf/10.1126/science.aaa8883`. URL: `https://www.science.org/doi/abs/10.1126/science.aaa8883`.

[19] R. Blatt and C. F. Roos. “Quantum simulations with trapped ions”. In: *Nature Physics* 8.4 (Apr. 2012), pp. 277–284. ISSN: 1745-2481. DOI: `10.1038/nphys2252`. URL: `https://doi.org/10.1038/nphys2252`.

[20] J. I. Cirac and P. Zoller. “Quantum Computations with Cold Trapped Ions”. In: *Phys. Rev. Lett.* 74 (20 May 1995), pp. 4091–4094. DOI: `10.1103/PhysRevLett.74.4091`. URL: `https://link.aps.org/doi/10.1103/PhysRevLett.74.4091`.

[21] Jun Ye and Theresa W. Lynn. “Applications of Optical Cavities in Modern Atomic, Molecular, and Optical Physics”. In: ed. by Benjamin Bederson and Herbert Walther. Vol. 49. Advances In Atomic, Molecular, and Optical Physics. Academic Press, 2003, pp. 1–83. DOI: `https://doi.org/10.1016/S1049-250X(03)80003-4`. URL: `https://www.sciencedirect.com/science/article/pii/S1049250X03800034`.

[22] W. Heisenberg. “Über den anschaulichen Inhalt der quantentheoretischen Kinematik und Mechanik”. In: *Zeitschrift für Physik* 43.3 (Mar. 1927), pp. 172–198. ISSN: 0044-3328. DOI: `10.1007/BF01397280`. URL: `https://doi.org/10.1007/BF01397280`.

[23] Norman F. Ramsey. “A New Molecular Beam Resonance Method”. In: *Phys. Rev.* 76 (7 Oct. 1949), pp. 996–996. DOI: `10.1103/PhysRev.76.996`. URL: `https://link.aps.org/doi/10.1103/PhysRev.76.996`.

[24] Ali Al-Masoudi et al. “Noise and instability of an optical lattice clock”. In: *Phys. Rev. A* 92 (6 Dec. 2015), p. 063814. DOI: `10.1103/PhysRevA.92.063814`. URL: `https://link.aps.org/doi/10.1103/PhysRevA.92.063814`.

[25] W. F. McGrew et al. “Atomic clock performance enabling geodesy below the centimetre level”. In: *Nature* 564.7734 (Dec. 2018), pp. 87–90. ISSN: 1476-4687. DOI: `10.1038/s41586-018-0738-2`. URL: `https://doi.org/10.1038/s41586-018-0738-2`.

[26] S. L. Campbell et al. “A Fermi-degenerate three-dimensional optical lattice clock”. In: *Science* 358.6359 (2017), pp. 90–94. DOI: `10.1126/science.aam5538`. eprint: `https://www.science.org/doi/pdf/10.1126/science.aam5538`. URL: `https://www.science.org/doi/abs/10.1126/science.aam5538`.

[27] Hidetoshi Katori et al. “Ultrastable Optical Clock with Neutral Atoms in an Engineered Light Shift Trap”. In: *Phys. Rev. Lett.* 91 (17 Oct. 2003), p. 173005. DOI: `10.1103/PhysRevLett.91.173005`. URL: `https://link.aps.org/doi/10.1103/PhysRevLett.91.173005`.

[28] Masao Takamoto et al. “An optical lattice clock”. In: *Nature* 435.7040 (May 2005), pp. 321–324. ISSN: 1476-4687. DOI: `10.1038/nature03541`. URL: `https://doi.org/10.1038/nature03541`.

[29] E. Felicitas Arias et al. “The 50th Anniversary of the Atomic Second”. In: *IEEE Transactions on Ultrasonics, Ferroelectrics, and Frequency Control* 65.6 (2018), pp. 898–903. DOI: `10.1109/TUFFC.2018.2823591`.

[30] Fritz Riehle et al. "The CIPM list of recommended frequency standard values: guidelines and procedures". In: *Metrologia* 55.2 (Feb. 2018), p. 188. DOI: `10.1088/1681-7575/aaa302`. URL: `https://dx.doi.org/10.1088/1681-7575/aaa302`.

[31] Kenji Numata, Amy Kemery, and Jordan Camp. "Thermal-Noise Limit in the Frequency Stabilization of Lasers with Rigid Cavities". In: *Phys. Rev. Lett.* 93 (25 Dec. 2004), p. 250602. DOI: `10.1103/PhysRevLett.93.250602`. URL: `https://link.aps.org/doi/10.1103/PhysRevLett.93.250602`.

[32] John M. Robinson et al. "Crystalline optical cavity at 4  K with thermal-noise-limited instability and ultralow drift". In: *Optica* 6.2 (Feb. 2019), pp. 240–243. DOI: `10.1364/OPTICA.6.000240`. URL: `https://opg.optica.org/optica/abstract.cfm?URI=optica-6-2-240`.

[33] M. Schioppo et al. "Ultrastable optical clock with two cold-atom ensembles". In: *Nature Photonics* 11.1 (Jan. 2017), pp. 48–52. ISSN: 1749-4893. DOI: `10.1038/nphoton.2016.231`. URL: `https://doi.org/10.1038/nphoton.2016.231`.

[34] J. Borregaard and A. S. Sørensen. "Efficient Atomic Clocks Operated with Several Atomic Ensembles". In: *Phys. Rev. Lett.* 111 (9 Aug. 2013), p. 090802. DOI: `10.1103/PhysRevLett.111.090802`. URL: `https://link.aps.org/doi/10.1103/PhysRevLett.111.090802`.

[35] May E. Kim et al. "Improved interspecies optical clock comparisons through differential spectroscopy". In: *Nature Physics* 19.1 (Jan. 2023), pp. 25–29. ISSN: 1745-2481. DOI: `10.1038/s41567-022-01794-7`. URL: `https://doi.org/10.1038/s41567-022-01794-7`.

[36] Weidong Li et al. "Improved absolute clock stability by the joint interrogation of two atomic ensembles". In: *Phys. Rev. A* 105 (5 May 2022), p. 053116. DOI: `10.1103/PhysRevA.105.053116`. URL: `https://link.aps.org/doi/10.1103/PhysRevA.105.053116`.

[37] Richard Hobson et al. "Cavity-enhanced non-destructive detection of atoms for an optical lattice clock". In: *Opt. Express* 27.26 (Dec. 2019), pp. 37099–37110. DOI: `10.1364/OE.27.037099`. URL: `https://opg.optica.org/oe/abstract.cfm?URI=oe-27-26-37099`.

[38] G Vallet et al. "A noise-immune cavity-assisted non-destructive detection for an optical lattice clock in the quantum regime". In: *New Journal of Physics* 19.8 (Aug. 2017), p. 083002. DOI: `10.1088/1367-2630/aa7c84`. URL: `https://dx.doi.org/10.1088/1367-2630/aa7c84`.

[39] Hidetoshi Katori. "Longitudinal Ramsey spectroscopy of atoms for continuous operation of optical clocks". In: *Applied Physics Express* 14.7 (July 2021), p. 072006. DOI: `10.35848/1882-0786/ac0e16`. URL: `https://dx.doi.org/10.35848/1882-0786/ac0e16`.

[40] M. J. Martin et al. “Extreme nonlinear response of ultranarrow optical transitions in cavity QED for laser stabilization”. In: *Phys. Rev. A* 84 (6 Dec. 2011), p. 063813. DOI: `10.1103/PhysRevA.84.063813`. URL: `https://link.aps.org/doi/10.1103/PhysRevA.84.063813`.

[41] Philip G. Westergaard et al. “Observation of Motion-Dependent Nonlinear Dispersion with Narrow-Linewidth Atoms in an Optical Cavity”. In: *Phys. Rev. Lett.* 114 (9 Mar. 2015), p. 093002. DOI: `10.1103/PhysRevLett.114.093002`. URL: `https://link.aps.org/doi/10.1103/PhysRevLett.114.093002`.

[42] Bjarke T. R. Christensen et al. “Nonlinear spectroscopy of Sr atoms in an optical cavity for laser stabilization”. In: *Phys. Rev. A* 92 (5 Nov. 2015), p. 053820. DOI: `10.1103/PhysRevA.92.053820`. URL: `https://link.aps.org/doi/10.1103/PhysRevA.92.053820`.

[43] H. M. Goldenberg, D. Kleppner, and N. F. Ramsey. “Atomic Hydrogen Maser”. In: *Phys. Rev. Lett.* 5 (8 Oct. 1960), pp. 361–362. DOI: `10.1103/PhysRevLett.5.361`. URL: `https://link.aps.org/doi/10.1103/PhysRevLett.5.361`.

[44] R. H. Dicke. “Coherence in Spontaneous Radiation Processes”. In: *Phys. Rev.* 93 (1 Jan. 1954), pp. 99–110. DOI: `10.1103/PhysRev.93.99`. URL: `https://link.aps.org/doi/10.1103/PhysRev.93.99`.

[45] Stefan A. Schäffer et al. “Lasing on a narrow transition in a cold thermal strontium ensemble”. In: *Phys. Rev. A* 101 (1 Jan. 2020), p. 013819. DOI: `10.1103/PhysRevA.101.013819`. URL: `https://link.aps.org/doi/10.1103/PhysRevA.101.013819`.

[46] Justin G. Bohnet et al. “A steady-state superradiant laser with less than one intracavity photon”. In: *Nature* 484.7392 (Apr. 2012), pp. 78–81. ISSN: 1476-4687. DOI: `10.1038/nature10920`. URL: `https://doi.org/10.1038/nature10920`.

[47] M Norcia. “New Tools for Precision Measurement and Quantum Science with Narrow Linewidth Optical Transitions”. PhD thesis. CU Boulder, 2019. URL: `https://scholar.colorado.edu/concern/graduate_thesis_or_dissertations/t435gc985`.

[48] Torben Laske, Hannes Winter, and Andreas Hemmerich. “Pulse Delay Time Statistics in a Superradiant Laser with Calcium Atoms”. In: *Phys. Rev. Lett.* 123 (10 Sept. 2019), p. 103601. DOI: `10.1103/PhysRevLett.123.103601`. URL: `https://link.aps.org/doi/10.1103/PhysRevLett.123.103601`.

[49] D. Meiser et al. “Prospects for a Millihertz-Linewidth Laser”. In: *Phys. Rev. Lett.* 102 (16 Apr. 2009), p. 163601. DOI: `10.1103/PhysRevLett.102.163601`. URL: `https://link.aps.org/doi/10.1103/PhysRevLett.102.163601`.

[50] A. L. Schawlow and C. H. Townes. “Infrared and Optical Masers”. In: *Phys. Rev.* 112 (6 Dec. 1958), pp. 1940–1949. DOI: `10.1103/PhysRev.112.1940`. URL: `https://link.aps.org/doi/10.1103/PhysRev.112.1940`.

[51] S. J. M. Kuppens, M. P. van Exter, and J. P. Woerdman. "Quantum-Limited Linewidth of a Bad-Cavity Laser". In: *Phys. Rev. Lett.* 72 (24 June 1994), pp. 3815–3818. DOI: `10.1103/PhysRevLett.72.3815`. URL: `https://link.aps.org/doi/10.1103/PhysRevLett.72.3815`.

[52] Julia R. K. Cline et al. "Continuous collective strong coupling between atoms and a high finesse optical cavity". In: (2022). eprint: `arXiv:2211.00158`.

[53] Francesca Fama et al. "Towards continuous superradiance with a thermal atomic beam". In: *APS Division of Atomic, Molecular and Optical Physics Meeting Abstracts.* Vol. 2022. APS Meeting Abstracts. Orlando, Jan. 2022, H11.005. URL: `https://ui.adsabs.harvard.edu/abs/2022APS..DMPH11005F`.

[54] M. Bober et al. "Towards a Continuous Active Optical Atomic Clock With Cold Strontium Atoms". In: *2021 Joint Conference of the European Frequency and Time Forum and IEEE International Frequency Control Symposium (EFTF/IFCS).* 2021. DOI: `10.1109/EFTF/IFCS52194.2021.9604263`.

[55] Simon B. Jäger et al. "Superradiant emission of a thermal atomic beam into an optical cavity". In: *Phys. Rev. A* 104 (3 Sept. 2021), p. 033711. DOI: `10.1103/PhysRevA.104.033711`. URL: `https://link.aps.org/doi/10.1103/PhysRevA.104.033711`.

[56] Hidetoshi Katori et al. "Magneto-Optical Trapping and Cooling of Strontium Atoms down to the Photon Recoil Temperature". In: *Phys. Rev. Lett.* 82 (6 Feb. 1999), pp. 1116–1119. DOI: `10.1103/PhysRevLett.82.1116`. URL: `https://link.aps.org/doi/10.1103/PhysRevLett.82.1116`.

[57] Xinye Xu et al. "Cooling and trapping of atomic strontium". In: *J. Opt. Soc. Am. B* 20.5 (May 2003), pp. 968–976. DOI: `10.1364/JOSAB.20.000968`. URL: `https://opg.optica.org/josab/abstract.cfm?URI=josab-20-5-968`.

[58] J. E. Sansonetti and G. Nave. "Wavelengths, Transition Probabilities, and Energy Levels for the Spectrum of Neutral Strontium (SrI)". In: *Journal of Physical and Chemical Reference Data* 39.3 (Aug. 2010), p. 033103. ISSN: 0047-2689. DOI: `10.1063/1.3449176`. eprint: `https://pubs.aip.org/aip/jpr/article-pdf/doi/10.1063/1.3449176/15763928/033103\_1\_online.pdf`. URL: `https://doi.org/10.1063/1.3449176`.

[59] C.J. Foot. *Atomic Physics.* Oxford Master Series in Physics. OUP Oxford, 2005. ISBN: 9780198506959. URL: `https://books.google.dk/books?id=%5C_CoSDAAAQBAJ`.

[60] Shayne Bennetts. "1000 times closer to a continuous atom laser: Steady-state strontium with unity phase-space density". PhD thesis. 2019. URL: `http://www.strontiumbec.com/StrontiumLab/Theses/Shayne_Bennetts_PhD_thesis.pdf`.

[61] Mikkel Tang. "Superradiant Lasers Based on Strontium-88". Available at `https://nbi.ku.dk/english/theses/phd-theses/mikkel-tang/Mikkel-tang.pdf`. PhD thesis. Niels Bohr Institute, Nov. 2022.

[62] Masami Yasuda and Hidetoshi Katori. “Lifetime Measurement of the $^3P_2$ Metastable State of Strontium Atoms”. In: *Phys. Rev. Lett.* 92 (15 Apr. 2004), p. 153004. DOI: `10.1103/PhysRevLett.92.153004`. URL: `https://link.aps.org/doi/10.1103/PhysRevLett.92.153004`.

[63] S. B. Nagel et al. “Magnetic trapping of metastable $^3P_2$ atomic strontium”. In: *Phys. Rev. A* 67 (1 Jan. 2003), p. 011401. DOI: `10.1103/PhysRevA.67.011401`. URL: `https://link.aps.org/doi/10.1103/PhysRevA.67.011401`.

[64] Simon Stellmer and Florian Schreck. “Reservoir spectroscopy of $5s5p\ ^3P_2$–$5snd\ ^3D_{1,2,3}$ transitions in strontium”. In: *Phys. Rev. A* 90 (2 Aug. 2014), p. 022512. DOI: `10.1103/PhysRevA.90.022512`. URL: `https://link.aps.org/doi/10.1103/PhysRevA.90.022512`.

[65] N. Poli et al. “Cooling and trapping of ultracold strontium isotopic mixtures”. In: *Phys. Rev. A* 71 (6 June 2005), p. 061403. DOI: `10.1103/PhysRevA.71.061403`. URL: `https://link.aps.org/doi/10.1103/PhysRevA.71.061403`.

[66] Simon Stellmer and Florian Schreck. “Reservoir spectroscopy of $5s5p\ ^3P_2$–$5snd\ ^3D_{1,2,3}$ transitions in strontium”. In: *Phys. Rev. A* 90 (2 Aug. 2014), p. 022512. DOI: `10.1103/PhysRevA.90.022512`. URL: `https://link.aps.org/doi/10.1103/PhysRevA.90.022512`.

[67] T. L. Nicholson et al. “Systematic evaluation of an atomic clock at 2 × 10-18 total uncertainty”. In: *Nature Communications* 6.1 (Apr. 2015), p. 6896. ISSN: 2041-1723. DOI: `10.1038/ncomms7896`. URL: `https://doi.org/10.1038/ncomms7896`.

[68] Steven Chu. “Laser Manipulation of Atoms and Particles”. In: *Science* 253.5022 (1991), pp. 861–866. DOI: `10.1126/science.253.5022.861`. eprint: `https://www.science.org/doi/pdf/10.1126/science.253.5022.861`. URL: `https://www.science.org/doi/abs/10.1126/science.253.5022.861`.

[69] Harold Metcalf and Peter van der Straten. “Cooling and trapping of neutral atoms”. In: *Physics Reports* 244.4 (1994), pp. 203–286. ISSN: 0370-1573. DOI: `https://doi.org/10.1016/0370-1573(94)90035-3`. URL: `https://www.sciencedirect.com/science/article/pii/0370157394900353`.

[70] Rudolf Grimm, Matthias Weidemüller, and Yurii B. Ovchinnikov. “Optical Dipole Traps for Neutral Atoms”. In: ed. by Benjamin Bederson and Herbert Walther. Vol. 42. Advances In Atomic, Molecular, and Optical Physics. Academic Press, 2000, pp. 95–170. DOI: `https://doi.org/10.1016/S1049-250X(08)60186-X`. URL: `https://www.sciencedirect.com/science/article/pii/S1049250X0860186X`.

[71] Marcin Bober, Jerzy Zachorowski, and Wojciech Gawlik. “Designing Zeeman slower for strontium atoms - towards optical atomic clock”. In: *Optica Applicata* 40 (2010).

[72] Sofus Laguna Kristensen. *Cavity-Enhanced Atom Interferometry with Optical Lattice Trapping on Seconds Timescale.* Master’s thesis, Niels Bohr Institute, 2019.

[73] Steven Chu. "Nobel Lecture: The manipulation of neutral particles". In: *Rev. Mod. Phys.* 70 (3 July 1998), pp. 685–706. DOI: `10.1103/RevModPhys.70.685`. URL: `https://link.aps.org/doi/10.1103/RevModPhys.70.685`.

[74] Paul D. Lett et al. "Observation of Atoms Laser Cooled below the Doppler Limit". In: *Phys. Rev. Lett.* 61 (2 July 1988), pp. 169–172. DOI: `10.1103/PhysRevLett.61.169`. URL: `https://link.aps.org/doi/10.1103/PhysRevLett.61.169`.

[75] David J Griffiths and Darrell F Schroeter. *Introduction to quantum mechanics*. Cambridge university press, 2018.

[76] P.W. Milonni and J.H. Eberly. *Laser Physics*. Wiley, 2010. ISBN: 9780470409701. URL: `https://books.google.dk/books?id=f7g0Mx5RR3cC`.

[77] T. H. Maiman. "Stimulated Optical Radiation in Ruby". In: *Nature* 187.4736 (Aug. 1960), pp. 493–494. ISSN: 1476-4687. DOI: `10.1038/187493a0`. URL: `https://doi.org/10.1038/187493a0`.

[78] Fritz Riehle. *Frequency Standards: Basics and Applications*. Wiley-VCH, 2004. ISBN: 9783527402304. URL: `https://books.google.dk/books?id=3S9RAAAAMAAJ`.

[79] E.T. Jaynes and F.W. Cummings. "Comparison of quantum and semiclassical radiation theories with application to the beam maser". In: *Proceedings of the IEEE* 51.1 (1963), pp. 89–109. DOI: `10.1109/PROC.1963.1664`.

[80] Matthew A Norcia. "Coupling atoms to cavities using narrow linewidth optical transitions: applications to frequency metrology". In: *PJ. Phys. B: At. Mol. Opt. Phys.* 52 (193001 2019). DOI: `10.1088/1361-6455/ab3930`.

[81] Zilong Chen et al. "Cavity-aided nondemolition measurements for atom counting and spin squeezing". In: *Phys. Rev. A* 89 (4 Apr. 2014), p. 043837. DOI: `10.1103/PhysRevA.89.043837`. URL: `https://link.aps.org/doi/10.1103/PhysRevA.89.043837`.

[82] C. Gerry and P.L. Knight. *Introductory Quantum Optics*. Cambridge University Press, 2005. ISBN: 9780521527354. URL: `https://books.google.dk/books?id=CgByyoBJJwgC`.

[83] Stefan Schäffer. "Cavity-enhanced optical clocks". Available at `https://nbi.ku.dk/english/theses/phd-theses/phd_theses_2019/stefan_alaric_schaffer/Stefan_alaric.pdf`. PhD thesis. Niels Bohr Institute, July 2019.

[84] Jiazhong Hu et al. "Entangled collective-spin states of atomic ensembles under nonuniform atom-light interaction". In: *Phys. Rev. A* 92 (6 Dec. 2015), p. 063816. DOI: `10.1103/PhysRevA.92.063816`. URL: `https://link.aps.org/doi/10.1103/PhysRevA.92.063816`.

[85] J. Gripp, S. L. Mielke, and L. A. Orozco. “Evolution of the vacuum Rabi peaks in a detuned atom-cavity system”. In: *Phys. Rev. A* 56 (4 Oct. 1997), pp. 3262–3273. DOI: `10.1103/PhysRevA.56.3262`. URL: `https://link.aps.org/doi/10.1103/PhysRevA.56.3262`.

[86] D. Meiser et al. “Prospects for a Millihertz-Linewidth Laser”. In: *Phys. Rev. Lett.* 102 (16 Apr. 2009), p. 163601. DOI: `10.1103/PhysRevLett.102.163601`. URL: `https://link.aps.org/doi/10.1103/PhysRevLett.102.163601`.

[87] R. J. Thompson, G. Rempe, and H. J. Kimble. “Observation of normal-mode splitting for an atom in an optical cavity”. In: *Phys. Rev. Lett.* 68 (8 Feb. 1992), pp. 1132–1135. DOI: `10.1103/PhysRevLett.68.1132`. URL: `https://link.aps.org/doi/10.1103/PhysRevLett.68.1132`.

[88] R Culver et al. “Collective strong coupling of cold potassium atoms in a ring cavity”. In: *New Journal of Physics* 18.11 (Nov. 2016), p. 113043. DOI: `10.1088/1367-2630/18/11/113043`. URL: `https://dx.doi.org/10.1088/1367-2630/18/11/113043`.

[89] D.A. Steck. *Quantum and Atom Optics*. 2007. URL: `https://books.google.dk/books?id=bc9TMwEACAAJ`.

[90] S. A. Schäffer et al. “Dynamics of bad-cavity-enhanced interaction with cold Sr atoms for laser stabilization”. In: *Phys. Rev. A* 96 (1 July 2017), p. 013847. DOI: `10.1103/PhysRevA.96.013847`. URL: `https://link.aps.org/doi/10.1103/PhysRevA.96.013847`.

[91] Bjarke T. R. Christensen et al. “Nonlinear spectroscopy of Sr atoms in an optical cavity for laser stabilization”. In: *Phys. Rev. A* 92 (5 Nov. 2015), p. 053820. DOI: `10.1103/PhysRevA.92.053820`. URL: `https://link.aps.org/doi/10.1103/PhysRevA.92.053820`.

[92] Mikkel Tang et al. “Cavity-immune spectral features in the pulsed superradiant crossover regime”. In: *Phys. Rev. Research* 3 (3 Sept. 2021), p. 033258. DOI: `10.1103/PhysRevResearch.3.033258`. URL: `https://link.aps.org/doi/10.1103/PhysRevResearch.3.033258`.

[93] D J McCarron, S A King, and S L Cornish. “Modulation transfer spectroscopy in atomic rubidium”. In: *Measurement Science and Technology* 19.10 (Aug. 2008), p. 105601. DOI: `10.1088/0957-0233/19/10/105601`. URL: `https://dx.doi.org/10.1088/0957-0233/19/10/105601`.

[94] and. “Modulation Transfer Spectroscopy of Ytterbium Atoms in a Hollow Cathode Lamp”. In: *Chinese Physics Letters* 28.3 (Mar. 2011), p. 033202. DOI: `10.1088/0256-307X/28/3/033202`. URL: `https://dx.doi.org/10.1088/0256-307X/28/3/033202`.

[95] R. W. P. Drever et al. "Laser phase and frequency stabilization using an optical resonator". In: *Applied Physics B* 31.2 (June 1983), pp. 97–105. ISSN: 1432-0649. DOI: `10.1007/BF00702605`. URL: `https://doi.org/10.1007/BF00702605`.

[96] S. Snigirev et al. "Fast and dense magneto-optical traps for strontium". In: *Phys. Rev. A* 99 (6 June 2019), p. 063421. DOI: `10.1103/PhysRevA.99.063421`. URL: `https://link.aps.org/doi/10.1103/PhysRevA.99.063421`.

[97] Daniel Schaeder Barker. *Degenerate Gases of Strontium for Studies of Quantum Magnetism.* Jan. 2016. DOI: `https://doi.org/10.13016/M2HB8S`.

[98] M. Schioppo et al. "A compact and efficient strontium oven for laser-cooling experiments". In: *Review of Scientific Instruments* 83.10 (Oct. 2012), p. 103101. ISSN: 0034-6748. DOI: `10.1063/1.4756936`. eprint: `https://pubs.aip.org/aip/rsi/article-pdf/doi/10.1063/1.4756936/14133321/103101\_1\_online.pdf`. URL: `https://doi.org/10.1063/1.4756936`.

[99] Ruwan Senaratne et al. "Effusive atomic oven nozzle design using an aligned microcapillary array". In: *Review of Scientific Instruments* 86.2 (Feb. 2015), p. 023105. ISSN: 0034-6748. DOI: `10.1063/1.4907401`. eprint: `https://pubs.aip.org/aip/rsi/article-pdf/doi/10.1063/1.4907401/15729100/023105\_1\_online.pdf`. URL: `https://doi.org/10.1063/1.4907401`.

[100] Thomas H. Loftus et al. "Narrow line cooling and momentum-space crystals". In: *Phys. Rev. A* 70 (6 Dec. 2004), p. 063413. DOI: `10.1103/PhysRevA.70.063413`. URL: `https://link.aps.org/doi/10.1103/PhysRevA.70.063413`.

[101] Poonam Arora et al. "Measurement of Temperature of Atomic Cloud Using Time-of-Flight Technique". In: *MAPAN-Journal of Metrology Society of India* 27 (Mar. 2012), pp. 31–39. DOI: `10.1007/s12647-012-0003-3`.

[102] Matthew A. Norcia et al. "Superradiance on the millihertz linewidth strontium clock transition". In: *Science Advances* 2.10 (2016), e1601231. DOI: `10.1126/sciadv.1601231`. eprint: `https://www.science.org/doi/pdf/10.1126/sciadv.1601231`. URL: `https://www.science.org/doi/abs/10.1126/sciadv.1601231`.

[103] Matthew A. Norcia et al. "Frequency Measurements of Superradiance from the Strontium Clock Transition". In: *Phys. Rev. X* 8 (2 May 2018), p. 021036. DOI: `10.1103/PhysRevX.8.021036`. URL: `https://link.aps.org/doi/10.1103/PhysRevX.8.021036`.

[104] Matthew A. Norcia and James K. Thompson. "Cold-Strontium Laser in the Superradiant Crossover Regime". In: *Phys. Rev. X* 6 (1 Mar. 2016), p. 011025. DOI: `10.1103/PhysRevX.6.011025`. URL: `https://link.aps.org/doi/10.1103/PhysRevX.6.011025`.

[105] Christoph Hotter et al. "Continuous multi-step pumping of the optical clock transition in alkaline-earth atoms with minimal perturbation". In: *Opt. Express* 30.4 (Feb. 2022), pp. 5553–5568. DOI: `10.1364/OE.445976`. URL: `https://opg.optica.org/oe/abstract.cfm?URI=oe-30-4-5553`.

[106] Simon B. Jäger et al. "Regular and bistable steady-state superradiant phases of an atomic beam traversing an optical cavity". In: *Phys. Rev. A* 103 (1 Jan. 2021), p. 013720. DOI: `10.1103/PhysRevA.103.013720`. URL: `https://link.aps.org/doi/10.1103/PhysRevA.103.013720`.

[107] Sławomir Bilicki. "Strontium optical lattice clocks: clock comparisons for timescales and fundamental physics applications". PhD thesis. Paris, CEA, 2017.

[108] R Hobson. "An optical lattice clock with neutral strontium". PhD thesis. University of Oxford, 2016. URL: `https://ora.ox.ac.uk/objects/uuid:d52faaaf-307c-4b48-847f-be590f46136f`.

[109] E. L. Hahn. "Spin Echoes". In: *Phys. Rev.* 80 (4 Nov. 1950), pp. 580–594. DOI: `10.1103/PhysRev.80.580`. URL: `https://link.aps.org/doi/10.1103/PhysRev.80.580`.

[110] J. Grünert and A. Hemmerich. "Optimizing the production of metastable calcium atoms in a magneto-optical trap". In: *Applied Physics B* 73.8 (Dec. 2001), pp. 815–818. ISSN: 1432-0649. DOI: `10.1007/s003400100768`. URL: `https://doi.org/10.1007/s003400100768`.

[111] R. Hobson et al. "Midinfrared magneto-optical trap of metastable strontium for an optical lattice clock". In: *Phys. Rev. A* 101 (1 Jan. 2020), p. 013420. DOI: `10.1103/PhysRevA.101.013420`. URL: `https://link.aps.org/doi/10.1103/PhysRevA.101.013420`.

[112] Tomoya Akatsuka et al. "Three-stage laser cooling of Sr atoms using the $5s5p^3P_2$ metastable state below Doppler temperatures". In: *Phys. Rev. A* 103 (2 Feb. 2021), p. 023331. DOI: `10.1103/PhysRevA.103.023331`. URL: `https://link.aps.org/doi/10.1103/PhysRevA.103.023331`.

[113] Christoph Hotter, David Plankensteiner, and Helmut Ritsch. "Continuous narrow-band lasing with coherently driven V-level atoms". In: *New Journal of Physics* 22.11 (Nov. 2020), p. 113021. DOI: `10.1088/1367-2630/abc70c`. URL: `https://dx.doi.org/10.1088/1367-2630/abc70c`.

[114] Krishna K. Meduri et al. "Dynamically induced irreversibility in coherently driven systems". In: *Phys. Rev. Lett.* 71 (26 Dec. 1993), pp. 4311–4314. DOI: `10.1103/PhysRevLett.71.4311`. URL: `https://link.aps.org/doi/10.1103/PhysRevLett.71.4311`.

[115] Hannes Gothe et al. “Continuous-wave virtual-state lasing from cold ytterbium atoms”. In: *Phys. Rev. A* 99 (1 Jan. 2019), p. 013415. DOI: `10.1103/PhysRevA.99.013415`. URL: `https://link.aps.org/doi/10.1103/PhysRevA.99.013415`.

[116] Rahul Sawant and S. A. Rangwala. “Lasing by driven atoms-cavity system in collective strong coupling regime”. In: *Scientific Reports* 7.1 (Sept. 2017), p. 11432. ISSN: 2045-2322. DOI: `10.1038/s41598-017-11799-5`. URL: `https://doi.org/10.1038/s41598-017-11799-5`.

[117] Yuan Zhang, Chongxin Shan, and Klaus Mølmer. “Ultranarrow Superradiant Lasing by Dark Atom-Photon Dressed States”. In: *Phys. Rev. Lett.* 126 (12 Mar. 2021), p. 123602. DOI: `10.1103/PhysRevLett.126.123602`. URL: `https://link.aps.org/doi/10.1103/PhysRevLett.126.123602`.